Application of characterisation methods in the development of biomedical titanium alloys

Jajčinović, Magdalena; Slokar Benić, Ljerka; Pezer, Robert; Holjevac Grgurić, Tamara

Source / Izvornik: **Machines, Technologies, Materials, 2023, 17, 86 - 89**

Journal article, Published version
Rad u časopisu, Objavljena verzija rada (izdavačev PDF)

International journal for science, technics and innovations for the industry

MACHINES TECHNOLOGIES MATERIALS

YEAR XVII Issue 2 / 2023 ISSN PRINT 1313-0226
ISSN WEB 1314-507X

Published by
Scientific technical
Union of Mechanical Engineering

MACHINES. TECHNOLOGIES. MATERIALS

INTERNATIONAL SCIENTIFIC JOURNAL

ISSN PRINT 1313-0226, ISSN WEB 1314-507X, YEAR XVII, ISSUE 2 / 2023

INTERNATIONAL EDITORAL BORARD

EDITOR IN CHIEF:		
Georgi Popov	Technical University of Sofia	BG
MEMBERS:		
Abdrakhman Naizabekov	Rudny industrial institute	KZ
Ahmet H. Ertas	Bursa Technical University	TR
Albert Albers	Karlsruhe Institut of Technology	DE
Andrzej Golabczak	Lodz University of Technology	PL
Andrzej Huczko	Warsaw University	PL
Dimitar Karaivanov	University of Chemical Technology and Metallurgy, Sofia	BG
Dobre Runchev	Ss. Cyril and Methodius University in Skopje	NM
Emilia Abadjieva	Akita University	JP
Erdem Camurlu	Akdeniz University, Antalya	TR
Eugen Sheregii	University of Rzeszow	PL
Franz Haas	Graz University of Technology	AT
Galina Nicolcheva	Technical University of Sofia	BG
Gennadii Bagliuk	Institute for Problems of Materials Science NAS of Ukraine, Kiev	UA
Georgii Raab	Ufa State Aviation Technical University	RU
Gregory Gurevich	Shamoon College of Engeeniring, Ashdod	IL
Hiroyuki Moriyama	Tokai University, Hiratsuka	JP
Idilia Batchkova	University of Chemical Technology and Metallurgy, Sofia	BG
Ivan Kralov	Technical University of Sofia	BG
Ivan Kuric	University of Zilina	SK
Julieta Kaleicheva	Technical University of Sofia	BG
Katia Vutova	Institute of Electronics, Bulgarian Academy of Sciences	BG
Maria Nikolova	Angel Kanchev University of Ruse	BG
Natasa Naprstkova	Jan Evangelista Purkyne University in Usti nad Labem	CZ
Oana Dodun	Gheorghe Asachi Technical University of Iasi	RO
Ognyan Andreev	Technical University of Sofia	BG
Predrag Dasic	High Technical Mechanical School of Trstenik	RS
Rasa Kandrotaite	Kaunas University of Technology	LT
Raul Turmanidze	Georgian Technical University, Tbilisi	GE
Roumen Petrov	Ghent University	BE
Sergey Dobatkin	National University of Science and Technology "MISIS", Moscow	RU
Souren Mitra	Jadavpur University, Kolkata	IN
Svetlana Gubenko	National Metallurgical Academy of Ukraine, Dnipro	UA
Vedran Mrzljak	University of Rijeka	HR
Wu Kaiming	Wuhan University of Science and Technology	CN

TECHNICAL EDITORS:
M. Sc. Eng. Radoslav Daskalov, M. Sc. Eng. Oleg Mihailov

Scientific and technical union of mechanical engineering
108 R. S. Rakovski str., Sofia, Bulgaria
www.stumejournals.com, office@stumejournals.com

CONTENTS

MACHINES

TECHNOLOGIES

MATERIALS

Visualization and analysis of worm gear drives efficiency and load capacity

Svetlin Stoyanov, Gergana Mollova
University of Ruse “Angel Kanchev”, 8 Studentska str., POB 7017, Ruse, Bulgaria
SStoyanov@Uni-Ruse.BG, Gergana_Mollova@yahoo.co.uk

Abstract: *Scientific methodologies have been created and applied during the analysis upon worm gear drives. Important parameters have been selected in order to make significant investigations in the area of worm gear efficiency and load capacity. The efficiency coefficient and maximal torque values have been studied for several combinations of modules, ratios, center distances, etc. The results have been presented and analysed through three-dimensional graphics. Conclusions are made.*

Keywords*: WORM GEAR DRIVES, GEAR EFFICIENCY, LOAD CAPACITY, SCIENTIFIC METHODOLOGIES, EFFICIENCY COEFFICIENT, MAXIMAL TORQUE, SOFTWARE SYSTEMS, COMPUTER-AIDED MATHEMATICS, THREE-DIMENSIONAL GRAPHICS.*

1. Introduction

A worm drive is a power transmission device in which a worm meshes with a worm gear to transmit power between two non-intersecting shafts that are oriented at a right angle. Worm gear drives are quite suitable for transmitting large gear ratios in one stage.

Some important features of worm gears are:

- A probability to achieve self-locking when reversing the direction of the power flow;
- Quiet operation capacity;
- Suitable when the space is limited;
- Absorption of shock loading;
- Minimum maintenance.

Small changes in parameters of worm gear drives can lead to the significant savings which is not the case in other drives [8]. This makes the selection of parameters of these drives to be a very important topic, which product development engineers are often not aware.

The main criterion for worm gear load capacity is the output torque of the worm gear shaft, which is directly connected to the driven machine. Output torque values could be limited certain conditions during transmission operation. Some significant boundary conditions are [1, 2, 3, 14]:

- pitting, which can appear on the active flanks of the worm gear teeth;
- wear, which usually on the flanks of the bronze worm gear;
- heating of transmission and scuffing, which depends on the load and sliding velocity values.

The friction coefficient in the meshing represents a complex characteristic regarding the quality of the worm gear train. Several different approaches and models have been presented in previous research by the authors’ team. The German standard DIN 3996: 2012-09 describes a short and clear approach [12]. On the other hand, the approach described in [16] and [17] presents a more complex and detailed method.

Besides, the investigations described in [16] and [17] treat other important problems for worm gear drives. The authors of these publications analyze the temperature and temperature variations in the contact meshing area. They emphasize that these variations could have relative great influence upon the wear of the worm gears. In other previous publications of the authors’ team, the calculations for various parameters of worm gears have been analyzed. Some main calculation approaches are standardized in [10, 9, 11, 13].

The authors’ team and other scientists from the ***University of Ruse*** have successfully completed some investigation tasks in the field of energy efficiency of drive systems and transmissions. The results of these studies are presented in detail in the following publications: [1-7].

2. A historical overview of this research

In [14], a new methodology was been created including several stages. The methodology involves the application of the scientific approach described in [15].

The new methodology from [14], starts with calculating the tangential frequency, the sliding speed, the efficiency coefficient, and the important tribology parameters. The calculations are carried out for a worm made of case-hardened steel 16 MnCr5 and for a worm made of GZ-CuSn12Ni. The necessary parameters are defined, trough which it becomes possible to determine the maximal actual contact stresses. Upon these calculations, the maximal output torque T_2 is determined. A database is generated and a graphical presentation is created.

Also, an optimization procedure has been created aiming to improve the load capacity parameters of worm gear trains [14]. Different functional parameters and certain geometry parameters have been taken into account such as rotating frequency of the worm shaft, gear ratio, module and geometry dimensions of the worm gear set.

Based upon the methodology described, in [14, 15] a substantial investigation has been carried out. The object of analysis and discussion of the paper presented will be the results concerning the center distance $a = 50$ mm. The calculation results for the efficiency coefficients ηz and maximal output torques T_2 in Nm depending on gear ratios i and modules m (in mm) at center distance $a = 50$ mm and $n_1 = 1500$ min^{-1} are summarized in Table 1 [14]. The calculations are carried out with 9 different values of the gear ratios *i* and 3 different values of the module *m*.

Table 1: *Results for center distance* $a = 50$ *mm and* $n_1 = 1500$ *min*$^{-1}$

	i	*m*	*ni*	*T2*
1	4.83	2.5	0.9314	14.97
2	7.25	2.5	0,9120	24,79
3	9,5	2	0,8994	30,91
4	14,5	2,5	0,8478	58,43
5	19	2	0,8289	72,67
6	29	2,5	0,7445	136,61

On this stage of the research, a question haw to present and analyze the data obtained raising.

In [1, 2, 14, 15] this is solved with the help of the software system ***MS Excel***. A plain 2-D graphs are created to visualize the relations obtained.

In [18] is analyzed an idea to use the flexibility and power of the contemporary computer-aided mathematics software systems.

For example, Fig. 1 and Fig. 2 [14] shows the variation of coefficient of efficiency and output torque in a graphical way depending on the values of the gear ratio and the module.

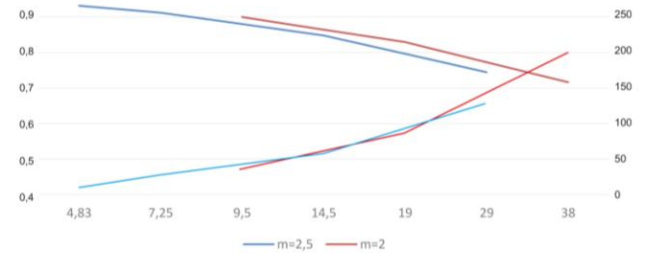

Fig. 1. *Variation of the efficiency coefficients and maximal output torques for a center distance a = 50 mm and rotation speed of worm gear shaft* $n_1 = 1500\ min^{-1}$.

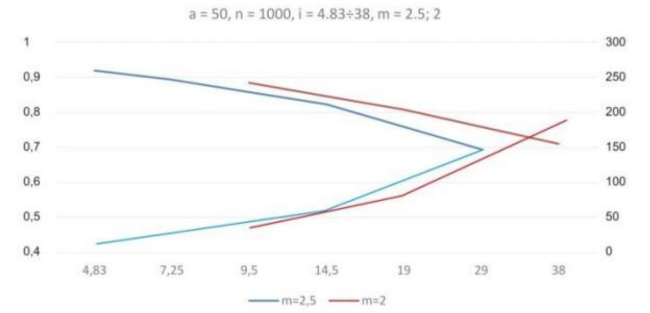

Fig. 2. *Variation of the efficiency coefficients and maximal output torques for a center distance a = 50 mm and rotation speed of worm gear shaft* $n_1 = 1000\ min^{-1}$.

In [14], a conclusion has been made that the area of maximal values of efficiency efficient and output torques is located in the gear ratio interval between 20 and 29 with modulus equal to 2 mm and 2.5 mm.

3. A new methodology – data interpolation and three-dimensional visualisation

The contemporaly growth of software systems provides powerfull new opportunities in all areas of engineering and science. This also applies to the field of mathematics. The systems ***MATLAB***, ***Wolfram Mathematica*** and ***Maple*** can be cited as leading systems for computer-aided mathematics [18].

With the help of software system ***MATLAB***, the calculated in [14, 15] data has been interpolated and visualized [18]. This gives two new abilities, as follows:

- An ability to directly signify the relations between three parameters (or even between four parameters, if the color in set as independent indicator);
- An ability to render relations in uninterrupted three-dimensional space (or even in four-dimensional space, if the color in set as independent indicator).

It follows some three-dimensional visualisation created and the conclusions obtained from them.

3.1. Efficiency coefficient in relation from ratio and module

Colored three-dimensional graphs are created for the all combinations of:

- **center distances:** *a* = 50 mm, *a* = 63 mm, *a* = 80 mm, and *a* = 125 mm

and

- **input rotation speeds**: $n_1 = 750\ min^{-1}$, $n_1 = 1000\ min^{-1}$, $n_1 = 1500\ min^{-1}$.

In this paper are presented some of the characteristic plots. On Fig 3 is shown a graph composed of two planes. The second plane is located in the left down corner on Fig. 3a, but for this to be visible, the graph must be rotated as it is shown on Fig. 3b. The black straight line is the border between the planes.

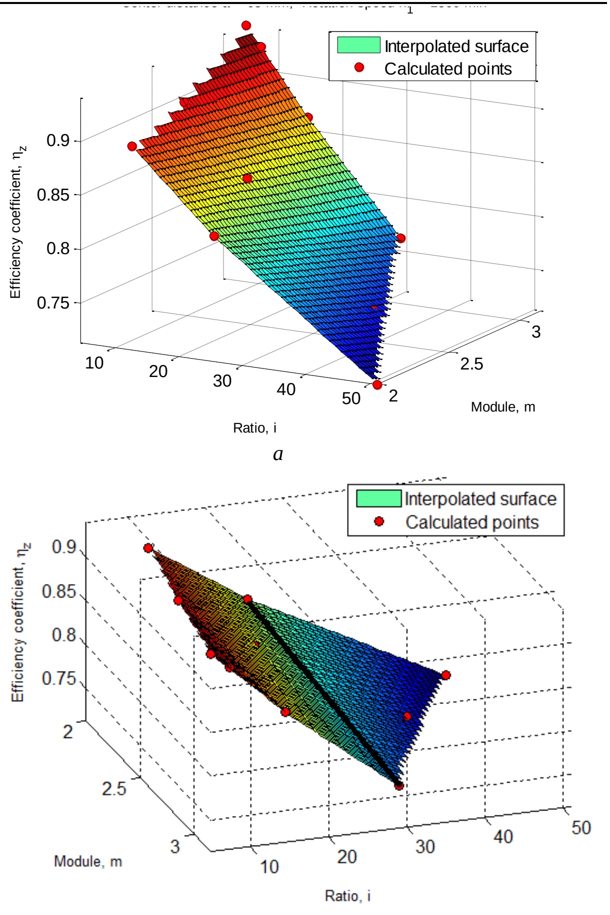

a

b

Fig. 3. *Efficiency coefficient in relation from ratio and module for center distance a = 63 mm and rotation speed* $n_1 = 1500\ min^{-1}$.

From Fig. 3, it can be observed that the efficiency coefficient increases with the increase of the module and the decrease of the ratio.

On Fig 4 is presented an analogical case, i.e., a surface that interpolates data points, one of which is higher than others. The relations of the efficiency coefficient from the ratio and module remains the same as on Fig 3.

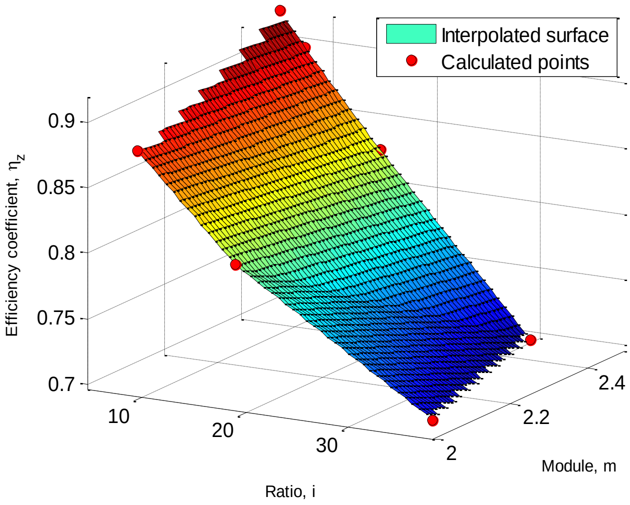

Fig. 4. *Efficiency coefficient in relation from ratio and module for center distance a = 50 mm and rotation* n_1 *= speed* $1000\ min^{-1}$.

The next plot is example for two data points located about the middle of the interpolated surface, which are out of the plane – Fig. 5. It can be observed that in these points the efficiency coefficient has a higher value, than in the other points of the interpolated plane surface.

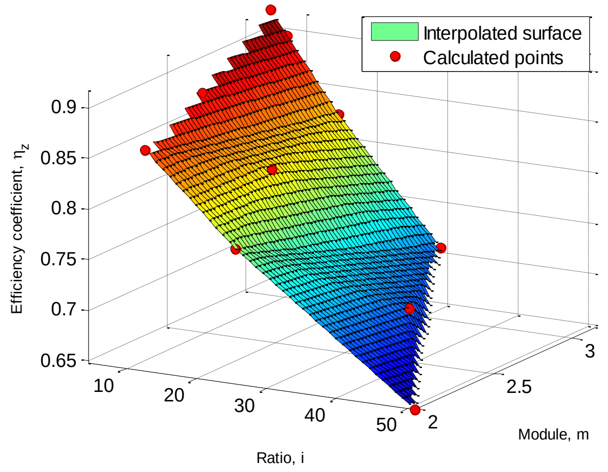

Fig. 5. *Efficiency coefficient in relation from ratio and module for center distance a = 63 mm and rotation speed* $n_1 = 750$ *min*$^{-1}$.

And, as the end of this section, Fig. 6 shows a different picture. There is a data point with lower value of the efficiency coefficient than other points in the plane interpolated surface. That is in the top left corner, i.e., in the area with higher values of the efficiency coefficient.

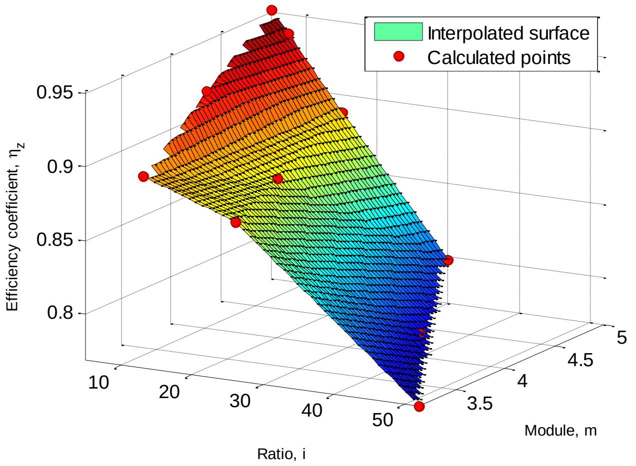

Fig. 6. *Efficiency coefficient in relation from ratio and module for center distance a = 100 mm and rotation speed* $n_1 = 1500$ *min*$^{-1}$.

The trend of the dependence of the efficiency coefficient from the ratio and module permanently becomes unchanged and is confirmed in all four figures from Fig. 3 to Fig. 6.

3.2. Efficiency coefficient in relation from ratio and output torque

On Fig. 7 is shown a relation of the efficiency coefficient from the ratio and the output torque T_2. **It can be concluded that, the efficiency coefficient grows with decreasing the output torque and the ratio.**

The software system ***MATLAB*** gives the ability multiple three-dimensional surfaces to be superimposed. On Fig. 8b are presented two three-dimensional relations together for center distance a = 63 mm and rotation speed n_1 = 1500 min^{-1}, as follows:

- the dependence of the efficiency coefficient from the ratio and module;
- the dependence of the efficiency coefficient from the ratio and **output torque.**

The relations for efficiency coefficient ant the output torque for other center distances and input rotation speeds are also investigated. Some of them are shown oh Fig. 9, Fig. 10, and Fig. 11. From these graphs, it can be concluded that **the trend of the dependence of the efficiency coefficient from the ratio and the output torque becomes unchanged, i.e., the efficiency coefficient grows with decreasing the output torque and the ratio.**

The presented results can be used for performing an optimization process with ***MATLAB Optimization Toolbox*** [18]. It provides functions for finding parameters that minimize or maximize objectives while satisfying constraints. The toolbox includes solvers for linear programming (LP), mixed-integer linear programming (MILP), quadratic programming (QP), second-order cone programming (SOCP), nonlinear programming (NLP), constrained linear least squares, nonlinear least squares, and nonlinear equations.

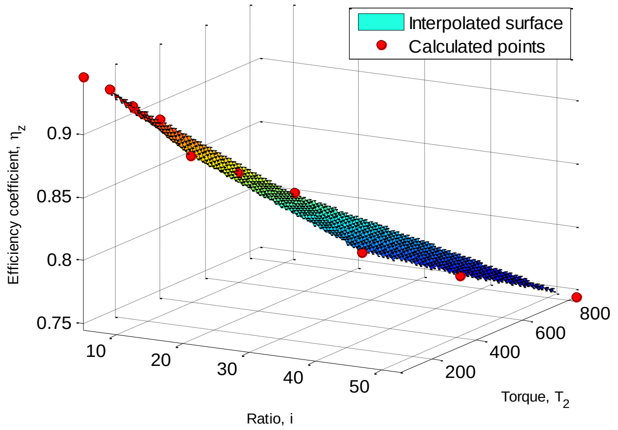

Fig. 7. *Efficiency coefficient for center distance a = 80 mm and rotation speed* $n_1 = 1500$ *min*$^{-1}$.

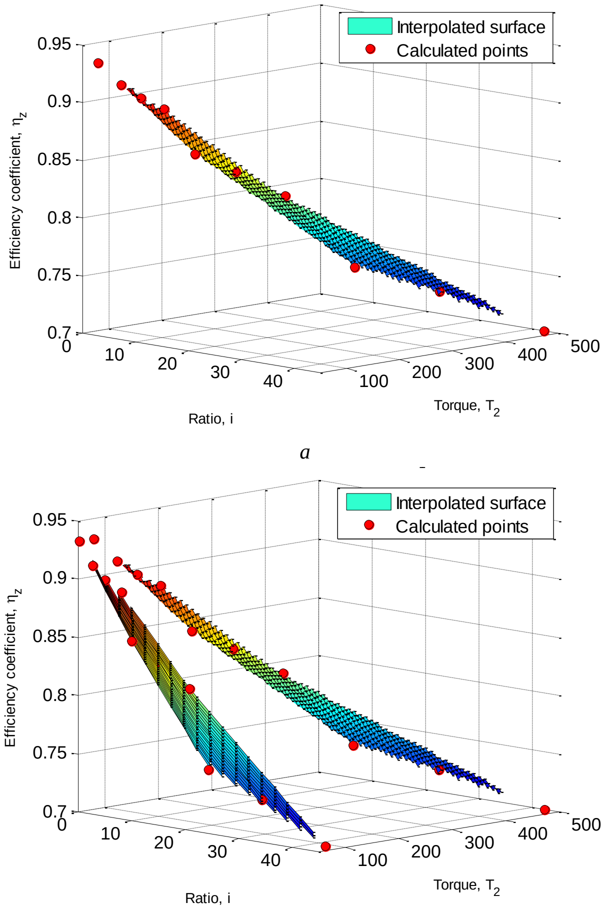

a

b

Fig. 8. *Efficiency coefficient for center distance a = 63 mm and rotation speed* $n_1 = 1500$ *min*$^{-1}$*: a – efficiency coefficient in function of ratio and torque; b – with superimposed surface of efficiency coefficient in function of ratio and module.*

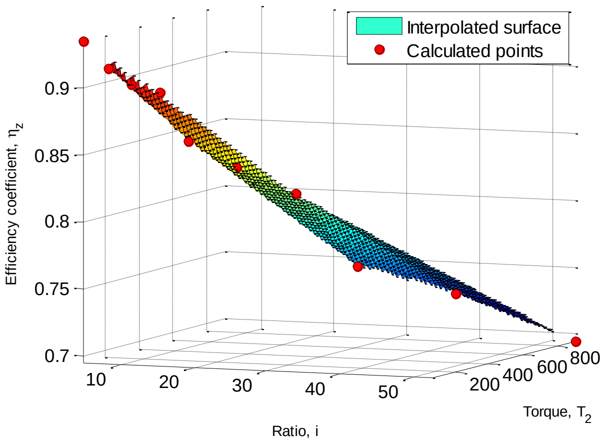

Fig. 9. *Efficiency coefficient and output torque for center distance a = 80 mm and rotation speed* $n_1 = 1000$ *min*$^{-1}$.

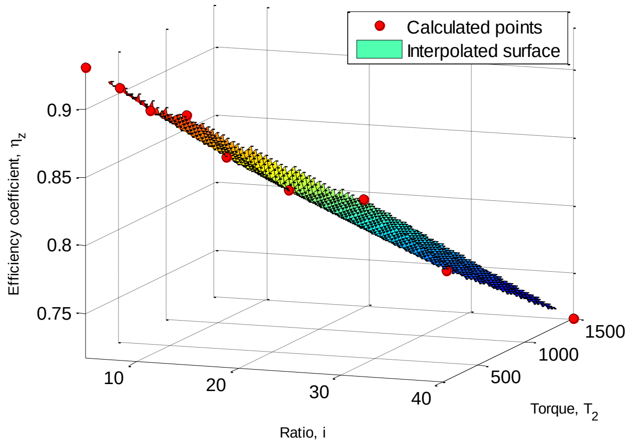

Fig. 10. *Efficiency coefficient and output torque for center distance a = 100 mm and rotation speed* $n_1 = 750$ *min*$^{-1}$.

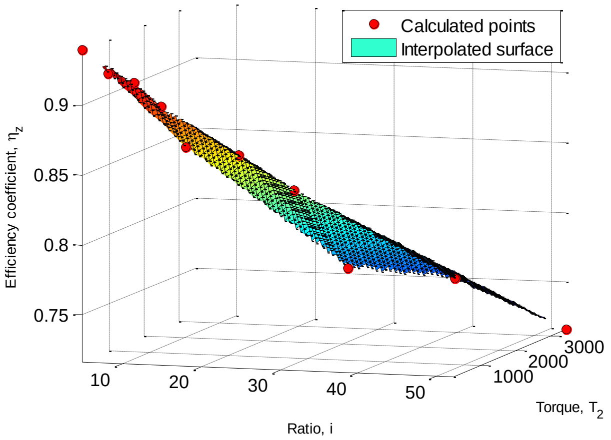

Fig. 11. *Efficiency coefficient and output torque for center distance a = 125 mm and rotation speed* $n_1 = 750$ *min*$^{-1}$.

4. Conclusions

The efficiency coefficient and maximal torque values have been investigated for several combinations of modules, ratios, center distances, etc. The results have been presented and analyzed through three-dimensional graphics. For the aim of this, a new methodology based on data interpolation and three-dimensional visualization are developed and applied.

From the results obtained, it can be concluded that the efficiency coefficient increases with the increase of the module and the decrease of the ratio. This trend remains for all the cases studied. Although this trend, there is some exceptions for local points as it is noted specifically when the graphs were discussed.

It is established that the efficiency coefficient grows with decreasing the output torque and the ratio. This trend is also stable for all cases studied.

MATLAB Optimization Toolbox™ lets design optimization tasks to be conducted. It includes parameter estimation, component selection, and parameter tuning. In combination with computer-aided design software (CAD), this gives an ability the above presented research to be continued with development and investigation of an automatized optimization and design system. This can be done in the integrated working environment of the software systems ***MATLAB*** and ***SolidWorks***.

5. References

1. A. Dobreva, P. Pavlov. Energy Efficiency of Worm Gear Drives, Proceedings of the 32nd DAAAM International Symposium, pp.0110-0116 (2021)
2. A. Dobreva, V. Dobrev, G. Mollova. Research of gear drives. IOP Conf. Ser.: Mater. Sci. Eng. 1220-012025 (2022)
3. A. Dobreva. Methods for Improving the Geometry Parameters and the Energy Efficiency of Gear Trains with Internal Meshing. VDI – Berichte, No 2199. 2, pp. 1291 – 1302, (2013)
4. A. Dobreva & V. Dobrev. Improving the Tribological Characteristics of Heavy Loaded Gear Boxes. Proceedings of the First Balkan Conference on Tribology “Balkantrib’93”, Vol 2.3, Sofia, pp. 166-170, (1993)
5. A. Dobreva & V. Dobrev. Innovative Methodology for Decreasing Mechanical Losses in Vehicles. Proceedings of the 4th International Congress of Automotive and Transport Engineering (AMMA 2018), Springer Verlag, pp. 234 – 242, (2018)
6. A. Dobreva & S. Stoyanov. Optimization Research of Gear Trains with Internal Meshing. Ruse, University Publishing Centre, pp 144, (2012
7. A. Dobreva. Theoretical Investigation of the Energy Efficiency of Planetary Gear Trains. Mechanisms and Machine Science, No 13, pp. 289-298, (2013)
8. A. Miltenovic, M. Banic, D. Miltenović. Load capacity of worm gear transmission from aspect of maximal use of available resources. MATEC Web of Conferences (2017)
9. AGMA 6034-B92. Practice for Enclosed Cylindrical Wormgear Speed Reducers and Gearmotors. Alexandria, VA: American Gear Manufacturers Association, (2010)
10. Bulgarian National Standard 12256-78. Worm-gears cylindrical. Output worm and output production worm, (1978)
11. DIN 3976. Cylindrical worms; dimensions, coordination of centre distances and gear ratios of worm drives. Berlin, (1980)
12. DIN 3996. 2012-09. Load capacity calculation of cylindrical worm gears with axes crossing at 90 degree angles, Berlin, (2012)
13. DIN 3996. 2012-09. Load capacity calculation of cylindrical worm gears with axes crossing at 90 degree angles, Berlin, (2012).
14. G. Mollova, A. Dobreva. Improving load capacity parameters of worm gears. MATEC Web of Conferences 366, 02002 (2022)
15. G. Mollova, V. Dobrev. Design methodology for investigating worm gear transmissions with significant dimensions. IN: Proceedings of University of Ruse, Vol 60, ISSN: 1311-3321, pp. 41-47, (2021)
16. M. Oehler, B. Magyar, B. Sauer Coupled thermal and tribological analysis of worm gear. Tribol. Lubrication technology 65 (1), pp. 54–60, (2018)
17. M. Oehler, B. Magyar, B. Sauer. Worm gear efficiency – worm gear efficiency. Final report, Frankfurt am Main, (2016)
18. S. Stoyanov. Visualization and analysis of gear drives parameters with the help of computer-aided mathematics systems. XX Jubilee International Congress – Machines, Technologies, Materials, winter session, Borovets, Bulgaria (2023) (to be published)

Design and CFD simulation of the exhaust manifold of the Formula Student vehicle

Marko Lučić
Faculty of Mechanical Engineering, University of Montenegro, Podgorica, Montenegro
E-mail: markol@ucg.ac.me

Abstract: *One of the biggest challenges in the FSAE competition is adapting the power unit to the strict regulations of the competition. The task of the exhaust manifold is to enable the best possible flow of exhaust gases from the engine to the environment. A properly designed vehicle exhaust manifold is of great importance for enabling better performance of the power unit. There are several different concepts for designing exhaust manifolds. Each concept has its advantages and disadvantages. One of the main guidelines when designing the exhaust manifold is to enable air flow with as little local resistance as possible so that the exhaust gases are released into the environment as soon as possible. In this work, a 3D model of three types of exhaust manifolds was created, and then a CFD simulation of airflow through exhaust manifolds was performed using ANSYS Fluent software. CFD simulations help to a great extent with a better design of the exhaust manifold.*

Keywords*: CFD, EXHAUST MANIFOLD, VEHICLE, IC ENGINES, FORMULA STUDENT*

1. Introduction

The design of the exhaust manifold is one of the biggest challenges when designing a Formula Student vehicle, as evidenced by a large number of scientific works on the mentioned topic [1-6]. Ref. [7] showed that with a proper design of the exhaust manifold, the exhaust emission can be reduced. In this paper, a CFD analysis of several different models of the exhaust manifold was performed. In the first chapter, what was done in the work itself was defined. The second chapter deals with the Formula Student rulebook with special reference to the part of the rulebook related to the driving system of the vehicle. The third chapter talks about exhaust manifolds in general. A CFD analysis of various Exhaust System concepts is presented in chapter four. In chapter five, the results of CFD analyzes of different concepts of exhaust branches are presented, while in chapter six, a conclusion related to the topic of the paper is given. Chapter seven lists the literature used in this paper.

2. Exhaust design limitations for a Formula Student vehicle

As the topic of this paper is the CFD analysis of the exhaust manifold of the engine used in the Formula Student competition, this chapter will talk about the competition itself. Formula Student or formerly "Formula SAE" (FSAE) is the most complex, demanding, and attractive student engineering competition in the world organized by the Society of Automotive Engineers (SAE). One of the biggest challenges of the Formula Student competition is the design of the exhaust system. The restrictions related to the internal combustion engine are shown in the Formula Student Rules [8]. By this regulation, the internal combustion engine that powers the FSAE vehicle is limited to a four-stroke, internal combustion piston engine with a volume of no more than 710 cm^3 per cycle. Given the previously mentioned limitation, the choice of internal combustion engines is limited to those that are usually installed in racing motorcycles. Another major limitation of the internal combustion engine that applies is related to the air intake. Rulebook [8] stipulates that all air sucked into the engine must pass through the restrictor. The maximum restrictor diameters which must be respected at all times during the competition are 20 mm for gasoline-fueled vehicles or 19 mm for E 85-fueled vehicles. The exhaust opening must be directed to the side or rear of the vehicle so that the driver is not exposed to the fumes at any speed given the vehicle's ground clearance. The exhaust port(s) must not extend more than 450 mm beyond the center line of the rear axle and must not be more than 600 mm above the ground. All exhaust components (headers, mufflers, etc.) protruding from the side of the body in front of the main hoop must be protected to prevent contact by persons approaching the vehicle or the driver exiting the vehicle. The temperature of the outer surface must not be harmful to the person touching it. The maximum sound level test speed for a given engine will be the engine speed that corresponds to an average piston speed of 15.25 m/s. The calculated speed will be rounded to the nearest 500 rpm. The maximum permitted sound level up to this calculated speed is 110 dB(C), fast weighing. The exhaust manifold used on racing motorcycle engines must be changed and another must be designed and manufactured that will be more suitable for use on a four-wheeled vehicle. When choosing an internal combustion engine to be used, it is necessary to carry out detailed analyses, primarily about the number of cylinders, but also other analyzes related to construction parameters. Analysis of the kinematics of a four-cylinder engine with internal combustion using CATIA software is presented in the paper [9].

3. Exhaust manifolds and exhaust headers

The exhaust manifold is somewhat similar to the intake manifold. The intake manifold receives incoming air from a central point, be it the throttle body or carburetor. Using the intake manifold, the air is distributed to the individual cylinders. The exhaust manifold allows the exhaust gases of individual cylinders to exit the cylinder head immediately into a single collection path or chamber. An exhaust manifold is not the most efficient design solution, but it is the simplest, most direct, and cheapest solution for ejecting exhaust gases from the engine. In the automotive industry, exhaust manifolds were made of cast iron for decades because they were cheaper to produce, but also because of their compact size compared to steel tubular exhaust manifolds. The major disadvantages of cast-iron exhaust manifolds are almost no tuning potential for internal combustion engines. Tubular structures that required assembly and welding have been avoided for years. There were rare cases where exhaust manifolds were made from steel pipes that were joined into a single outlet pipe. Tubular exhaust manifolds offer the possibility of better engine customization and have great potential for extracting additional power and torque, while cast-iron exhaust manifolds have significant design limitations. The positive side of cast-iron exhaust manifolds is that they are made from one piece, require less proctor in the vehicle, and are usually significantly thicker, so they better insulate the noise and temperatures of the exhaust gases of internal combustion engines. Cast-iron exhaust manifolds due to very sharp curves can cause a bottleneck effect which can have a very unfavorable effect on the engine. Tubular headers have a weight advantage over cast-iron manifolds. The single most important advantage is that tubular exhaust headers can increase the power and torque of the engine. Tubular headers are available in several configurations. Tubular headers with different tube lengths are used for simpler and easier installation. Tubular headers with the same pipe lengths provide a significant advantage in terms of more efficient balancing of exhaust flow and pressure. Tubular headers are made with significantly less sharp corners of the pipes in contrast to cast-iron manifolds and thus allow better flows. The big disadvantage of tubular headers is the very high price, especially if they are made of stainless steel. This cost can be very justified if you consider the performance advantage over manifolds. Depending on the specific vehicle, the installation of tubular headers represents an additional challenge due to the space limitations of where it should be placed. Also, the disadvantage of tubular headers about manifolds is the tendency to create more noise due to the wear of smaller pipes [10].

4. CFD simulation

In this paper, CFD analysis of several different models of the exhaust system for the internal combustion engine used to drive the Formula Student vehicle was performed. The geometry of the exhaust systems analyzed in this paper corresponds to the engine that is installed in the motorcycle of the Japanese manufacturer Yamaha, trademark YZF-R6. Figures 1 to 3 show the models analyzed in this paper. 3D models of exhaust systems were created in Solid Works software. CFD analysis of exhaust systems was done in ANSYS Fluent software. Exhaust manifolds analyzed in this paper are marked with the marks A, B, and C. Manifold A has equal lengths of cylindrical pipes that connect to the main pipe under the same radius (Figure 1). Exhaust manifold B has different lengths of cylinder pipes that join the main pipe at the same radius (Figure 2). Manifold C represents a classic exhaust manifold design (Figure 3).

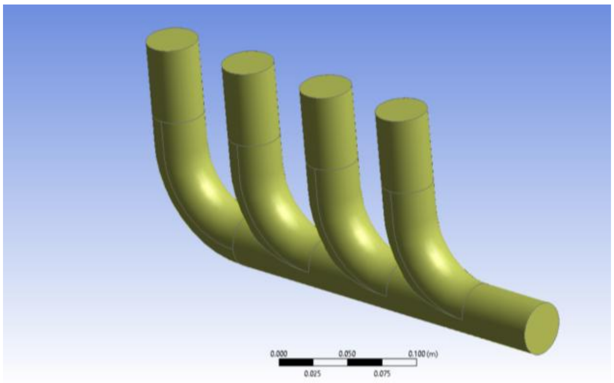

Fig. 1 *Exhaust manifold A*

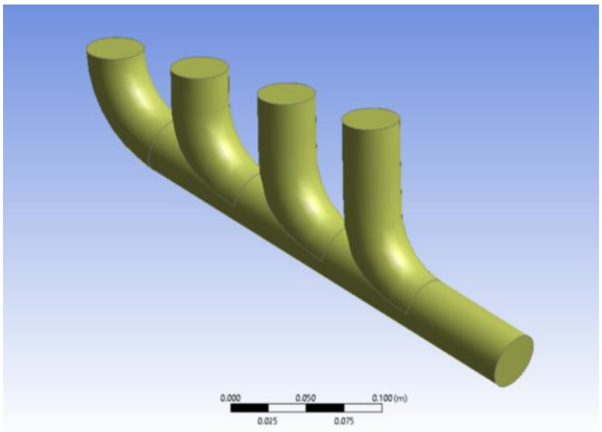

Fig. 2 *Exhaust manifold B*

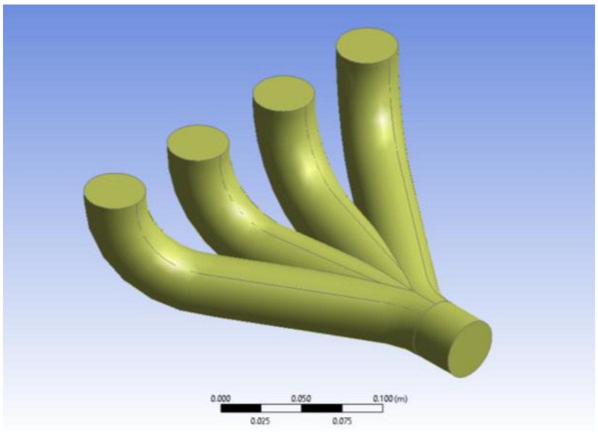

Fig. 3 *Exhaust manifold C*

After generating the fluid domain, a mesh was created for each of the models. The appearance of the created network is shown in Figures 4 to 6. Setting up the network for models during CFD simulation is a very demanding and complex job.

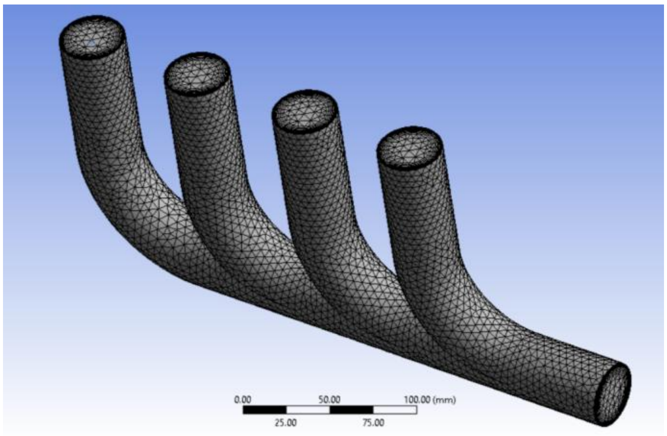

Fig. 4 *Mesh for Exhaust Manifold A*

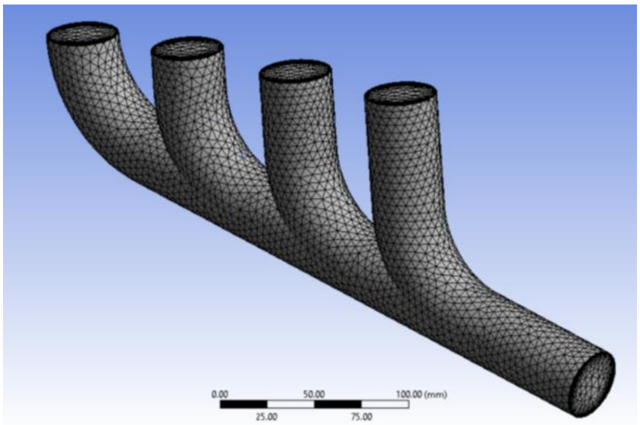

Fig. 5 *Mesh for Exhaust Manifold B*

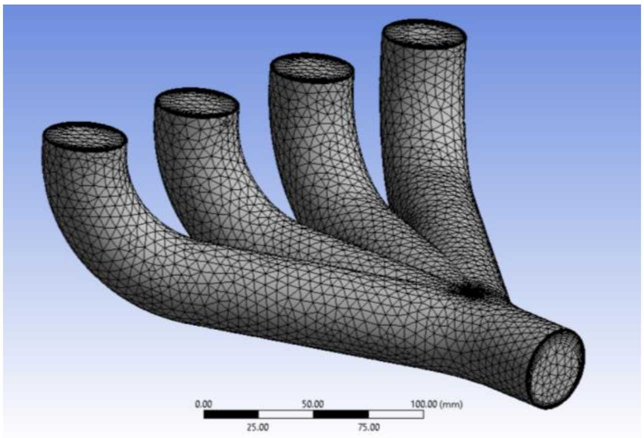

Fig. 6 *Mesh for Exhaust Manifold C*

After creating the network for the generated models of exhaust manifolds, it is necessary to set up the CFD simulation. For the CFD simulation, the standard k-epsilon turbulence model with standard constants was used: Cmu=0.09, C1-Epsilon=1.44, C2-epsilon=1.92, TKE Prandtl Number=,1 and TDE Prandtl Number=1.3. Enhanced wall treatment with pressure gradient effects was also used. Material fluid properties are shown in Table 1.

Table 1: *Material fluid properties*

Material	Gasoline-vapor C8H18
Density [kg/m^3]	1.0
Viscosity [kg/m s]	1.72 x 10^{-5}
Thermal Conductivity [W/m K]	0.0454

After defining the material, boundary conditions were defined. Boundary conditions are set so that at the entrance to the exhaust manifolds we have a velocity magnitude of 30 m/s and that the temperature at the inlet is 700 K. As it is a four-cylinder engine, each of the considered exhaust manifolds has 4 inlets and one outlet. The inlets and outlets for each of the exhaust manifolds are shown in Figures 7, 8, and 9.

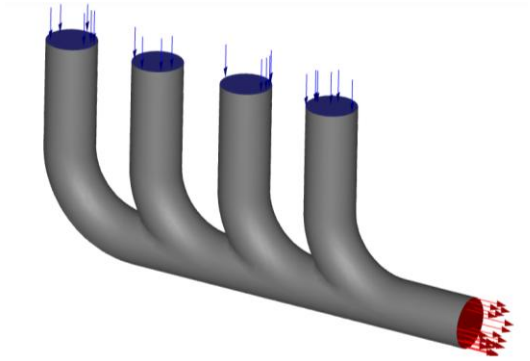

Fig. 7 *Inlets and outlet for Exhaust manifold A*

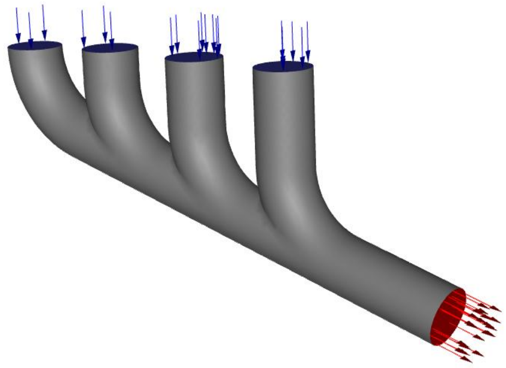

Fig. 8 *Inlets and outlet for Exhaust manifold B*

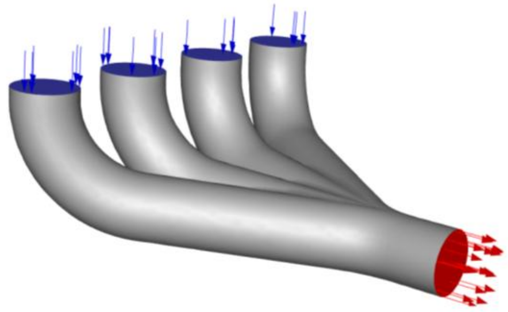

Fig. 9 *Inlets and outlet for Exhaust manifold C*

5. CFD simulation results

In this chapter, the results of the CFD analysis of the three types of exhaust manifolds that were considered (Exhaustmanifoldsd A, B, and C) are given. Figures 10 to 12 show pressure contours for the considered exhaust manifolds in this paper.

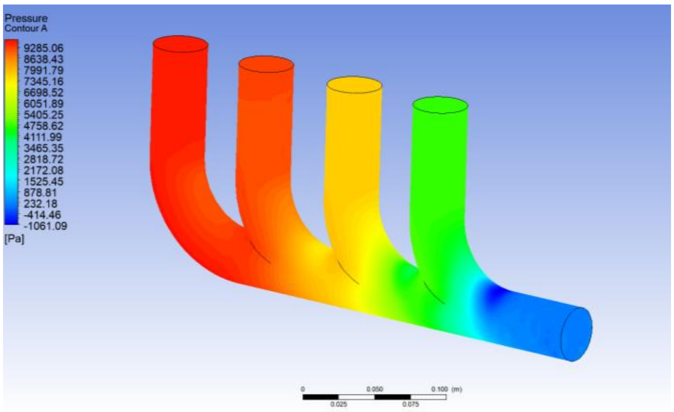

Fig. 10 *Pressure contour for Exhaust manifold A*

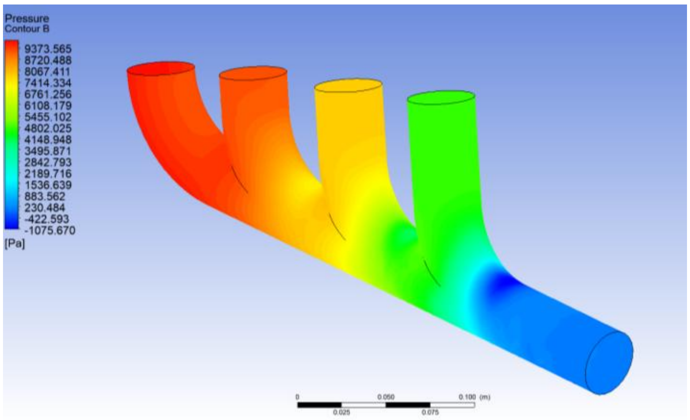

Fig. 11 *Pressure contour for Exhaust manifold B*

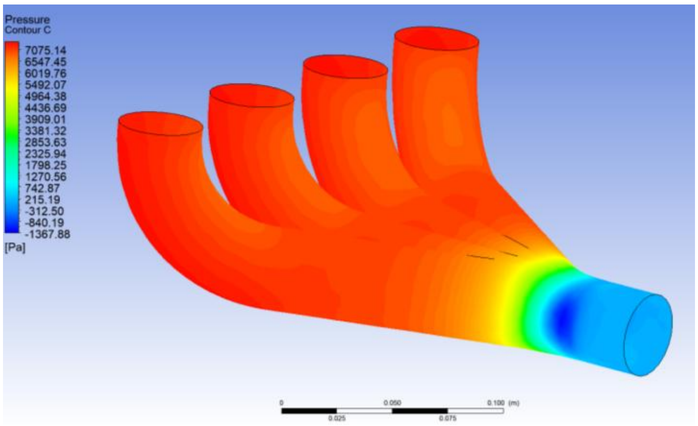

Fig. 12 *Pressure contour for Exhaust manifold C*

Figures 13 to 15 show the velocity streamlines for the considered exhaust manifolds.

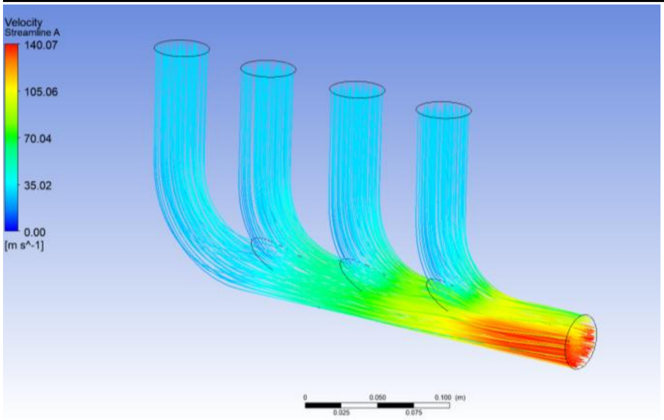

Fig. 13 *Velocity streamlines for Exhaust manifold A*

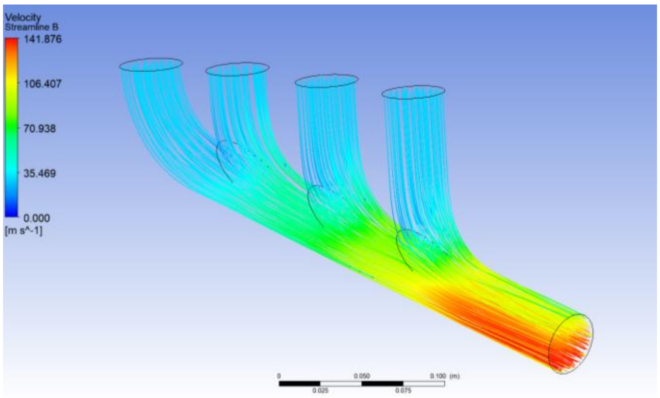

Fig. 14 *Velocity streamlines for Exhaust Manifold B*

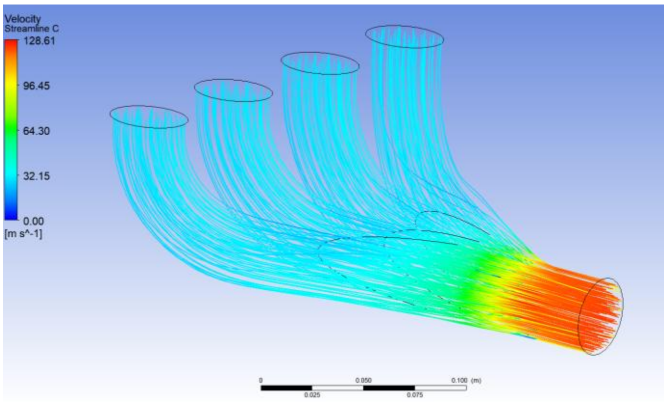

Fig. 15 *Velocity streamlines for Exhaust Manifold C*

From the previous pictures it can be seen that the results for exhaust manifolds A and B are very similar. Otherwise, these two exhaust manifolds are similar in terms of geometry, with the difference that Exhaust manifold B has pipes of different lengths that connect to the main pipe. Exhaust manifold A has a geometrically simpler construction, that is, the pipes used to distribute exhaust gas from the cylinders to the main pipe are of the same length. For these two exhaust manifolds, the pressure and flow velocity differ very little. Exhaust manifold C has significantly different results compared to the previous two. To better understand the results of the CFD analysis, the values of maximum pressure and maximum velocity for all exhaust manifolds that were considered are shown in Table 2.

Table 2: *Max values of pressure and velocity for Exhaust manifolds A, B, and C*

	Max pressure [Pa]	Max velocity [m/s]
Manifold A	9285.06	140.07
Manifold B	9373.58	141.87
Manifold C	7075.14	128.61

6. Conclusion

CFD simulations of airflow through the Exhaust manifold are of great importance because they make huge savings during the development of the system itself. CFD simulations have proven to be a very powerful tool when simulating the most realistic conditions in which the corresponding element or system being analyzed can work. These simulations can provide very important information related to the development of the exhaust manifold itself. CFD simulations of three types of exhaust manifolds were performed in the paper as a potential design solution for exhaust manifolds of Formula Student vehicles. When choosing the appropriate exhaust manifold concept, it is necessary to take into account some other parameters. One very important parameter is the production of the exhaust manifold itself, as well as the production costs. Exhaust manifold C is much more complex to manufacture compared to Exhaust manifolds A and B because it requires much more precise pipe-cutting and welding technology. Almost negligible differences in the CFD analysis results occur with Exhaust manifolds A and B because they are geometrically very similar.

7. References

1. Mohamad, B., Ali, M. Q., Neamah, H. A., Zelentsov, A., & Amroune, S. (2020). Fluid dynamic and acoustic optimization methodology of a formula-student race car engine exhaust system using multilevel numerical CFD models. *Diagnostyka*, *21*.
2. Yamamoto, S., Matsumoto, S., Ueda, T., Kodama, T., Honda, Y., & Wakabayashi, K. (2007). *A Study on Intake and Exhaust System of Turbocharged Engine under the Regulations of Formula SAE* (No. 2007-32-0113). SAE Technical Paper. 36-39.
3. Narang, H., Sharma, K., Mehta, D., Sheth, S., Bhanderi, S., & Patel, A. Design and Fabrication of Exhaust System of Formula Student Car
4. Mohamad, B. A. (2021). *Modelling and testing of advanced intake and exhaust system components for race car engines* (Doctoral dissertation, University of Miskolc).
5. Teja, M. A., Ayyappa, K., Katam, S., & Anusha, P. (2016). Analysis of exhaust manifold using computational fluid dynamics. *Fluid Mech Open Acc*, *3*(1), 1000129.
6. Umesh, K. S., & Rajagopal, V. P. K. (2013). CFD Analysis of Exhaust Manifold of Multi-Cylinder Si Engine Todetermine Optimal Geometry for Reducing Emissions. *International Journal of Automobile Engineering Research and Development*, 45-56.
7. Formula Student Rules. (2022). *SAE*
8. Lučić, M. (2022). Kinematic analysis of the slider-crank mechanism of an internal combustion (IC) engine using modern software. *Mechanization in agriculture & Conserving of the resources*, *68*(1), 11-17.
9. Mike, Narvigia. (2014). Performance Exhaust Systems: How to Design, Fabricate, and Install. *CarTech*, ISBN 978-1-61325-207-9

Influence of the window profile on the final quality of the product

Elena Jevtoska[1]
Faculty for design and technology of furniture and interior-Skopje, Str. 16-ta Makedonska Brigada" N 3 Skopje
ejevtoska@gmail.com

Abstract *The current product on the market offers a wide range of diverse profiles for producing windows that are made of different materials, width and order of grills depending on the profile. Within the framework of this research the windows with same dimensions shall be elaborated, those which are made of the same production capacity and use the same fittings but different types of PVC profiles. The aim is to prove what kind of influence the used profile has over the final quality of the product. For this research, two groups and six subgroups will be tested. In each subgroup, one tests five windows made of the same profile. The groups are divided according to the used fittings. The testing of the quality shall be conducted in accordance with the European norms EN 1026:2016 (Windows and doors - Air permeability - Test method), EN 1027:2016 (Windows and doors - Water tightness - Test method), EN 12211:2016 (Windows and doors - Resistance to wind load - Test method).*

Keywords*: CONSTRUCTION CARPENTRY, WINDOW, AIR PERMEABILITY, WIND RESISTANCE, PVC PROFILES*

1. Introduction

The quality of one product is a characteristic worth being considered when it is proven that the same satisfies the needs for which it is produced. Having in mind that the purpose of one window is to provide light and desirable ventilation of a room, and, at the same time, to protect the object from external influences such as air permeability, water tightness and resistance to wind, we state that the window is of a higher quality as much as it can guarantee all these conditions. The window as a product is of complex content from diverse materials and parts. As different parts of the window we enlist the following below: Frame – the frame is a construction of the jamb and the construction of the side jamb.

Glass – the content of the construction that can be made of glass and glass packet.

Hinge – design, window handle, window lockers which offer the sliding of the window, meaning, the possibility for its opening and closing.

Throughout the production of window parts, different types of materials are used:

Frame – wood profiles from different types of wood, PVC profiles, aluminum profiles, as well as a combination of these materials.

Glass – one glass (4mm, 6mm), glass packet out of two, three or four glasses with different combinations of glasses layered with different protective paints.

Fittings – metal, plastic, rubber.

Un-plasticized Poly Vinyl Chloride is relatively new to the building industry as a material for windows and doors. UPVC is based on poly vinyl chloride(PVC), one of the most versatile polymers found. UPVC is prepared with a special formulation in which different stabilizers and modifiers are added to poly vinyl chloride to make rigid and suitable for use as window frames. UPVC contains poly vinyl chloride(PVC), calcium carbonate(CaCo3) and titanium dioxide (TiO2). PVC forms the major constituent of blend composition. Unlike other polymer PVC is heat sensitive and requires additives during processing. Hence the properties of PVC can be increased through additives like light and UV stabilizer, fillers, pigments and lubricants can be added during the blending process. Titanium dioxide is an expensive pigment used for imparting natural white color to the UPVC profile and provide necessary UV stability for the product. Calcium carbonate are fillers which are inorganic minerals as fine particles homogenized in PVC blend. Usage of filler has effect on mechanical property like tensile strength, elongation, impact strength, shrinkage and cost. Production of UPVC involves a complex extrusion process. Extrusion is a manufacturing process where material is drawn through a die of required cross section. The main advantage of extrusion process is that it can create very complex sections and also can be used for brittle objects. Additionally this process provide excellent surface finishes. UPVC extrusion process can be recycled. UPVC has excellent insulation properties resulting in high energy efficiency.(1)

The non-polyvinyl chloride as a material offers possibilities for creating different window profiles in terms of the dimensions and the order of the grills. This paper has the aim of researching how much the diversification of the profiles influences the final quality of the window. The quality will be elaborating on the water tightness, air permeability as well as resistance to deformity on wind load.

2. Materials and research metod

The samples which are subject of the research are divided into two groups. In each group there are six subgroups, each consisting of five windows. All the samples' dimensions are 800mm width and 1400 mm height. All the samples in the subgroup are made of the same production capacity and the same type of fittings and profile is used for their making (Table 1). For all the samples in the subgroups a different type of profile is used..

Table 1: *Groups of the test samples*

Subgroup	Picture of the sample	Profile of the sample
Group 1 Windows with dimensions 800/1400mm Fitting AGB		
Subgroup 1		REHAU GENEO [2] 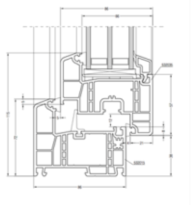
Subgroup 2		ALPHACAN 70R [3] 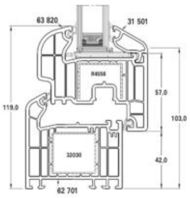
Subgroup 3		ALPHACAN PRESTIGIO [3] 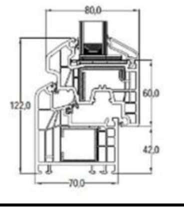

Subgroup 4		ALUPLAST IDEAL 4000 [4] 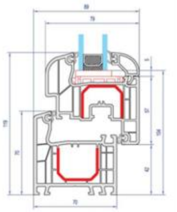
Subgroup 5		SCHUCO SYSTM CT 70 [5] 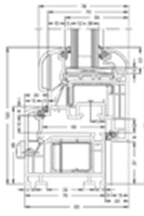
Subgroup 6		REHAU SYNEGO [2] 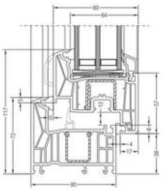
Group 2 Windows with dimensions 800/1400mm Fitting Sigenia		
Subgroup 7		KOMMERLINK [6] 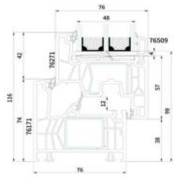
Subgroup 8		SCHUCO SI 82 [5] 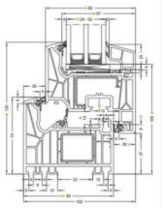
Subgroup 9		ALUPLAST IDEAL 8000 [4] 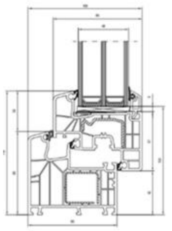
Subgroup 10		GEALAN S9000 [7] 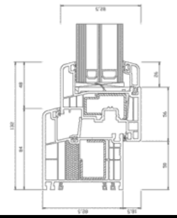
Subgroup 11		SALAMANDER STREAMLINE MD76 [8] 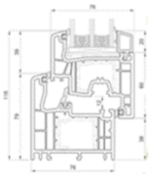
Subgroup 12		TROCAL 88mm [9] 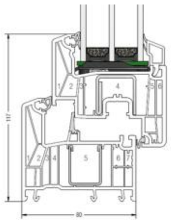

3. Results

3.1. Results of the air permeability

The testing of the air permeability is conducted with pressure and absorption of the different air pressure. The mean values for every subgroup will be presented individually in a diagram, just as the class according to the EN 1026:2016 "Windows and doors - Air permeability - Test method" standard. [10]

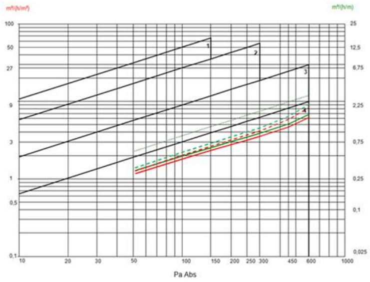

Fig.1 Air permeability measures for subgroup 1

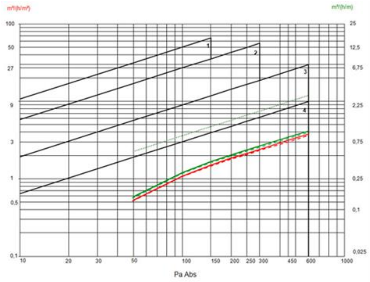

Fig.2 Air permeability measures for subgroup 2

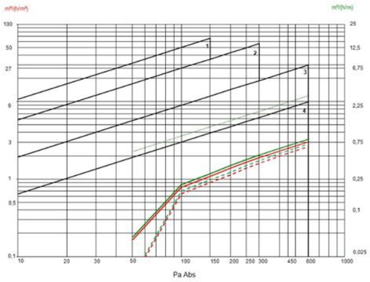

Fig.3 Air permeability measures for subgroup 3

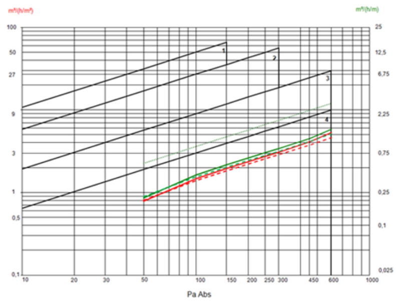

Fig.4 Air permeability measures for subgroup 4

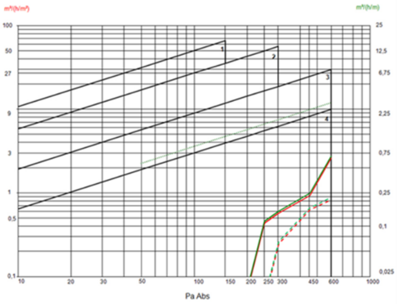

Fig.5 Air permeability measures for subgroup 5

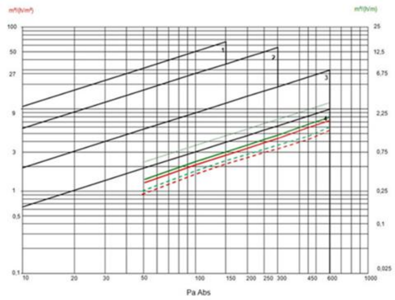

Fig.6 Air permeability measures for subgroup 6

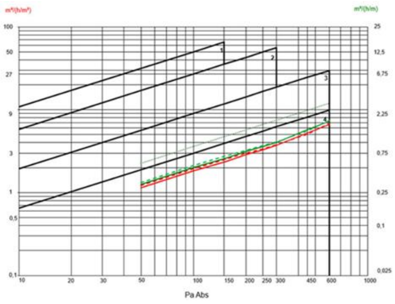

Fig.7 Air permeability measures for subgroup 7

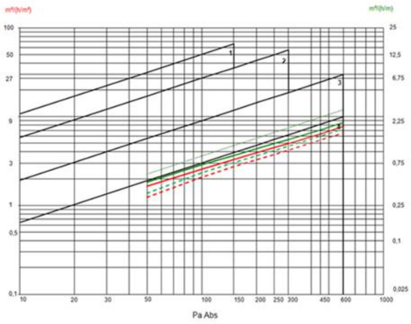

Fig.8 Air permeability measures for subgroup 8

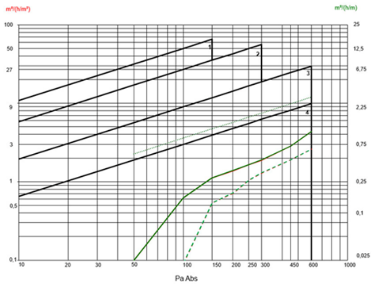

Fig.9 Air permeability measures for subgroup 9

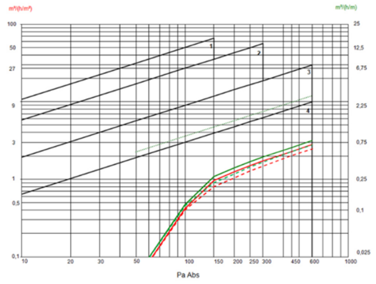

Fig.10 Air permeability measures for subgroup 10

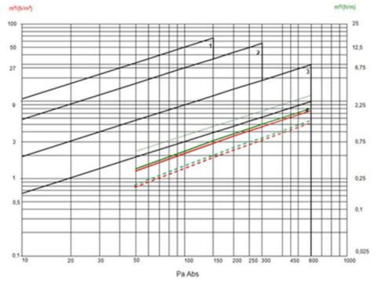

Fig.11 Air permeability measures for subgroup 11

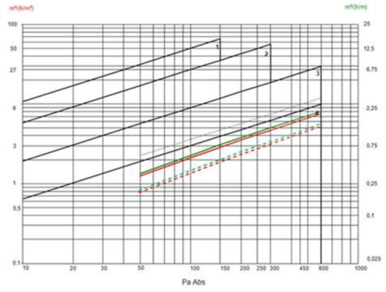

Fig.12 Air permeability measures for subgroup 12

3.2. Results – water tightness

Class according to the EN 1027:2016 "Windows and doors - *Water tightness - Test method*" standard. [11]

Table.2: *Subgroup 1 – water tightness*

class	Pressure in Pa		Time	Water strance		Observation
	Normal	Actual		Dripping	Flowing	
A1	0	0	15:00	**00:00**	**00:00**	**OK**
A2	50	50	05:00	**00:00**	**00:00**	**OK**
A3	100	100	05:00	**00:00**	**00:00**	**OK**
A4	150	150	05:00	**00:00**	**00:00**	**OK**
A5	200	201	05:00	**00:00**	**00:00**	**OK**
A6	250	250	05:00	**00:00**	**00:00**	**OK**
A7	300	301	05:00	**00:00**	**00:00**	**OK**
A8	450	449	05:00	**00:00**	**00:00**	**OK**
A9	600	601	05:00	**00:00**	**00:44**	**NOT OK**

Table.3: *Subgroup 2 – water tightness*

class	Pressure in Pa		Time	Water strance		Observation
	Normal	Actual		Dripping	Flowing	
A1	0	0	15:00	00:00	00:00	OK
A2	50	50	05:00	00:00	00:00	OK
A3	100	100	05:00	00:00	00:00	OK
A4	150	149	05:00	00:00	00:00	OK
A5	200	201	05:00	00:00	00:00	OK
A6	250	251	05:00	00:00	00:00	OK
A7	300	300	05:00	00:00	01:25	NOT OK

Table.4: *Subgroup 3 – water tightness*

class	Pressure in Pa		Time	Water strance		Observation
	Normal	Actual		Dripping	Flowing	
A1	0	0	15:00	00:00	00:00	OK
A2	50	50	05:00	00:00	00:00	OK
A3	100	100	05:00	00:00	00:00	OK
A4	150	148	05:00	00:00	00:00	OK
A5	200	201	05:00	00:00	00:00	OK
A6	250	251	05:00	00:00	00:00	OK
A7	300	300	05:00	00:00	00:14	NOT OK

Table.5: *Subgroup 4 – water tightness*

class	Pressure in Pa		Time	Water strance		Observation
	Normal	Actual		Dripping	Flowing	
A1	0	0	15:00	00:00	00:00	OK
A2	50	50	05:00	00:00	00:00	OK
A3	100	100	05:00	00:00	00:00	OK
A4	150	149	05:00	00:00	00:00	OK
A5	200	199	05:00	00:00	00:00	OK
A6	250	249	05:00	00:00	00:00	OK
A7	300	301	05:00	00:00	03:13	NOT OK

Table.6: *Subgroup 5 – water tightness*

class	Pressure in Pa		Time	Water strance		Observation
	Normal	Actual		Dripping	Flowing	
A1	0	-9	15:00	00:00	00:00	OK
A2	50	50	05:00	00:00	00:00	OK
A3	100	100	05:00	00:00	00:00	OK
A4	150	150	05:00	00:00	00:00	OK
A5	200	200	05:00	00:00	00:00	OK
A6	250	251	05:00	00:00	00:11	NOT OK

Table.7: *Subgroup 6 – water tightness*

class	Pressure in Pa		Time	Water strance		Observation
	Normal	Actual		Dripping	Flowing	
A1	0	0	15:00	00:00	00:00	OK
A2	50	50	05:00	00:00	00:00	OK
A3	100	100	05:00	00:00	00:00	OK
A4	150	150	05:00	00:00	00:00	OK
A5	200	200	05:00	00:00	00:00	OK
A6	250	251	05:00	00:00	00:00	OK
A7	300	300	05:00	00:00	00:00	OK
A8	450	451	05:00	00:00	00:00	OK
A9	600	600	05:00	00:00	00:00	OK

Table.8: *Subgroup 7 – water tightness*

class	Pressure in Pa		Time	Water strance		Observation
	Normal	Actual		Dripping	Flowing	
A1	0	0	15:00	00:00	00:00	OK
A2	50	50	05:00	00:00	00:00	OK
A3	100	100	05:00	00:00	00:00	OK
A4	150	150	05:00	00:00	00:00	OK
A5	200	201	05:00	00:00	00:00	OK
A6	250	250	05:00	00:00	00:00	OK
A7	300	300	05:00	00:00	00:00	OK
A8	450	451	05:00	00:00	00:17	NOT OK

Table.9: *Subgroup 8 – water tightness*

class	Pressure in Pa		Time	Water strance		Observation
	Normal	Actual		Dripping	Flowing	
A1	0	0	15:00	00:00	00:00	OK
A2	50	50	05:00	00:00	00:00	OK
A3	100	100	05:00	00:00	00:00	OK
A4	150	151	05:00	00:00	00:00	OK
A5	200	200	05:00	00:00	00:00	OK
A6	250	250	05:00	00:00	00:00	OK
A7	300	300	05:00	00:00	00:00	OK
A8	450	450	05:00	00:00	00:00	OK
A9	600	602	05:00	00:00	00:00	OK

Table.10: *Subgroup 9 – water tightness*

class	Pressure in Pa		Time	Water strance		Observation
	Normal	Actual		Dripping	Flowing	
A1	0	0	15:00	00:00	00:00	OK
A2	50	50	05:00	00:00	00:00	OK
A3	100	100	05:00	00:00	00:00	OK
A4	150	152	05:00	00:00	00:00	OK
A5	200	200	05:00	00:00	00:00	OK
A6	250	250	05:00	00:00	00:00	OK
A7	300	302	05:00	00:00	00:00	OK
A8	450	452	05:00	00:00	04:28	NOT OK

Table.11: *Subgroup 10 – water tightness*

class	Pressure in Pa		Time	Water strance		Observation
	Normal	Actual		Dripping	Flowing	
A1	0	0	15:00	00:00	00:00	OK
A2	50	50	05:00	00:00	00:00	OK
A3	100	100	05:00	00:00	00:00	OK
A4	150	150	05:00	00:00	00:00	OK
A5	200	200	05:00	00:00	00:00	OK
A6	250	250	05:00	00:00	00:00	OK
A7	300	299	05:00	00:00	00:00	OK
A8	450	450	05:00	00:00	00:00	OK
A9	600	603	05:00	00:00	00:00	OK

Table.12: *Subgroup 11 – water tightness*

class	Pressure in Pa		Time	Water strance		Observation
	Normal	Actual		Dripping	Flowing	
A1	0	0	15:00	00:00	00:00	OK
A2	50	50	05:00	00:00	00:00	OK
A3	100	100	05:00	00:00	00:00	OK
A4	150	150	05:00	00:00	00:00	OK
A5	200	200	05:00	00:00	00:00	OK
A6	250	250	05:00	00:00	00:00	OK
A7	300	302	05:00	00:00	00:00	OK
A8	450	453	05:00	00:00	04:01	NOT OK

Table.13: *Subgroup 12 – water tightness*

class	Pressure in Pa		Time	Water strance		Observation
	Normal	Actual		Dripping	Flowing	
A1	0	0	15:00	00:00	00:00	OK
A2	50	50	05:00	00:00	00:00	OK
A3	100	100	05:00	00:00	00:00	OK
A4	150	152	05:00	00:00	00:00	OK
A5	200	200	05:00	00:00	00:00	OK
A6	250	250	05:00	00:00	00:00	OK
A7	300	301	05:00	00:00	00:00	OK
A8	450	449	05:00	00:00	00:00	OK
A9	600	602	05:00	00:00	00:00	OK

3.3. Results – resistance to wind load

Class according to the *EN 12211:2016 "Windows and doors - Resistance to wind load - Test method"* standard. [12]

Table.14: *Maximum deflection to the classification at the base width*

Class		f (mm)
(a-c) 1250 mm		
A	(a-c)/150	8.33
B	(a-c)/200	6.25
C	(a-c)/300	4.67

Table.15: *Results of the frontal deflection in mm section/pressure – Subgroup 1*

Pa	1(a)	2(b)	3(c)	f (mm)
2000 Pa	0.64	3.11	0.37	2,60
0 Pa	0.00	0.00	0.00	0.0
-2001 Pa	0.79	2.09	0.50	1.45
0 Pa	0.03	0.02	0.00	0.01

Table.16: *Results of the frontal deflection in mm section/pressure – Subgroup 2*

Pa	1(a)	2(b)	3(c)	f (mm)
2001 Pa	0.46	5.41	0.95	4.71
0 Pa	0.01	0.04	0.01	0.03
-2003 Pa	0.29	5.31	0.76	4.79
0 Pa	0.00	0.01	0.00	0.01

Table.17: *Results of the frontal deflection in mm section/pressure – Subgroup 3*

Pa	1(a)	2(b)	3(c)	f (mm)
1999 Pa	0.50	5.44	0.85	4,77
0 Pa	0.01	0.04	0.01	0.03
-2001 Pa	0.27	5.38	0.72	4,89
0 Pa	0.00	0.01	0.00	0.01

Table.18: *Results of the frontal deflection in mm section/pressure – Subgroup 4*

Pa	1(a)	2(b)	3(c)	f (mm)
2003 Pa	0.59	6.02	0.36	5,54
0 Pa	0.05	0.04	0.04	0.01
-2001 Pa	0.41	6.82	0.49	6,37
0 Pa	0.02	0.00	0.00	0.01

Table.19: *Results of the frontal deflection in mm section/pressure – Subgroup 5*

Pa	1(a)	2(b)	3(c)	f (mm)
2003 Pa	0.54	0.85	0.36	0.40
0 Pa	0.10	0.07	0.05	0.01
-2000 Pa	0.53	0.85	0.50	0.34
0 Pa	0.00	0.00	0.00	0.00

Table.20: *Results of the frontal deflection in mm section/pressure – Subgroup 6*

Pa	1(a)	2(b)	3(c)	f (mm)
2007 Pa	0.58	5.17	0.68	4.54
0 Pa	0.00	0.00	0.00	0.00
-2003 Pa	0.83	5.23	0.93	4.35
0 Pa	0.00	0.00	0.00	0.00

Table.21: *Results of the frontal deflection in mm section/pressure – Subgroup 7*

Pa	1(a)	2(b)	3(c)	f (mm)
2005 Pa	0.51	6.06	0.42	5.60
0 Pa	0.00	0.00	0.00	0.00
-2006 Pa	0.22	4.56	0.21	4.35
0 Pa	0.00	0.00	0.00	0.00

Table.22: *Results of the frontal deflection in mm section/pressure – Subgroup 8*

Pa	1(a)	2(b)	3(c)	f (mm)
2001 Pa	2.54	2.89	0.60	1.29
0 Pa	0.00	0.00	0.00	0.00
-2004 Pa	1.21	1.45	0.37	0.66
0 Pa	0.00	0.00	0.00	0.00

Table.23: *Results of the frontal deflection in mm section/pressure – Subgroup 9*

Pa	1(a)	2(b)	3(c)	f (mm)
2008 Pa	0.34	1.08	0.85	0.49
0 Pa	0.00	0.00	0.00	0.00
-2005 Pa	0.16	0.72	0.45	0.42
0 Pa	0.00	0.00	0.00	0.00

Table.24: *Results of the frontal deflection in mm section/pressure – Subgroup 10*

Pa	1(a)	2(b)	3(c)	f (mm)
2010 Pa	0.68	1.60	0.58	0.97
0 Pa	0.00	0.00	0.00	0.00
-2012 Pa	0.38	0.79	0.41	0.40
0 Pa	0.00	0.00	0.00	0.00

Table.25: *Results of the frontal deflection in mm section/pressure – Subgroup 11*

Pa	1(a)	2(b)	3(c)	f (mm)
2010 Pa	0.56	5.90	0.66	5.29
0 Pa	0.05	0.06	0.04	0.02
-2012 Pa	1.00	4.57	0.96	3.59
0 Pa	0.01	0.00	0.00	0.01

Table.26: *Results of the frontal deflection in mm section/pressure – Subgroup 12*

Pa	1(a)	2(b)	3(c)	f (mm)
2007 Pa	0.23	1.44	0.38	1,14
0 Pa	0.00	0.00	0.00	0.00
-2008 Pa	0.14	0.85	0.35	0.61
0 Pa	0.00	0.00	0.00	0.00

4. Conclusion

From the analyzed results and their comparison of the individual samples, the following can be confirmed:

- The profile used for producing windows has a minimum influence on the air permeability. The examined samples which were made in the same production capacity, were divided into two groups and six subgroups. Each subgroup had six samples. All the samples of one group had the same fittings, but different type of PVC profile. The samples of the subgroups are of same profile, fittings and dimensions. The results given from the windows slightly differed and they circulated in one class of sustainability of the air permeability. The authors, in the form: initials of the first names followed by last name (only the first letter capitalized with full stops after the initials),

. - The profile used for producing windows has significant influence over the water tightness. The examined samples which were made in the same production capacity, were divided into two groups and six subgroups. Each subgroup had six samples. All the samples of one group had the same fittings, but different type of PVC profile. From the analysed samples a greater water tightness is shown at the windows made of the profile with greater dimensions and bigger sagging of the jamb and side jamb.

- The profile used for production of windows has significant influence over the deformities of the window itself. The examined samples which were made in the same production capacity, were divided into two groups and six subgroups. Each subgroup had six samples. All the samples of one group had the same fittings, but different type of PVC profile.The analysis of the results brought conclusion that the windows are made of profile which is strengthened with more steel making it more resistant to deformities when hit by wind load.

5. References

1. S. Vallabhy1, M. Arun Kumar2, V. Bharath2, E. Dhakshina Moorthy2, Hitesh Kumar Jain2 - DESIGN OF UPVC WINDOWS FOR LATERAL WIND LOADS SANDWICH WITH

HURRICANE BARS FOR MULTISTOREY STRUCTURES (2019)

2. www.rehau.com (28-10-2022)
3. www.alphacan.com (28-10-2022)
4. www.aluplast.net/de/index.php (28-10-2022)
5. www.schueco.com/com/ (12-11-2022)
6. www.koemmerling.com (12-11-2022
7. www.gealan.de/en/ (12-11-2022)
8. www.salamander-windows.com/en (14-11-2022)
9. www.trocal.com (14-11-202)
10. EN 1026:2016 “Windows and doors - Air permeability - Test method” standard
11. EN 1027:2016 “Windows and doors - Water tightness - Test method” standard
12. EN 12211:2016 "Windows and doors - Resistance to wind load - Test method" standard

Study of Vitamin C stability in thermal water for ecofriendly application in the pharmaceutical industry

Sabolč Bognar*, Nina Finčur, Daniela Šojić Merkulov
University of Novi Sad Faculty of Sciences, Department of Chemistry, Biochemistry and Environmental Protection,
Trg Dositeja Obradovića 3, 21000 Novi Sad, Serbia
sabolc.bognar@dh.uns.ac.rs

Abstract: *Free radicals and reactive species of oxygen are destructive for living organisms. Antioxidants are capable to reduce the effect of free radicals and to recover the organisms' health. On the other hand, during the fabrication process various chemicals are released into the water ecosystems from the factories, causing harmful effects on the aquatic organisms. The Autonomous Province of Vojvodina in Serbia is rich in thermal waters. Thankfully to the various minerals, they could have antioxidant effect and could be used as raw material for the production of different pharmaceutical products. In this study we examined the possible effect of different thermal water samples on the degradation rate of Vitamin C as an antioxidant with UV radiation. Furthermore, the influence of initial pH value was also investigated. Our results showed that the thermal water reduced the degradation rate of vitamin C. In addition, the lowest removal rate was observed at initial pH 7, which is close to the skin's natural pH. These findings showed that the thermal water could be used in preparations for skin.*

Keywords*: FREE RADICALS, ANTIOXIDANTS, ENVIRONMENTAL POLLUTION, ECO-FRIENDLY INDUSTRY, THERMAL WATER, STABILITY STUDY, FORCED PHOTODEGRADATION, SKIN PREPARATIONS.*

1. Introduction

Oxygen is an essential element for life. This element is necessary for the basic chemical and biological reactions and without oxygen there would be no energy for cells [1]. Consequently, it is amusing that oxygen can also destroy the living organism [2].Namely, during the ATP degradation by the mitochondria free radicals are produced, which can be both harmful and useful [1]. Reactive oxygen species can also be generated due to environmental factors, such as UV irradiation [3]. At low concentrations they have positive effect on the immune system, while at higher concentrations they can cause oxidative stress and damage living cells. These damages in the living cells result in the development of various serious disorders, such as cancer, arthritis, aging, autoimmune disorders, cardiovascular and neurodegenerative diseases [1].

Based on the mentioned, it is obvious that these substances have to be eliminated in order to keep organisms healthy. The compounds, which are capable to reduce the oxidation of proteins, carbohydrates, lipids and DNA, are known as antioxidants. Antioxidants can be synthetic and natural. The sources of natural antioxidants are most commonly fruits and vegetables. On the other hand, the synthetic sources are mostly drugs, made by various pharmacy companies [4].

Unfortunately, pharmaceutical factories during the production release high amount of wastewater to the natural ecosystem, which results in the appearance of different active pharmaceutical ingredients (API) in the environment. API can cause various, unexpected effects on the non-target organisms. Thus, the amount of released water should be reduced and the wastewater should be adequately treated prior to reaching the water ecosystems [5].

Nowadays, great attention is paid to the personal care products, which are present in aquatic environment at high concentrations. For instance, various UV filters has been found in different water samples, especially in summer, due to the outdoor activities when they are washed from the skin into the water [6].

Based on the mentioned, eco-friendly but effective antioxidants should be found or developed. Fortunately, Serbia and the Autonomous Province of Vojvodina, which belongs to the Pannonia Basin, are very rich in thermal mineral waters. Many of them are used mostly in balneology. Thermal waters in Vojvodina possess above-average geothermal qualities in comparison to the European hydro geological standards and can be successfully applied for medical purposes [7].

In this study, the possible antioxidant effect of thermal water from Kanjiža Spa was investigated, under simulated sunlight. Furthermore, the possible effect of initial pH and mineral concentration on the photodegradation rate was also examined.

2. Materials and methods

Thermal water was sampled from Kanjiža Spa (Kanjiža, Vojvodina, Serbia) and kept in refrigerator. Thermal water was used without further treatment, except the experiments with various mineral concentrations, when 30%, 50%, and 70% of the water samples was evaporated, in order to concentrate the present elements.

For the investigation of the possible antioxidant effect of thermal water, solution of vitamin C (0.05 mM) was freshly prepared prior to photodegradation experiments, dissolving appropriate amount of vitamin C () in ultrapure and thermal water.

The initial pH values were set using 0.1 M $HClO_4$ (70% (*w*/*w*), >99.99%, Sigma−Aldrich, St. Louis, MO, USA) and 0.1 M NaOH (*pro analysis*, MOSS &HeMOSS, Belgrade, Republic of Serbia).

In order to determine the antioxidant efficiency of thermal water, the samples taken after photodegradation were analysed using liquid chromatography with the following components of mobile phase: acetonitrile (99.9%, Sigma−Aldrich, St. Louis, MO, USA) and orthophosphoric acid (85%, pro analysis, Sigma–Aldrich, St. Louis, MO, USA).

3. Sample preparation and analytical procedures

The photodegradation experiments were performed in a photoreactor (TOPT-V, Toption, China). The samples were prepared and irradiated in a photochemical cell made of quartz glass (total volume of ca. 100 mL). The photochemical cells were placed in a circle around the Xe lamp, which was used as simulated solar irradiation (SSI). The cells were equally exposed to the irradiation source. Xenon lamp was in a quartz cold trap, which was equipped with water-circulating jackets and connected to a cooler in order to ensure a constant temperature inside the photoreactor (Fig. 1).

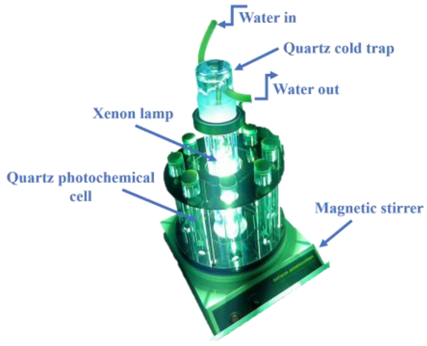

Fig. 1. *TOPT-V photoreactor*

The samples of vitamin C, taken after different times of irradiation (5, 10, 15 and 30 min) using SSI, were firstly filtered through Millipore (Millex-GV, Burlington, MA, USA, 0.22 µm) membrane filter to remove all possible impurities. After that, they were analyzed using a high-pressure liquid chromatograph with a diode array detector (UFLC-DAD, Shimadzu Nexera, Tokyo, Japan) (wavelength of vitamin C absorption maximum at 243 nm) equipped with Inertsil® ODS-4 column (2.1 mm × 50 mm i.d., particle size 2 µm, 30 °C). Prepared samples (20 µL) were injected and analyzed. The mobile phase (flow rate 1.0 mL/min) was a mixture of acetonitrile and water (50:50, *v*/*v*, pH 2.56), while the water was acidified with phosphoric acid so that the mass fraction of phosphoric acid was 0.1%.

4. Results and discussion

Firstly, the degradation of vitamin C was investigated in ultrapure water, under different initial pH values, at pH 10 and 7, using SSI. Based on the obtained results (Fig. 2) it can be seen, that the degradation rate was higher under basic conditions. This can be explained by the auto-oxidation process of vitamin C, which is accelerated under alkaline conditions [8].

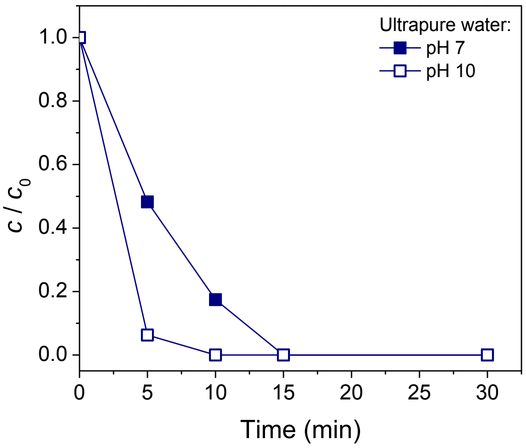

Fig. 2 *Degradation kinetics of vitamin C (0.05 mM) in ultrapure water, under SSI*

In the next step, we investigated the degradation efficiency of vitamin C in thermal water from Kanjiža Spa. There were two different water samples used. Namely, the degradation studies were conducted in pure thermal water (i.e without any treatment) and in samples where 50% of initial volume of water was evaporated in order to increase the concentration of present minerals (Table 1). The experiments were carried out under two different inital pH (10 an 7) and the obtained results are represented in Fig. 3. Based on our findings it can be seen that the degradation rate of vitamin C was higher in the non-treated thermal water compared to ultrapure water at both initial pH. The higher degradation in non-treated thermal water can be explained by the presence of different ions and by the higher natural pH value, which can accelerate the degradation. On the other hand, in the evaporated water samples the degradation of vitamin C under SSI was lower at both inital pH comperated to other samples (Fig. 3). The possible explanation for this behaviour lies in the fact, that the concentration of present cations and anions was higher and reduced the degradation, i.e vitamin C was protected from forced photodegradation under SSI. Furthermore, after 15 min of irradiation the degradation process stopped and no further amounts of vitamin C were degraded in the last 15 min of irradiation.

Table 1. *Chemical characteristics of thermal water from Kanjiža Spa*

Parameter	Value
pH	7.9
Sodium (g/L)	1.298
Potassium (g/L)	0.0097
Lithium (g/L)	0.0001
Ammonium (g/L)	0.0002
Calcium (g/L)	0.0064
Magnesium (g/L)	0.0027
Strontium (g/L)	0.0004
Manganese (g/L)	0.00001
Iron (g/L)	0.00001
Aluminum (g/L)	0.00005
Hydrogen carbonate (g/L)	2.934
Chloride (g/L)	0.073
Bromide (g/L)	0.00013
Iodide (g/L)	0.0006
Fluoride (g/L)	0.0003
Nitrate (g/L)	0.0001
Hydrogen phosphate (g/L)	0.0002
Sulphate (g/L)	0.0009

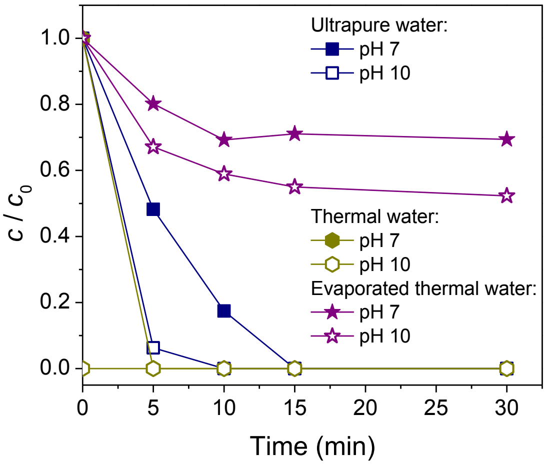

Fig. 3 *Degradation kinetics of vitamin C (0.05 mM) in ultrapure, thermal and evaporated thermal water, under SSI*

Finally, in order to determine the optimal conditions, further experiments were carried out with thermal water evaporated to 30% and 70% (Fig. 4) at initial pH 7 and 10, under SSI. Based on our findings it can be seen that in the samples with thermal water evaporated 30% higher degradation was observed compared to 50% and 70%, after 30 min of irradiation under SSI. It can be explained by the lower concentration of various ions which could not reduce the degradation of vitamin C. On the other hand, in the case of thermal water samples evaporated to 70% lower degradation was observed compared to 30%, but higher compared to 50%. This behavior is probably due to the very high concentration of present ions.

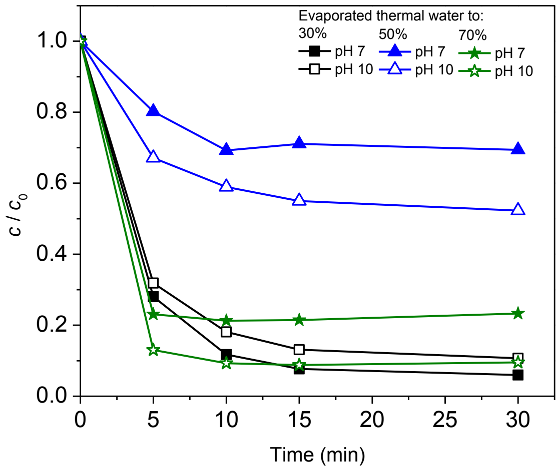

Fig. 4 *Degradation kinetics of vitamin C (0.05 mM) in ultrapure, thermal and evaporated thermal water, under SSI*

5. Conclusion and outlooks

In this study the possible antioxidant effect of thermal water from Kanjiža Spa was investigated. In order to prove this effect, the stability of vitamin C was followed during forced photodegradation under SSI and at initial pH 7 and 10. Firstly, our findings showed a different behaviour of vitamin C in ultrapure and thermal water. Based on the obtained data it also can be concluded, that in alkaline medium, both in ultrapure and thermal water, the degradation rate was higher, which can be the result of vitamin C auto-oxidation, which is more intense above pH 7. The influence of present ion concentration on the photodegradation efficiency was examined, as well. Namely, thermal water was evaporated to 30%, 50% and 70% in order to reach different concentration of the present natural cations and anions in the samples. According to the obtained data, the lowest vitamin C degradation was achieved when 50% of thermal water was evaporated. Whereas, in the case of 30% and 70% the degradation efficiency was higher. The reduced photodegradation rate of vitamin C in the case of 50% indicates a possible antioxidant effect of thermal water, since the irradiated compound was protected from the total degradation.

Our findings indicate that evaporated thermal water to 50% could be used as an antioxidant and has potential application in pharmaceutical industry. Namely, different preparations could be developed, for instance skin care products, using an eco-friendly, natural resource instead of chemicals. Furthermore, various experiments should be carried out in order to determine the possible use of thermal water as an active pharmaceutical ingredient, which would make pharmacy and medicine more sustainable.

6. Acknowledgement

The authors acknowledge the financial support of the Provincial Secretariat for Higher Education and Scientific Research (Grant Number 142-451-2367/2022-01/01) and the Science Fund of the Republic of Serbia (Grant No 7747845, *In situ* pollutants removal from waters by sustainable green nanotechnologies-CleanNanoCatalyze).

7. References

1. L. A. Pham-Huy, H. He, C. Pham-Huy, Int. J. Biomed. Sci. **4** (2009), 89−96.
2. V. Lobo, A. Phatak, N. Chandra, Pharmacogn. Rev. **4** (2010), 118−126.
3. J.-Y. Meng, C.-Y. Zhang, F. Zhu, X.-P. Wang, C.-L. Lei, J. Insect Physiol. **55** (2009), 588−592.
4. V. Sindhi, V. Gupta, K. Sharma, S. Bhatnagar, R. Kumari, N. Dhaka, J. Pharm. Res **7** (2013), 828−835.
5. J.L. Wilkinson, A.B.A. Boxall, D.W. Kolpin, (…) and C. Teta, PNAS **119** (2022), Art. No. e2113947119.
6. M. Picot Groz, M.J. Martinez Bueno, D. Rosain, H. Fenet, C. Casellas, C. Pereira, V. Maria, M.J. Bebianno, E. Gomez, Sci. Total Environ. **493** (2014), 162−169.
7. M. Bubalo-Živković, T. Lukić, B. Đerčan, R. Stojsavljević, D. Bjelajac, B. Ristanović, Zbornik radova – Geografski fakultet Univerziteta u Beogradu **66** (2018), 53−70.
8. X. Yin, K. Chen, H. Cheng, X. Chen, S. Feng, Y. Song, L. Liang, Antioxidants, **11** (2022), Art. No. 153.

Studying the surface and microstructure of a chromium coating with nanodiamond particles deposited on monolithic composite with layered structure

Vladimir Petkov[1,*], Mihaela Aleksandrova[1], Radoslav Valov[1], Valery Korzhov[2], Vyacheslav Kiiko[2], Tatyana Stroganova[2]
[1] Bulgarian Academy of Sciences, Institute of Metal Science, Equipment and Technologies with Center for Hydro- and Aerodynamics "Acad. A. Balevski", 67 Shipchenski Prohod Blvd, 1574, Sofia, Bulgaria
[2] Institute of Solid State Physics, Russian Academy of Sciences, 2 Akademik Osilyan str., Chernogolovka, Moscow Region, 142432, Russia
vladimir2pe@yahoo.com

Abstract: *Electrochemical coatings of chromium modified with nanodiamond particles applied directly on niobium-aluminum alloy were obtained. Nanodiamond particles produced by detonation synthesis were used. Chromium coatings were deposited on a monolithic composite with a complex structure based on niobium and aluminum alloys, called later matrix for short. Standard chromium electrolyte and electrolyte with nanodiamond particles concentration of 10 g/l were used. Analyzes were performed by Scanning Electron Microscope system of Bruker Inc. and the Polyvar Met metallographic microscope. The microhardness was measured using a PolyvarMet 4000 microhardness tester. The obtained results of the microhardness were 788 kg/mm*^{2} *in the chromium layer and 168 kg/mm*^{2} *and 692 kg/mm*^{2} *in the matrix. The microstructural and SEM-EDS analysis showed the presence of two intermetallides* Nb_2Al *and* Nb_3Al *in the monolithic composite of niobium aluminum matrix. The average thickness of the chromium coatings modified with nanodiamond particles is 55 μm.*

Keywords*: CHROMIUM COATING, NANODIAMOND PARTICLES, NIOBIIUM ALUMINUM MATRIX, MICROSTRUCTURE*

1. Introduction

High-temperature monolithic composites with layered structures are usually obtained by pressing at certain temperature of bundled layers of various metal foils and powders such as: Mo-Al, Nb-Al, Nb-Al-Ti, Cr-Al-Nb [1], Mo-Nb-B-Si [2] and others. In our case, we consider a composite of niobium (niobium alloy with 0.1% carbon) and aluminum foils pressed at 1-2 MPa at a temperature of 1300°C in vacuum.

In the binary system Nb-Al the main phases are: $NbAl_3$, Nb_2Al and Nb_3Al [3]. According to some authors the phases Nb_7Al_3 and $Nb_{17}Al_3$ also coexist [4]. The first attempt to use the batch rolling method to obtain a monolithic composite was made to densify aluminum and niobium foil at a temperature of 300°C [5].

To improve the properties of this type of monolithic composite (MC) such as heat resistance, microhardness, wear resistance, corrosion resistance, they are electrochemically coated with metallic chromium. The composite chromium coatings modified with nanodiamond particles deposited on various metals and alloys such as steel, aluminum, etc. additionally contribute to increasing the above-mentioned properties. [6, 7, 8].

In the present research the main aim was to obtain composite chromium coatings with diamond nanoparticles deposited directly on a monolithic composite based on a niobium aluminum matrix with a layered structure. Their structure and morphology were studied on the one hand, and on the other hand, the thickness of the coating and its microhardness were determined. A uniform and dense layer of chromium with nanodiamonds with thickness of about 55 μm was obtained. The microhardness in the chromium layer is about 800 kg/mm^2, in the matrix close to the chromium layer it is about 170 kg/mm^2 and in the middle of the sample it is about 700 kg/mm^2.

Any application of coatings, regardless of the type of metal matrix, is carried out by preliminary removing of the oxide layer from the metal surface immediately before depositing the coating. In our case, a series of oxide layers of the main elements Nb and Al, from which the monolithic composite was obtained, must be removed. Multicomponent alloys are usually chemically treated with a series of acids and their mixtures and bases also in some cases. Electrochemical polishing in appropriate electrolyte solutions is also used to remove the oxide layers.

2. Experimental data

The objective of the study is to obtain a chromium coating with nanodiamond particles on a monolithic composite with a layered structure obtained on the basis of a niobium alloy with 0.1% carbon and aluminum. The phase composition, microstructure and elemental composition in different areas of the matrix and of the chrome coating were investigated. The primary test samples are rectangular tiles with dimensions - 30 x 20 mm and height h - 1.5 mm. Figure 1 shows some of the chromium-coated test samples shot with an optical microscope (LM). There, the structure of the chromium coating surface was shot with magnification marked A x20 and B x80 with different levels of illumination. The chromium coating follows the surface of the monolithic composite sample with a layered structure that is slightly rough with elongated stripes. The basic chromium coating has a slightly wavy structure with fine grains, which is more clearly observed in (Fig. 1B).

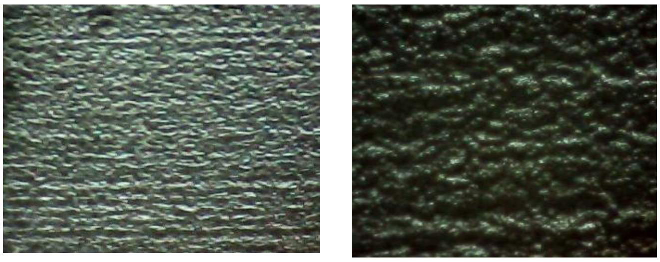

A, x20 *B, x80*

Fig. 1 *Chromium coating with ND deposited on the niobium aluminum matrix with magnification A x20 and B x80*

Short description of the preliminary treatment (technological process) for obtaining chromium coatings with ND on MC of the niobium aluminum matrix (alloy): The samples are first grinded, then degreased and etched with a mixture of acids. The niobium alloys are usually cleaned of the surface oxides with a mixture of the acids HF, HNO_3, H_3PO_4 in a ratio of 1:1:1 or 1:1:2 [9]. Finally they are immersed in a special acid-alkaline solution [10] before connected to the cathode and immersed in the chromium plating electrolyte.

The preliminary chemical treatment is extremely important for obtaining a uniform, dense and well-adhered chromium coating. Otherwise, the coatings crack, peel or do not adhere well to the metal matrix. In the present study a standard chromium plating electrolyte was used with chromic anhydride:sulfuric acid ratio of 100:1 [6, 10]. It has the following chemical composition: CrO_3 – 220 g/l; H_2SO_4 - 2.2 g/l.

The electrochemical parameters of the process are:

Current density: 45 A/dm^2

Duration: approx. 45 min

The electrolyte temperature: approx. 50^{o}C

Two electrolytes are prepared. The first is the standard chromium electrolyte described above and the second one is with the nanodiamond particles. It is in the form of an aqueous suspension with an ND concentration of 10%. The suspension with ND was then activated in an ultrasonic bath, after which the resulting electrolyte is added to the standard electrolyte for chromium plating with a final concentration of nanodiamonds of 10 g/l. The previously treated niobium aluminum samples connected to the cathode are immersed in the obtained in this way electrolyte and the electrodeposition of metallic chromium is carried out. The final result of the chromium plating of the niobium aluminum matrix is shown in (Fig. 1).

3. Research, results and discussion

3.1. X-ray structural analysis

Investigations were done with a Bruker D8 Advance powder X-ray diffractometer. The Bruker DIFFRAC.EVA program was used to determine the qualitative and quantitative phase analysis.

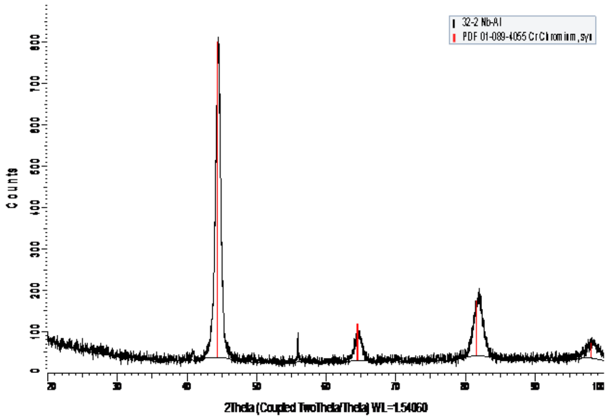

Fig. 2 *Diffractogram of chromium coating with diamond nanoparticles deposited on MC of the niobium aluminum matrix designated as(32-2Nb-Al)*

In the diffractogram in Fig. 2 one phase of metallic chromium with a cubic structure is found, which is evidence of a good density of the chromium coating.

3.2. Microstructure and microhardness

The microstructure of the chromium coating with ND deposited on MC of niobium aluminum alloy was imaged with a "Polyvar Met" metallographic microscope (Fig. 3). The chromium coating was prepared from electrolyte with concentration of nanodiamonds in the electrolyte 10 g/l. The microhardness in the chromium layer was about 800 kg/mm^2, which is typical for chromium coatings with ND. It was determined using a PolyvarMet 4000 microhardness tester (Fig. 3). In the matrix with a layered structure it is 168 kg/mm^2 which we assume was measured in the aluminum and niobium solid solution and it was about 690 kg/mm^2 most likely measured at the obtained intermetallyde Nb_2Al.

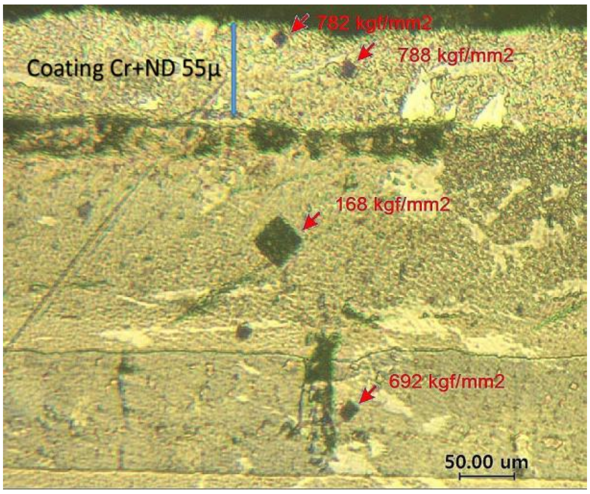

Fig. 3. *Microstructure and microhardness of chromium coating with nanodiamond particles deposited directly on MC of niobium aluminum alloy*

The chromium layer is 55 µm thick, uniform and dense, following the surface of the monolithic composite of the niobium aluminum matrix. (Fig. 3).

3.3. Surface morphology and elemental composition determination

The studies were carried out using a scanning electron microscope "HIROX SH-5500P" with an EDS system "QUANTAX 100 Advanced" with accelerating voltage: from 1 to 30 kV. In Fig. 4 A the chromium coating is observed which is in gray. The coating in Fig. 4 B is in black and its border is hardly distinguishable from the final border with the resin with which the sample is prepared. The SEM examination of the chromium coating deposited on MC of the niobium aluminum matrix is surrounded by a yellow square marked with the number 3.

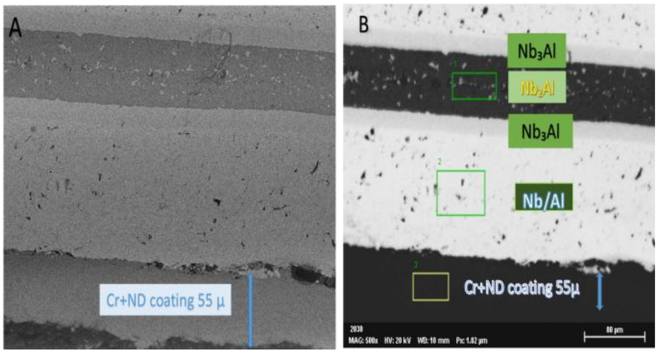

Fig. 4. *SEM image of a chromium coating with nanodiamond particles deposited on a MC of a niobium aluminum matrix*

The surface was investigated at magnification x500 and it consists of continuous and uniform layer of chromium with nanodiamond particles with thickness approximately 55 µm thick.

1

Element	At. No.	Netto	Mass [%]	Mass Norm. [%]	Atom [%]	abs. error [%] (1 sigma)	rel. error [%] (1 sigma)
Nb	41	13931	47.53	50.84	18.28	1.84	3.88
Al	13	17517	33.31	35.62	44.09	1.66	4.98
C	6	311	12.65	13.53	37.63	4.16	32.88
		Sum	93.49	100.00	100.00		

2

Element	At. No.	Netto	Mass [%]	Mass Norm. [%]	Atom [%]	abs. error [%] (1 sigma)	rel. error [%] (1 sigma)
Nb	41	40929	91.38	88.05	49.56	3.42	3.74
C	6	422	11.74	11.32	49.26	3.49	29.69
Si	14	539	0.66	0.63	1.18	0.07	10.82
		Sum	103.78	100.00	100.00		

3

Element	At. No.	Netto	Mass [%]	Mass Norm. [%]	Atom [%]	abs. error [%] (1 sigma)	rel. error [%] (1 sigma)
Cr	24	29844	82.11	94.55	86.40	2.29	2.79
C	6	186	2.52	2.90	11.49	1.02	40.30
Nb	41	457	1.62	1.86	0.95	0.13	8.29
Si	14	244	0.59	0.68	1.16	0.08	13.17
		Sum	86.84	100.00	100.00		

Figure 4 shows the examined in zones and characterized by SEM-EDS analysis of the surface of the chromium coating with ND and of the niobium aluminum matrix. The elemental composition was determined in three zones: In zone 1 the intermetallyde Nb_2Al was found according to the elemental composition and microstructural analysis from. In zone 2 it was a solid solution of niobium and aluminum in the niobium aluminum matrix. And in zone 3 it was only the chromium layer with diamond nanoparticles.

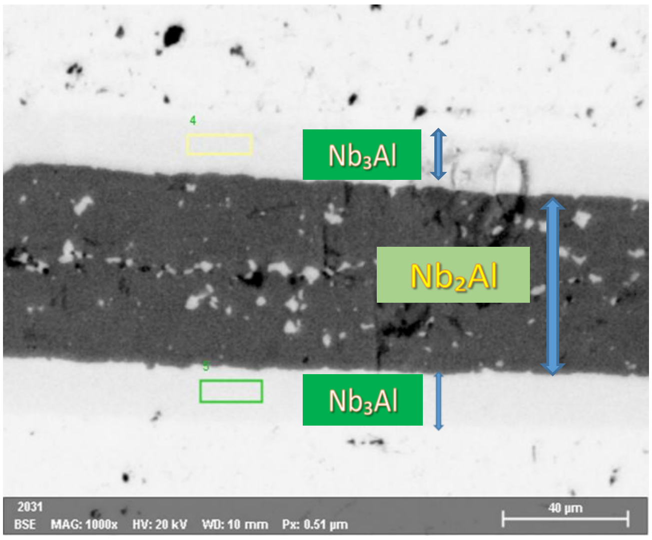

Fig. 5*. SEM image of zone study of the monolithic composite with a layered structure based on a niobium aluminum matrix*

Figure 5 shows the zone examination and characterization by SEM-EDS analysis of MC of the niobium aluminum matrix. The elemental composition is determined in two zones: 4 and 5, where the intermetallyde Nb_3Al is most likely to be found, and the broad dark band is the intermetallyde Nb_2Al.

The data from the studies in a Nb/Al matrix are shown in the zone marked with 4. The main elements are Nb, Al, C and traces of Si.

4

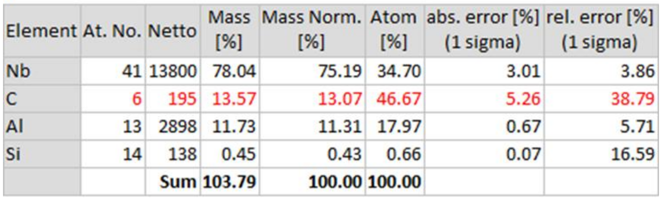

Element	At. No.	Netto	Mass [%]	Mass Norm. [%]	Atom [%]	abs. error [%] (1 sigma)	rel. error [%] (1 sigma)
Nb	41	13800	78.04	75.19	34.70	3.01	3.86
C	6	195	13.57	13.07	46.67	5.26	38.79
Al	13	2898	11.73	11.31	17.97	0.67	5.71
Si	14	138	0.45	0.43	0.66	0.07	16.59
		Sum	**103.79**	**100.00**	**100.00**		

In zone 5, the yellow rectangle in Fig. 5 the data from the studies inside the matrix are presented, from which it is clearly seen that the quantities of the main elements match and are approximately the same in mass percentages as those of zone 4.

The identified carbon, although with a large error, is very likely to be from the nanodiamonds used in the chromium plating electrolyte (Fig. 4), zone 3 and/or from the carbon content of the niobium alloy used together with aluminum foil to produce a monolithic composite with a layered structure (Fig.5), zone 4 and 5.

5

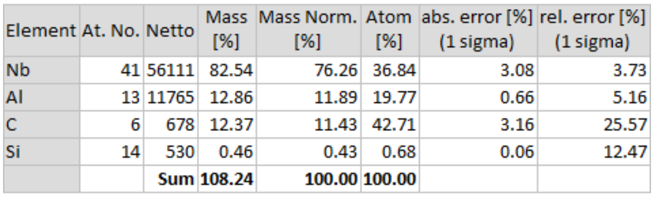

Element	At. No.	Netto	Mass [%]	Mass Norm. [%]	Atom [%]	abs. error [%] (1 sigma)	rel. error [%] (1 sigma)
Nb	41	56111	82.54	76.26	36.84	3.08	3.73
Al	13	11765	12.86	11.89	19.77	0.66	5.16
C	6	678	12.37	11.43	42.71	3.16	25.57
Si	14	530	0.46	0.43	0.68	0.06	12.47
		Sum	**108.24**	**100.00**	**100.00**		

4. Conclusions:

Electrochemical chromium coatings with ND were deposited directly on a monolithic niobium aluminum matrix composite.

The presence of chromium with a cubic structure in the coating was determined by X-ray structural analysis.

The chromium coatings with ND were found to be dense, discontinuous, following the surface of the monolithic niobium aluminum matrix composite with a layer thickness of about 55 μm.

It was found that the microhardness in the chromium coating is nearly 15 % more than that measured in the Nb_2Al intermetallyde obtained in the niobium aluminum matrix.

The microhardness in the chromium coating was found to be nearly 5 times greater than that measured in the Al/Nb solid solution obtained in the niobium aluminum matrix.

The presence of two intermetallydes Nb_2Al and Nb_3Al was determined by microstructural and SEM-EDS analysis.

SEM-EDS analysis determined the presence of carbon in the samples, most likely from the niobium alloy (Nb01C) in the matrix and traces of carbon in the chromium coating, which are most likely from the diamond nanoparticles which proves their participationin the structure of the layer.

5. Acknowledgments

5.1. This study was performed with the financial support of the Fund “Scientific Researches” (research project No KP-06-Russia/18, date 15.12.2020)

5.2. The work was supported by RFBR grant 50-53-18002

6. References

1. F. Stein, H. Cuiyun, I. Wossack I, J. of Alloys and Comp. **598**, 253–265 (2014)
2. T. Yang, X. Guo, 2019, *Metals*, **9**, 653 (2019)
3. A. da Silvaa, G. Coelhob, C. Nunesb, J. Fiorani, N. David, M. Vilasi, Mat. Res., **22**, 5 (2019)
4. M.J. Richards, Jour. Mét., 1-12, (1962)
5. A. Nishimoto, K. Akamatsu, Mat. Sci. Forum, **634**, 1390 (2010)
6. V. Petkov, R. Valov, S. Simeonova, M. Kandeva, Arch. of Foundry Eng., **20**, 115, (2020)
7. N. Gidikova, M. Sulowski, V. Petkov, R. Valov, G. Cempura, Arch. Metall. Mater, **62,** 2421-2424 (2017)
8. N. Gidikova, A. Cias, V. Petkov, M. Madej, M. Sulowski, R. Valov,. Arch. Metall. Mater, **59**, 1523, (2014)
9. V. Palmieri, F. Stivanello, S.Yu., The 10th Workshop on RF Superconductivity, Tsukuba, Japan, (2001)
10. N. Gidikova N., **V.** Petkov, R. Valov, BG Patent 67042B1, (2020)

Formation of the structure of polymeric products on the based of polyamide 6 produced by fdm-printing

Alexander Skaskevich[1], Valery Sarokin[1], A. Sudan[1], A.N. Gaiduk[1], Angel Velikov[2]
Yanka Kupala Grodno State University[1] – Grodno, Belarus, Bulgarian Academy of Sciences, Institute of Metal Science, Equipment and Technologies with Center for Hydro- and Aerodynamics "Acad. A. Balevski",, Bulgaria[2]
E-mail: askas@grsu.by, sorvg@grsu.by, anmabg@abv.bg

Abstract: *An analysis of the prospects for the development of FDM printing technology has been carried out. The paper studies the possibility of obtaining polymer products based on polyamide 6 and its compositions by layer-by-layer deposition. Tests of the strength indicators of the printed experimental products were carried out. The mechanism of the influence of the composition and modes of formation of printed products on their strength characteristics is proposed. The influence of the composition of the composite polymer material based on PA6 on the quality of printing products has been studied. Methods for controlling the shrinkage parameters of products obtained by layer-by-layer deposition are proposed. The obtained results of the study can be used in the development of composites for the production of polymer filament to ensure the process of FDM printing of polymer products, including for the needs of mechanical engineering.*

KEYWORDS: *FDM PRINTING, POLYAMIDE 6, TECHNOLOGICAL PARAMETERS, TENSILE STRENGTH, RELATIVE ELONGATION, POLYMER PRODUCTS*

1. Introduction

The production of polymer products using additive technologies has become available due to the intensive development of the production of FDM printers, as well as consumable polymer materials (filaments), which allows solving various production problems. At the same time, during the printing process, control over the main operational characteristics of products is ensured by choosing the composition of the polymer filament, as well as the technological settings of the FDM printer. In the Republic of Belarus, aliphatic polyamides and composites based on them are actively and effectively used for the production of structural products with high values of consumer characteristics of the widest range. At the same time, the effective processing of polyamides into products and the realization of the advantages and advantages of the indicated thermoplastic polymer when using various technologies are hampered by high values of hygroscopicity (up to 12 wt.% with an acceptable value during processing of 0.05-0.1 wt.%) and thermal shrinkage (up to 2.5% for unfilled materials) polyamide 6. For the active use of polyamide 6 in additive technologies, this is a significant drawback that affects the quality of the resulting products. And if polyamide processors effectively cope with a high tendency to moisture absorption by pre-drying the raw material and using heating of the material in the loading zone of the process equipment, then the thermal shrinkage of the binder requires more complex solutions. Most often, it is possible to reduce the thermal shrinkage of the polyamide matrix by modifying it with polymer components [1], as well as by introducing dispersed and (or) fibrous fillers [2]. At the same time, glass fibers in the composition of polyamide 6 can significantly increase the level of deformation and strength parameters of products, and carbon fibers increase impact strength and wear resistance. Polyamide 6 and composites based on it are mainly processed into products by injection molding due to the high values of the melt flow parameter. The use of PA6 for FDM printing in products seems difficult due to the high melt fluidity (MFR PA6 210/310 is more than 20 g/10 min), and therefore the use of composite compositions based on it for 3D printing is promising.

In modern conditions of limited availability of the raw material base, as well as increasing logistics costs for the supply of material resources and components of machine-building equipment, it is promising to study the possibility of using domestic polymer composite materials to obtain piece products in the conditions of enterprises operating and maintaining equipment that includes products based on polymer materials.

Thus, the purpose of the work is to substantiate the feasibility and effectiveness of using a polymer filament based on polyamide 6 and its composites for printing polymer products by the layer-by-layer deposition method.

2. Materials and Methods

To study the features of the formation of the structure of the material in products obtained by 3D printing, in this article, the authors used polyamide PA6-210/310 (Grodnamid) TU RB 500048054.009-2001 in granules produced by GrodnoAzot OJSC, carbon fiber UPA6-10 TU RB 00204056-086-94 in granules produced by OJSC SvetlogorskKhimvolokno, composite material PA6 + 10 wt.% HDPE, obtained by thermomechanical combination of components during extrusion. To study the parameters of polymer products, a filament with a diameter of 1.75 mm was obtained for these materials by extrusion on a Z-7M laboratory extruder (Russia) in modes that take into account the rheological characteristics of the starting materials. The parameters of the extrusion process when obtaining a filament are shown in Table 1.

Table 1: *MFR values for PA6-210/310 (Grodnamid)*

Options	Material		
	PA6-210/310	UPA6-10	ПА6+10 mas.% HDPE
Cylinder temperature by zones, °C (±10°C)	230	230	230
Head temperature, °C (±10°C)	240	240	240
Feed-screw speed, rpm	20	10	20
Retraction speed, m/min	0,9	0,5	0,8

Previously to printing product samples, the polymer filament was subjected to thermostating in an oven at a temperature of 95 ± 5 °C for 4 hours to reduce the moisture content by no more than 0.1 wt%. To assess the deformation-strength characteristics of materials under uniaxial tension and to study the features of the formation of the structure of materials during layer-by-layer deposition, a product was printed in the form of standard blades (type 1) GOST 11262-80 on an Ultimaker 3 3D printer. The FDM printing parameters of the blades were set in the CraftWare 1.19 slicer program. A series of 6 standard samples was printed in the given technological parameters of the print settings per cycle (table 2). Evaluation of the deformation-strength characteristics of the studied samples was carried out on a tensile testing machine RM-500 in the mode of uniaxial tension at a speed of 10 mm/min with fixation of the deformation and tensile force. It was of interest to investigate the mechanism of the formation of autohesive bonds within the slab space and between the layers of a polymer product during the manufacture by the method of layer-by-layer deposition. The resulting samples of polymer products in the form of blades with different orientations in the intralayer volume (± 45° and 0°/90°) were subjected to 5% deformation in uniaxial tension for further study of brittle cleavage of product images obtained in the longitudinal direction of the tension axis. The structure of the materials was studied by scanning electron microscopy on blades that were brittle fractured after soaking in liquid nitrogen. At the same time, in order to manifest the effects of interlayer autohesion and study the effect of fillers on the structure of composites in the product, the blades were subjected to deformation within a 5% elongation under uniaxial tension. It was of interest to analyze the interaction of the polyamide-based filament melt in the interlayer and intralayer locations.

Table 2: *Parameters of print settings for test samples*

Basic print settings	PA 6	UPA 6-10	PA6+10 mas.% HDPE
The speed of movement of the nozzle of the extruder during printing, mm / sec	40	20	40
Print layer thickness, mm	0,2	0,2	0,2
Print width, mm	0,4	0,4	0,4
Number of layers of the perimeter of the product	2	2	2
Table temperature, ℃	100	70	100
Extrusion Temperature,℃	250	250	240
Unspecified print settings were the same for all samples			

3. Results and discussion

As a result of visualization of internal stresses arising in a polymer material obtained by layer-by-layer deposition of Nylon, a higher level of stresses arising in the peripheral part of the material, in comparison with the volume [3], was shown. In this case, the level of internal stresses decreases with a decrease in the degree of filling of the product volume with a polymer melt. It was shown in [4,5] that the degree of filling of the volume of the material affects the dimensional stability of products obtained by layer-by-layer deposition. At the same time, a number of research authors indicate [6,7,8] that the highest values of the deformation-strength characteristics of the material in the product are achieved at zero angles of orientation of the printing direction to the tension axis. However, to ensure the isotropy of strength indicators, layer-by-layer filling of the volume of the product was carried out in the “parallel lines” mode, changing the direction of printing in the next layer by 90 º, as recommended by many researchers [6,8].

The analysis of the morphology of the brittle fracture surface of blade samples based on UPA 6/10 carbon fiber, obtained by FDM printing with polymer orientation ±45º inside the layers when filling the volume of the product, was carried out on SEM images of the surface shown in Figure 1. A snapshot of the sample surface within the interlayer brittle The cleavage is shown in Figure 1a, which shows several adjacent layers of fibers with print orientation in the layer at angles of +45° and -45°. In Figure 1a, several important morphological features of the destruction of the polymer binder can be distinguished: interlayer voids resulting from the 3D printing process, layers with a rough fracture surface morphology, and layers with a smoother surface. For a detailed display of the nature of the contact of adjacent layers, an increase in the survey area is given (Figure 1b). The presented images indicate that between the threads between the layers, insufficient adhesion is characteristic along the tension axis, at which the formed crack grows. A rough fracture surface can also be noted in the interlayer region where fibrillation of the polymeric binder is noted with the formation of filamentous fragments.

This nature of the destruction of UPA 6/10 carbon fiber suggests that the binder layers oriented perpendicular to the tension axis hinder the growth of cracks. In this case, the participation of the remaining layers of the material in the mechanism of resistance to destruction of the matrix can be considered insignificant due to insufficient adhesion between them, due to the limited mobility of the binder polymer filled with carbon fibers.

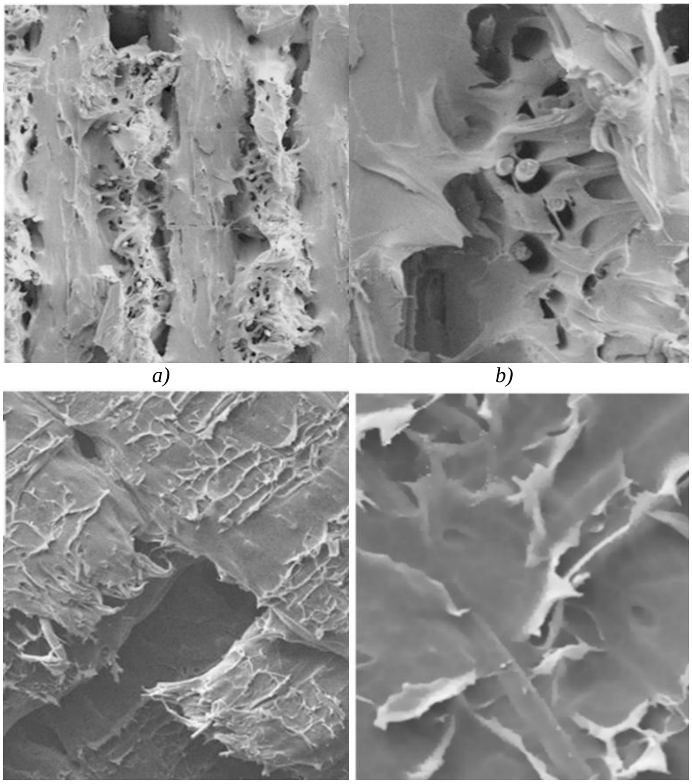

a) b)

c) d)

a) general view of the fracture surface morphology of the sample in the interlayer location (magnification ×100); b) close-up of surface features in adjacent layers (×500 magnification); c) general view of the fracture surface morphology of the sample in the intralayer location (magnification ×100); d) close-up of surface features within the layer (×500 magnification)

Figure 1 *SEM images of brittle fracture surfaces of samples with a print orientation of ± 45°*

The role of short elements of carbon fiber contained in the PA6 matrix in the process of deformation destruction of the layered structure of a carbon fiber product is also noticeable. Fibrillation of the polymer matrix during uniaxial tension of the carbon-filled PA6 sample suggests the implementation of a local mechanism of strengthening the polymer matrix in the product formed by the FDM-printing method.

At the same time, within the imprinted layer, a sufficiently strong autohesive adhesion is observed in the intralayer location of the matrix, which is observed in the image of the brittle fracture morphology of the sample (Figure 1c). This is due to the good rheological characteristics of PA6, which contribute to the realization of the phenomenon of autohesion between the polymer threads within the printed layer. Figure 1d shows that the traces of fracture surface roughness are concentrated along short fibers. This fact confirms the assumption that short carbon fibers enhance autohesion during FDM printing of polymer products based on carbon fiber.

Figure 2 shows SEM images of the brittle cleavage surfaces of specimens based on UPA6-10 carbon fiber obtained with the printing direction oriented in the 0º/90º layer. The surface of a brittle fractured sample, representing the interlayer space of the matrix, is shown in Figure 2 a. The image shows layers located at an angle of 0º and at an angle of 90º. At the same time, layers at an angle of 0º under conditions of preliminary 5% deformation have a rough surface, and layers at an angle of 90º retain a smooth appearance. An enlarged view of the cleavage surface of this sample is shown in Figure 2b. It should be noted traces of stretching of the fibers in the layers located at an angle of 0º, which indicate the course of the processes of fibrillation of the polyamide binder during deformation.

The surface morphology of a brittle cleavage of a sample of the studied carbon fiber with a polymer orientation angle of 0º/90º demonstrates a similar morphological pattern, as in the case of printing products with an orientation of ± 45º. The brittle fracture surface of CFRP contains traces of piles of polymer fibrils of destroyed threads. The presented images indicate some similarity of the fracture mechanism in the case of deformation of the sample obtained by printing with an orientation of ± 45º.

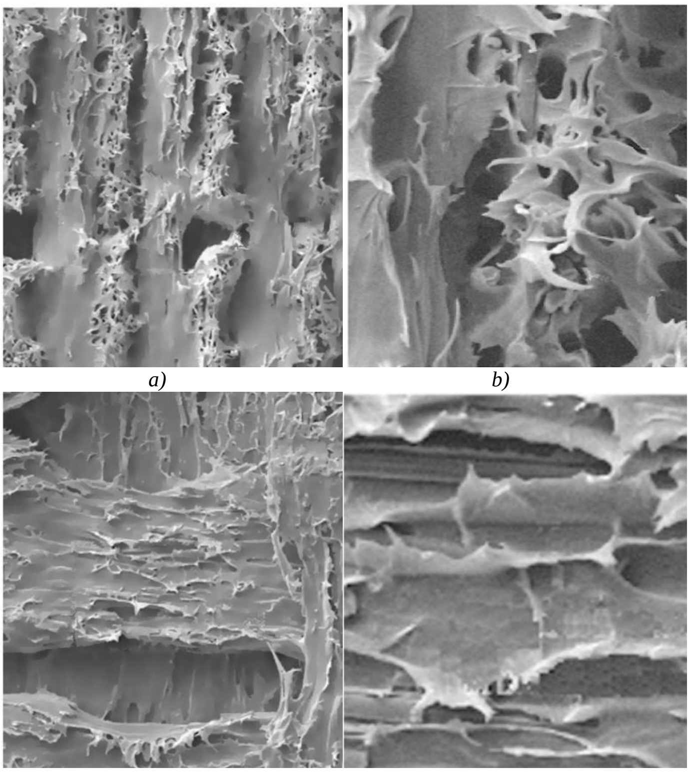

a) general view of the fracture surface morphology of the sample in the interlayer location (magnification ×100); b) close-up of surface features in adjacent layers (×500 magnification); c) general view of the fracture surface morphology of the sample in the intralayer location (magnification ×100); d) close-up of surface features within the layer (×500 magnification)

Figure 2 *SEM images of brittle fracture surfaces of specimens with print orientation 0º/90º*

An analysis of the features of the operation of the specified product indicates the predominant destruction in the place of the most weakened section, located between the body of the pusher and the surfacing. An example of a destroyed product is shown in Figure 3.

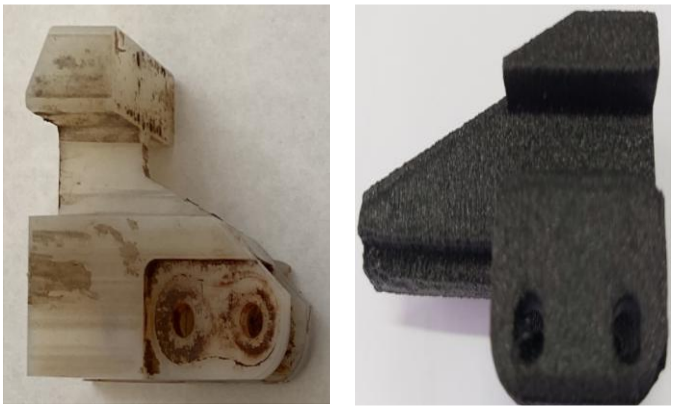

Figure 3 *Appearance of the products "Pusher F08575326" (a) and "Pusher 406.42.0490" (b), obtained by injection molding (a) and FDM printing technology (b)*

3. Conclusion

Thus, the results of the study of the accuracy parameters of FDM printing of polymer products based on PA6-210/310 (Grodnamid), as well as the indicators of their deformation and strength characteristics, indicate the promise of using polyamide both in the initial state and in the state of the composite. The printing efficiency of PA6 in the product is achieved by ensuring a stable geometry of the polymer filament, as well as choosing the optimal printing temperature not exceeding 250℃. The obtained results of the work can be taken into account when determining the technological modes of production of filaments based on PA6, as well as when choosing the modes of FDM printing of thin-layer elements of polymer structures and elements of parts that are most loaded during operation. The data obtained indicate the prospects for conducting scientific research in the creation of materials based on aliphatic polyamides and their composites, as well as studying the influence of technological factors in the process of processing polyamide filaments into products by FDM printing.

4. References

1. Nanocomposite and nanostructured engineering materials and technologies for their production. Monograph / S.V. Avdeychik and [others], Ed. A.V. Kirichek. – M.: Spektr Publishing House, 2013. – 224 p.
2. Liopo, V. A. Physical bases of polymer modification with doping additives of layered minerals / V. A. Liopo, G. A. Kuznetsova, V. A. Struk, A. A. Skaskevich // Materials, technologies, tools. - 2002. - T. 7, No. 4. - S. 54-58.
3. Skaskevich, A. A. Influence of technological parameters of FDM-print on the strength characteristics of samples of polyamide / A. A. Skaskevich, A. Sudan, D. Dzhendov // Machines. Technologies. Materials. – 2020. – T. XIV. – № 5. – C. 210-212.
4. Skaskevich, A. A. Features of the formation of the structure of polymer products based on carbon fiber plastics obtained by the FFF-printing method / A. A. Skaskevich, A. S. Sudan // Petrochemistry-2021: materials of the IV Intern. sci.-tech. forum on chem. technologies and oil and gas processing, Minsk, November 22-23. 2021 - Minsk: BSTU, 2021. - S. 88-91.
5. Sudan, A. On the prospects for the production of filaments based on polyamide 6 for FDM printing / A. Sudan, A. N. Gaiduk, A. A. Skaskevich // Bulletin of Yanka Kupala Grodno State University. Ser. 6. Technique. - 2021. - T. 11. - No. 2. - S. 83-90.
6. Kondrashov, S.V. Influence of technological modes of FDM printing and the composition of the materials used on the physical and mechanical characteristics of FDM models (review) / S.V. Kondrashov [and others] // Proceedings of VIAM. - T.82, No. 10. - 2019. - S. 34-49.
7. Nefelov, I.S., Baurova, N.I. Ways to prevent technological defects in machine parts manufactured using additive technologies / I.S. Nefelov, N.I. Baurova // Bulletin of modern technologies. - No. 5. - 2017. - P.36-40.
8. Erofeev, V.T. Study of the physical and mechanical characteristics of polylactide samples in additive technology / V.T. Erofeev [et al.] // Building materials and products. - Number 3. - 2019. - P.92-101.

Technology and technological scheme of a workshop for the production of beehives made of amorphous quartz ceramics

Lyuben Lakov, Todorka Lepkova, Gacheva M., Krasimira Toncheva, Gabriel Peev, Dimo Mihaylov

Bulgarian Academy of Sciences, Institute of Metal Science, Equipment and Technologies with Hydro- and Aerodynamics Centre „Acad. A. Balevski”, 67 "Shipchenski Prohod" Blvd, 1574 Sofia, Bulgaria,
e-mail: mvgacheva@abv.bg; krasiton4@abv.bg

Abstract: *The development refers to an innovative technology and technological scheme of a workshop for the production of beehives made of amorphous quartz ceramics. The conditions for obtaining stable suspensions from quartz glass are emphasized and investigated. The time for the treatment of the glass in the grinding device, the amount of water, the influence of the modifiers in stabilizing the suspension by adjusting the pH level, as well as the most suitable sedimentary composition of the glass particles are established. The factors determining the speed and degree of sintering of the ceramics are investigated and established. They include the density of the raw products, the dispersion of the quartz glass particles and its purity, as well as the environment in the furnace and the sintering mode.*

Keywords: *BEEHIVE, AMORPHOUS CERAMICS, SUSPENSION, SEDIMENT COMPOSITION*

1. Introduction

Quartz ceramics is a sintered material made of ground quartz glass, which is molded using the known ceramic technologies. The resulting products are opaque and white in color. Quartz ceramic is the only ceramic material made not of crystals but of a vitreous phase. There is no material better suited for building beehives than quartz ceramics, as it is an extremely pure material which, as opposed to marl clays on their own or mixed with kaolin, does not contain any other mineral phases apart from amorphous silica.

Quartz ceramic is applied in many areas where ordinary quartz glass is also used. This is due to its high thermal stability, the stability of its thermophysical properties and its high thermal insulation properties. It is extremely suitable for the production of structural elements with a high level of cavities, such as those used for the construction of beehives, since it is not only thermally and acoustically insulating but is also atmospherically and chemically resistant to acid rain, etc. At the same time, quartz ceramic products are highly resistant against mites and rodents [1].

2. Choice of Forming method on structural parts with a high level of cavities designed for beehives

The most suitable method in this case is slip casting of aqueous suspensions. It is important to note that it is mandatory to ensure that the starting material maintains its high purity during all technological operations [2].

It is known that practically all impurities activate the crystallization of quartz glass. Therefore, the correct selection of both the material of the lining of the grinding unit and the grinding bodies is of great importance. The lining and the grinding bodies are best made of quartz glass, but due to its high wear (up to 10%), it is permissible to use high alumina ceramics with a density above 3.65-3.75 g/cm^2. This leads to a significant reduction of the grinding time (4-5 times), and the observed wear is below 1%, which is essential for the quality of the final product. The use of devices with metal working parts is undesirable.

The slip casting of quartz ceramic parts with cavities results in products with the highest density. This helps to reduce not only the time of the sintering but also its temperature.

An important stage in the technology is the preparation of a suspension of finely ground quartz glass. This is done by coarse and fine wet grinding of the glass in the same grinding unit. Thus, a slip with a minimum amount of water (16÷20%) is obtained [3]. The effectiveness of wet grinding is explained primarily by the fact that water is one of the best surfactants in relation to SiO_2. The adsorptive decrease of strength, the saturation of the unsaturated bonds of the material, the disaggregating action of water, the high specific impact energy of the milling bodies and the reduced soothing action of the suspension are also essential. The wet grinding process is exothermic and the total amount of bound water decreases sharply with the increasing of the temperature. As the temperature increases, the strength of the aqueous layers decreases due to the greater mobility of the ions. Thus the amount of bound water decreases and the free water in the suspension increases.

To create a suspension with low humidity, we use the method of maximum saturation. Its essence is that during wet grinding, the unit is stopped two or three times and ground glass with a sediment composition of 50÷100 microns is added to the suspension in a ratio of about 1/10 of the amount of glass in the suspension. Equilibrium viscosity is reached after 2-3 hours of additional grinding. In this way, the water content of the maximally saturated suspension is reduced by about 4 times. The suspension is quickly sintered, which reduces the shrinkage during drying of the obtained products. The suspension is quickly absorbed on the walls of the mold, as a result of which the shrinkage of the obtained product during drying is minimal. The thickness of the absorbed layer depends on the running time of the process.

The quartz glass particles in the suspension are considered chemical compounds of SiO_2 with ionized silicic acid, continuously dissociating according to equations:

$$\textbf{(1)}\qquad [\boldsymbol{H_4SiO_3}] \rightleftarrows \boldsymbol{SiO_4^{4-}} + \boldsymbol{4H^+}$$

$$\textbf{(2)}\qquad [\boldsymbol{H_2SiO_3}] \rightleftarrows \boldsymbol{SiO_3^{2-}} + \boldsymbol{2H^+}$$

It is assumed that the hydration of SiO_2 is limited by the specific surface area of the particles in the suspension as a result of the building of surface tetrahedra.

The particles of the unstabilized slips are whole aggregates (floccules) with water-filled voids which are preserved during molding. Therefore, a traditional method for stabilizing such slips is gravity stirring. The electric double layer formed by reactions (1) and (2) is insignificant due to the small amount of silicic acid (up to 0.01%) and its low degree of dissociation. The stability of the slip is achieved through a uniform distribution of water dipoles around the ionized solid SiO_2 particles, which is achieved by prolonged stirring (for about 70-80 hours).

The rate of absorption of the suspension on the walls of the mold and the casting density depend significantly on the pH of the suspension. Its optimal value lies in the range from 4.5 to 6. At a pH value of 5 ± 0.3, the silicic acid is most stable, while in a neutral environment it polymerizes intensively, releasing water and reducing the concentration of H^+ ion. HCl is used to lower the pH of the suspension, and NH_4OH to increase it [4].

3. *Molding hollow structural details for beehives from amorphous ceramics*

After preparing a stable suspension of amorphous quartz glass powder, the next stage in the technology involves casting test bodies, carrying out drying and high temperature sintering, and establishing the shrinkage coefficient of the samples. Following this is the making of models and mold outfits for each of the hollow structural details of the ceramic beehive. The residence time of the slip in the mold is determined experimentally and the uncollected slip is drained from the molds.

The time between the filling of the mold with slip and its draining is 12 minutes. The thickness of the cavity wall is 3 cm, and the width of the cavity is 18 mm.

A technological diagram of a workshop for the production of beehives is shown in Fig. 1.

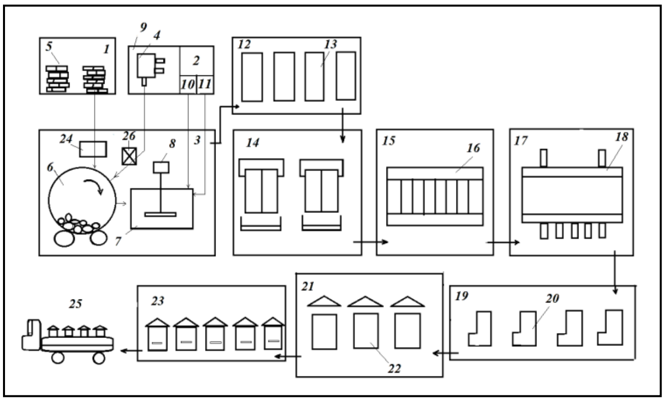

Fig. 1. *Technological diagram of a workshop for the production of beehives*

1. Quartz glass warehouse;
2. Modifier sector;
3. Sector for the preparation of quartz glass suspension with particle size below 100μm;
4. Distiller;
5. Quartz glass with particle size below 100μm;
6. Grinding device;
7. Container for ready-mixed suspension;
8. Stirrer;
9. Distilled water and modifiers sector;
10. Tank for HCl;
11. Tank for NH_4OH;
12. Molding equipment sector;
13. Mold outfits;
14. Molding sector;
15. Sector for drying structural ceramic parts with cavities;
16. Drying sector;
17. Furnace sector;
18. Furnace;
19. Warehouse for finished structural ceramic parts;
20. Sintered structural details for beehives;
21. Ceramic beehive assembly sector;
22. A beehive made of amorphous quartz ceramics
23. Warehouse for finished products;
24. Scales;
25. Dispatch vehicle;
26. Container measuring the volume of the drained fluid (distilled water).

4. *Sintering of amorphous quartz ceramics*

The main factors determining the sintering mode include: the purity of the quartz glass, the density of the cast details, the sedimentary composition of the ground quartz glass and the crystallization tendency.

The quality of the final product is significantly dependent on the heating rate in the temperature range from 1000 ^{0}C to a final temperature of 1200-1300 ^{0}C (in this case 1250 ^{0}C). At slow increase in the temperature (50 - 100 K/h), the crystallization ability also rises, leading to phase formation of high temperature cristobalite, which is a contributing factor to the reduction of the strength of the products. The established optimal heating rate, at which the formation of crystallization centres is avoided, is 400 K/h [5].

The chosen method of obtaining articles from slip ensures a sufficiently high density of the final product. Nevertheless, sintering should not necessarily aim for high density, which is achieved with longer heating and higher temperature, as this leads to an increase in crystallization and sharply reduced strength.

In our case, since the products are not used at high temperatures, a sintering intensifier – 1.2% $B2O_3$ – was added to prevent crystallization.

Fig. 2 shows ceramic structural details with cavities - an intermediate stage of assembling the ceramic beehive, and a completely finished, ready-to-use hive.

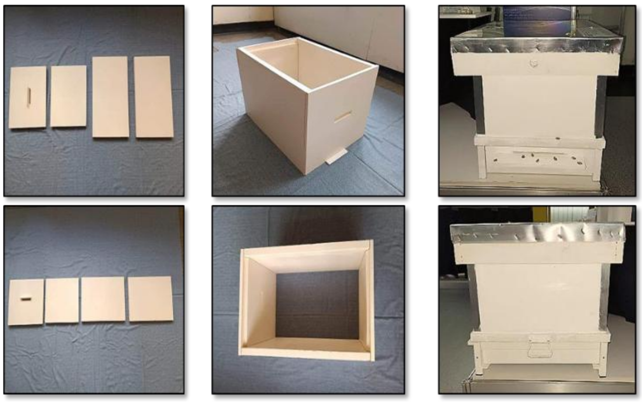

a) ***b)*** ***c)***

Fig. 2. a) *hollow ceramic structural details;* ***b)*** *intermediate stage of assembling a ceramic beehive;* ***c)*** *ceramic hive ready for the settlement of a bee family*

5. *Properties useful for the amorphous quartz ceramics and supporting its use, such as ceramic structural details with high level of cavities designed for beehives*

The mechanical properties are determined by the grain structure and porosity of the suspension absorbed on the walls of the mold. Amorphous quartz ceramic samples with a porosity of 3% had a hardness of about 5.5 Mohs. As the porosity increases to 20%, the hardness drops sharply to about 2 Mohs.

The flexural strength ranges from 3 to 80 MPa. It should be noted that the relationship between porosity and strength typical of other ceramics is not observed in quartz ceramics.

The compressive strength ranges from 50 to 600 MPa depending on the technological parameters, the porosity and the environment in the furnace. It reaches 500 MPa in an air environment and 600 MPa in a vacuum.

It is interesting to note that the value of tensile strength is 75% - 85% of that of flexural strength. This is a very high value, unusual for a ceramic material.

An important indicator for beehives is thermal conductivity. In the case under consideration, it depends both on the structure and the porosity of the material and on the presence of impurities. For opaque materials and for materials with an amorphous structure, such as quartz ceramics, the heat transfer process is determined by the so-called phonon conductive thermal conductivity.

6. *Conclusions:*

1. A technology and a scheme of a workshop for the production of structural details from amorphous quartz ceramics and their assembly into whole beehives have been developed.

2. The factors for obtaining stabilized suspensions of amorphous quartz particles, as well as the conditions for proper high temperature sintering, have been established.

3. A prototype of a beehive has been created, built from structural ceramic details made of amorphous quartz ceramics with a high level of cavities.

7. References

[1] Luben Lakov, Bojidar Jivov, Todorka Lepkova, Krasimira Toncheva, Stancho Yordanov, "Comparison of innovative collapsible ceramic hive and traditional non-separable hives made on the basis of natural plastic raw materials", Machines. Technologies. Materials. Vol. 16, (2022), Issue 10, pg(s) 340-343.
[2] E. Gerasimov and others. under the editorship of Prof. Dr. Eng. S. Bachvarov, "Technology of ceramic products and materials", IC "Sarasfati", Sofia, (2003)
[3] Yu. E. Pivinsky, F. T. Gorobets, "Ogneopory", No. 8, (1968)
[4] G. Solovushkova, Yu. Polonsky, etc., "Ognepory", No. 7, 5÷6, (1980)
[5] Yu. E. Pivinsky, A. G. Romashkin, "Quartz ceramics", Moscow, ed. Literate. in construction, (1972)

Simulation of toolpaths and program verification of a CNC lathe machine tool

Violeta Krcheva[1], Marija Chekerovska[1], Sara Srebrenkoska[1]
[1]Faculty of Mechanical Engineering
'Goce Delcev' University - Stip, Republic of North Macedonia
violeta.krceva@ugd.edu.mk, marija.cekerovska@ugd.edu.mk, sara.srebrenkoska@ugd.edu.mk

Abstract: *This paper presents the simulation and verification of programs created for the CNC Hitachi Seiki Seicos LIII lathe machine tool. The main purpose of program simulation and verification is to ensure the quality and accuracy of the cutting process, which can significantly improve production efficiency. In addition to defining the toolpath, simulation can perform linear and circular interpolation according to specific programs based on G - codes. Therefore, all the motions of the moving parts of the real lathe machine tool can be clearly visualized. The use of simulation is a good solution not only to precise the toolpath, but also verify the program and detect any possible collision between cutting tools and mobile components, before loading the program into the lathe machine tool and starting cutting processes.*

***Keywords**: MANUFACTURING, MACHINING, PROGRAMMING, CODES, SOFTWARE*

1. Introduction

Constant monitoring and control over the dimensions, dimensional tolerances, and surface finish of the designed parts during the manufacturing process provides increased process efficiency and product durability.

Therefore, Computer Numerical Controlled (CNC) machine tools have been widely implemented in the manufacturing industry in the last few years for the reason that their reliability is greater than that of conventional manufacturing machine tools. In order to machine the part in a drawing by using CNC machine tools, it is necessary to generate a series of instructions for activating those CNC machine tools. This task is called CNC programming [1].

CNC programming is a term that refers to the methods for generating the instructions that drive the CNC machine tool [2]. A series of instructions to be performed by the CNC machine tool compose a program of instructions. It consists of G – codes, also known as geometric codes, that control the motion of the machine tool. The standard format for a G – code command begins with "G" and is followed by a two – digit number. These common G – code instructions provide the geometric position of the moving parts of the machine tool, which is generally determined by a coordinate system, as an instrument for identifying the location of the moving parts, moving them in a particular direction, and indicating their precise position in 3D space. This programming language also includes M – codes that control the CNC machine tool or its functions (such as spindle rotation speed, cutting tool feed, cutting tool change, coolant, etc.). M – codes are also written in alphanumeric format, beginning with "M" and two digits following.

G – code, in the act of being a programming language, leads to particular programs of instructions generated by Computer – Aided Manufacturing (CAM) systems that use Computer – Aided Design (CAD) information. These innovative manufacturing systems are used to both design and manufacture products, and they significantly improve the design and productivity of manufacturing processes.

CAD refers to the implementation of computer technology for design and design documentation. On the other side, CAM software programs are used for generating tool paths and verifying program correctness.

The purpose of CAM software programs is to design products and arrange manufacturing processes, particularly CNC machining. Extremely complex parts in large quantities, requiring complex machining processes, are produced on CNC machine tools. Most frequently, final parts and prototypes are machined using CAD/CAM software programs. As a consequence, before being applied to an actual CNC machine tool, these complex manufacturing processes need to be thoroughly verified. For that reason, one of the most well-known, practical, and helpful CAM software programs is the Computer Numeric Control (CNC) Simulator.

The CNC Simulator is an application designed to predict the behavior, performance, and outcome of certain manufacturing processes based on simulation - driven design that has been defined by Sellgren [10] as: "a design process where decisions related to the behaviour and the performance of the design in all major phases of the process are significantly supported by computer – based product modelling and simulation".

Simulation in manufacturing refers to a broad collection of computer based applications to imitate the behavior of manufacturing systems [2]. Numerous simulation software programs have been developed to graphically verify the program of instructions prior to running the part on the machine tool with an actual workpiece. Because of the complexity of generating the program of instruction, simulation software was developed to identify programming errors prior to actual part production. Additionally, it is much easier to edit the program of instruction at this stage of development [3].

The information input to the program regarding the toolpath, tool, material, and parameters specific to each are linked to the geometry. This means that if any of the parameters for the parts mentioned above are changed, the other related data can be regenerated to take these changes into account without recreating the entire operation [4].

2. Research

This research illustrates a simulation of part of the clutch hub manufacturing process. It refers to a machining chip removal process that can be performed on a CNC Hitachi Seiki Seicos LIII lathe machine tool.

Machining is one of the most important manufacturing processes. Machining is a manufacturing process in which a sharp cutting tool is used to cut away material to leave the desired part shape. The predominant cutting action in machining involves shear deformation of the work material to form a chip; as the chip is removed, a new surface is exposed. Machining is most frequently applied to shape metals [8].

Machining with chip removal includes methods in which the design of workpieces is achieved by removing excess of materials [9].

Machining is not just one process; it is a group of processes. There are many kinds of machining operations, each of which is capable of generating a certain part geometry and surface texture The common feature is the use of a cutting tool to form a chip that is removed from the workpart. [8].

In this research, the required machining operations to machine the clutch hub on the mentioned CNC lathe machine tool are discussed. These are: turning, boring, drilling, facing, and chamfering.

In the turning process, the cutting tool is set at a certain depth of cut (mm) and travels to the left with a certain velocity as the workpiece rotates. The feed, or feed rate, is the distance the tool travels horizontally per unit revolution of the workpiece (mm/rev). This movement of the tool produces a chip, which moves up the face of the tool [12].

Turning, boring and drilling generate cylindrical or more complex surfaces of rotation. Facing, also carried out on a lathe, generates a flat surface, normal to the axis of rotation, by feeding the tool from the surface towards the center or outward from the center. [11]

In order to analyze the cutting operations, accurate 2D drawings have been created using a CAD system, i.e., AutoCAD software, for the starting and final workpieces. The starting workpiece is a forged clutch hub (Fig. 1b), and the final part is the machined clutch hub (Fig. 1a).

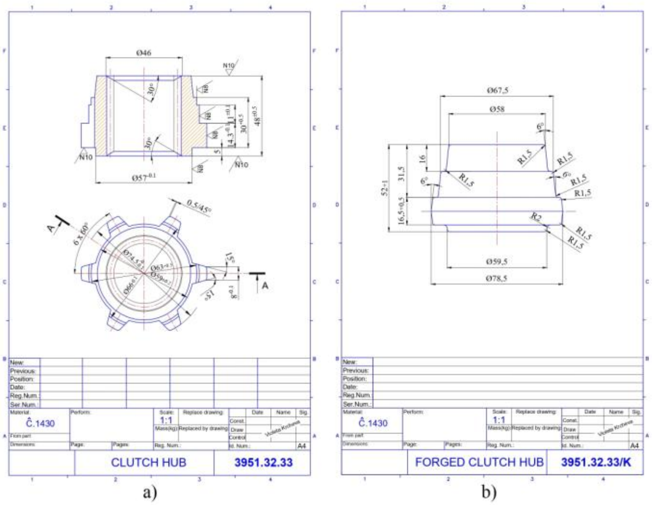

Fig. 1 *(a) Clutch hub, (b) Forged clutch hub*

To precisely define the metal cutting processes performed on this CNC lathe, these drawings are converted into simple 2D models. In that way, the kind of metal cutting operation and final geometry of the part in every phase of the manufacturing process can be clearly explained. Depending on which side of the clutch hub is machined, two phases are determined.

The first phase refers to the shorter side of the forged clutch hub and is defined by four passes.

The first pass (Fig. 2a) is drilling, and the chosen cutting tool is a straight - flute drill DS20 - D3400DM40 – 04 (Fig. 2b) that uses indexable inserts, produced by SANDVIK Coromant.

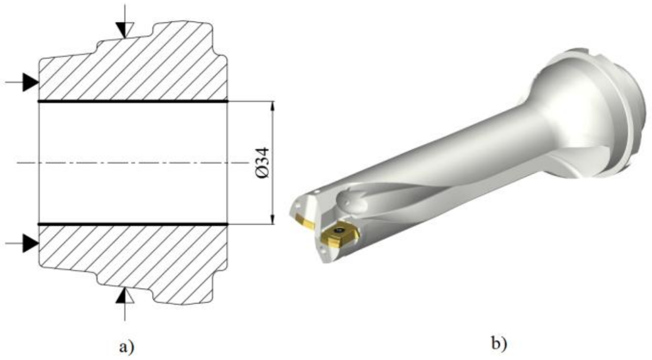

Fig. 2 *(a) First pass, (b) Straight - flute drill that uses indexable inserts*

The second pass (Fig. 3a) is defined by two cutting operations: turning and facing. The chosen cutting tool is a combination of the PCLNR 2525M 12 shank tool (Fig. 3b) and the CNMG 12 04 08-PM 4325 indexable insert (Fig. 3c), both produced by SANDVIK Coromant.

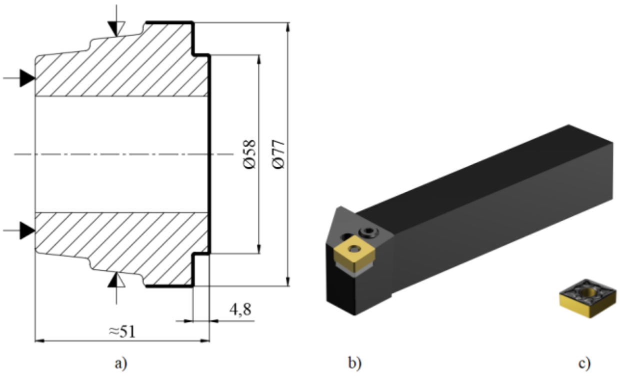

Fig. 3 *(a) Second pass, (b) Shank tool, and (c) Indexable insert*

The third pass (Fig. 4a) is defined by two cutting operations: turning and facing. The chosen cutting tool is a combination of the DDHNL 2525M 15 shank tool (Fig. 4c) and the DNMG 15 06 08-KF 3225 indexable insert (Fig. 4b), both produced by SANDVIK Coromant.

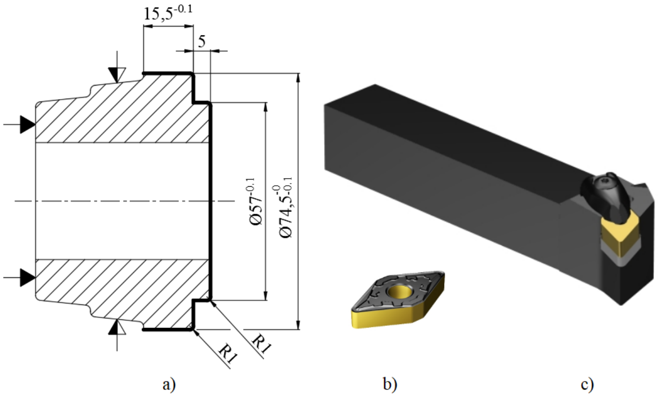

Fig. 4 *(a) Third pass, (b) Indexable insert, and (c) Shank tool*

And the fourth pass (Fig. 5a) is defined just by one cutting operation: chamfering. The chosen cutting tool is a combination of the S25T-PTFNR16 16-W shank tool (Fig. 5b) and the TNMX 16 04 08-WF 1515 indexable insert (Fig. 5c), both produced by SANDVIK Coromant.

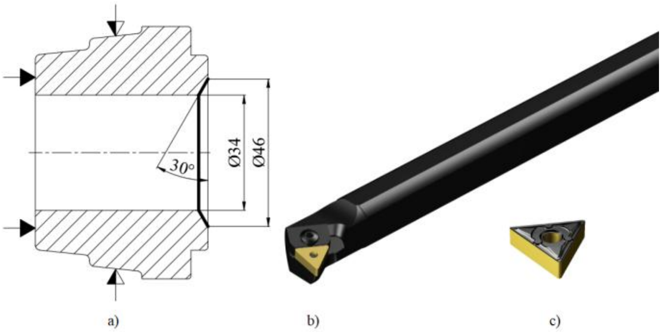

Fig. 5 *(a) Fourth pass, (b) Shank tool, and (c) Indexable insert*

The second phase refers to the longer side of the forged clutch hub and is defined by three passes.

The first pass (Fig. 6a) is defined by two cutting operations: turning and facing, and the chosen cutting tool is the same as in the second pass in the previous phase (Fig. 3b, Fig. 3c).

The second pass (Fig. 6b) is defined by two cutting operations: turning and facing, and the chosen cutting tool is the same as in the third pass in the previous phase (Fig. 4b, Fig. 4c).

And the third pass (Fig. 6c) is defined by two cutting operations: chamfering and boring, and the chosen cutting tool is the same as in the fourth pass in the previous phase (Fig. 5b, Fig. 5c).

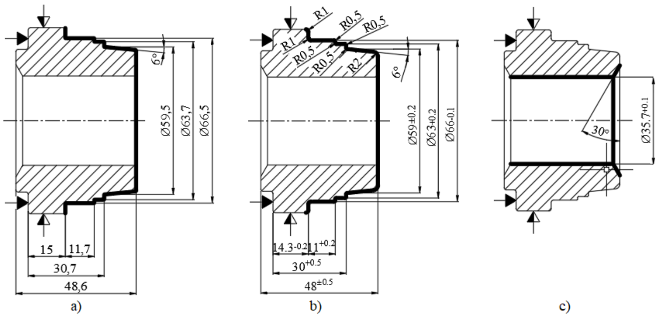

Fig. 6 *(a) First pass, (b) Second pass, and (c) Third pass*

Additionally, for each cutting operation, a program of instructions is created. In that way, two programs of instructions are created, and each one is simulated and verified by the CIMCO Edit v6.1 software program.

.3. *Results and discussion*

Considering the created programs of instructions, in the CIMCO Edit v6.1 software program, the toolpath of the chosen cutting tool is visualized for each of the passes, for every cutting operation. Each block of the program of instructions is provided in a clear manner in accordance with a certain pass (or the complete phase).

The following pictures present a simulation of the toolpath corresponding to the program of instructions created for the mentioned passes and phases, testing and verifying it in the process of design and development.

A linear interpolation movement on the cutting tool using the Z-axis as the direction of movement completes the first pass in the first phase (Fig. 7).

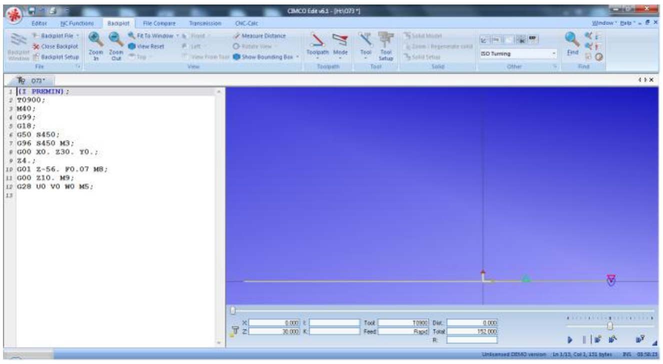

```
(I PREMIN);
T0900;
M40;
G99;
G18;
G50 S450;
G96 S450 M3;
G00 X0. Z30. Y0.;
Z4.;
G01 Z-56. F0.07 M8;
G00 Z10. M9;
G28 U0 V0 W0 M5;
```

Fig. 7 *Simulation of the first pass*

The cutting tool is moved linearly and circularly interpolatively along the X and Z axes to finish the second pass in the first phase (Fig. 8).

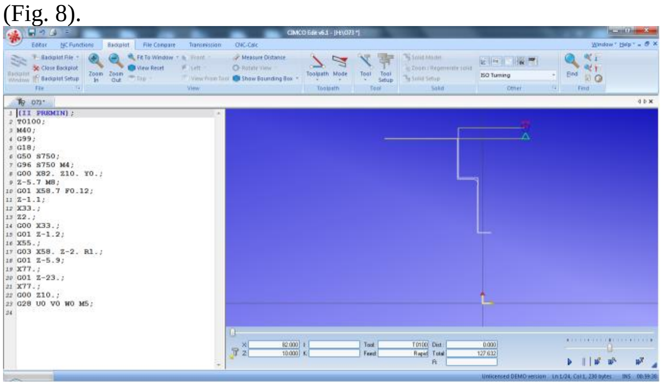

```
(II PREMIN);
T0100;
M40;
G99;
G18;
G50 S750;
G96 S750 M4;
G00 X82. Z10. Y0.;
Z-5.7 M8;
G01 X58.7 F0.12;
Z-1.1;
X33.;
Z2.;
G00 X33.;
G01 Z-1.2;
X55.;
G03 X58. Z-2. R1.;
G01 Z-5.9;
X77.;
G01 Z-23.;
X77.;
G00 Z10.;
G28 U0 V0 W0 M5;
```

Fig. 8 *Simulation of the second pass*

Linear and circular interpolation motions on the cutting tool oriented on the X and Z axes complete the third pass in the first phase (Fig. 9).

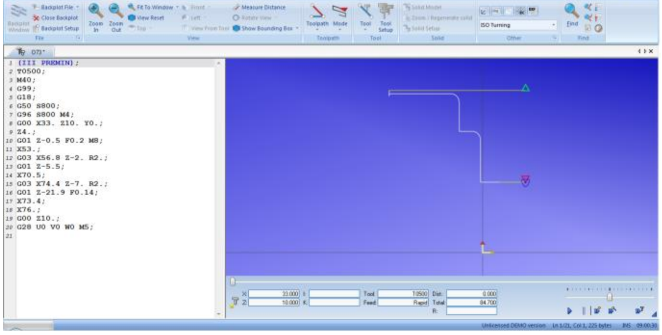

```
(III PREMIN);
T0500;
M40;
G99;
G18;
G50 S800;
G96 S800 M4;
G00 X33. Z10. Y0.;
Z4.;
G01 Z-0.5 F0.2 M8;
X53.;
G03 X56.8 Z-2. R2.;
G01 Z-5.5;
X70.5;
G03 X74.4 Z-7. R2.;
G01 Z-21.9 F0.14;
X73.4;
X76.;
G00 Z10.;
G28 U0 V0 W0 M5;
```

Fig. 9 *Simulation of the third pass*

The fourth pass in the first phase is finished with linear movements of the cutting tool pointed in the X and Z axes (Fig. 10).

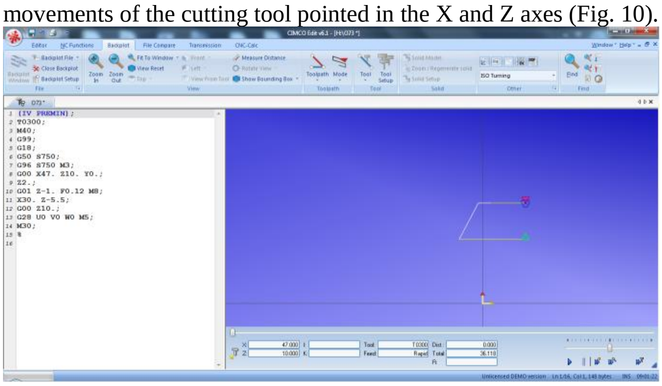

```
(IV PREMIN);
T0300;
M40;
G99;
G18;
G50 S750;
G96 S750 M3;
G00 X47. Z10. Y0.;
Z2.;
G01 Z-1. F0.12 M8;
X30. Z-5.5;
G00 Z10.;
G28 U0 V0 W0 M5;
M30;
%
```

Fig. 10 *Simulation of the fourth pass*

Completing the four passes results in the realization of the first phase (Fig. 11).

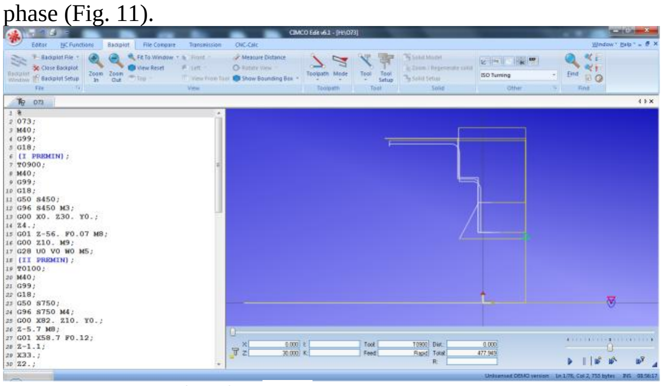

```
%
O73;
M40;
G99;
G18;
(I PREMIN);
T0900;
M40;
G99;
G18;
G50 S450;
G96 S450 M3;
G00 X0. Z30. Y0.;
Z4.;
G01 Z-56. F0.07 M8;
G00 Z10. M9;
G28 U0 V0 W0 M5;
(II PREMIN);
T0100;
M40;
G99;
G18;
G50 S750;
G96 S750 M4;
G00 X82. Z10. Y0.;
Z-5.7 M8;
G01 X58.7 F0.12;
Z-1.1;
X33.;
Z2.;
```

Fig. 11 *Simulation of the first phase*

To complete the first pass in the second phase, the cutting tool is moved along the X and Z axes in a linear and circular interpolative motion (Fig. 12).

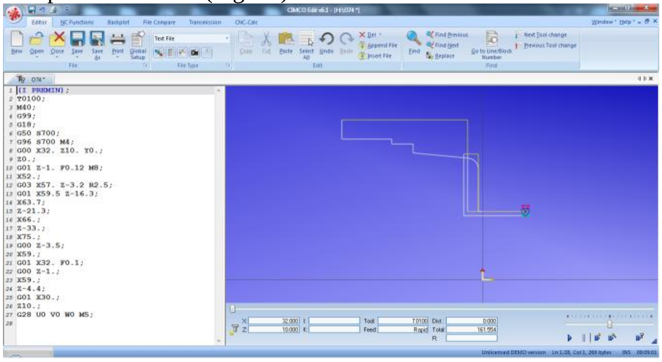

```
(I PREMIN);
T0100;
M40;
G99;
G18;
G50 S700;
G96 S700 M4;
G00 X32. Z10. Y0.;
Z0.;
G01 Z-1. F0.12 M8;
X52.;
G03 X57. Z-3.2 R2.5;
G01 X59.5 Z-16.3;
X63.7;
Z-21.3;
X66.;
Z-33.;
X75.;
G00 Z-3.5;
X59.;
G01 X32. F0.1;
G00 Z-1.;
X59.;
Z-4.4;
G01 X30.;
Z10.;
G28 U0 V0 W0 M5;
```

Fig. 12 *Simulation of the first pass*

The second pass in the second phase is finished with linear and circular interpolation motions on the cutting tool oriented on the X and Z axes (Fig. 13).

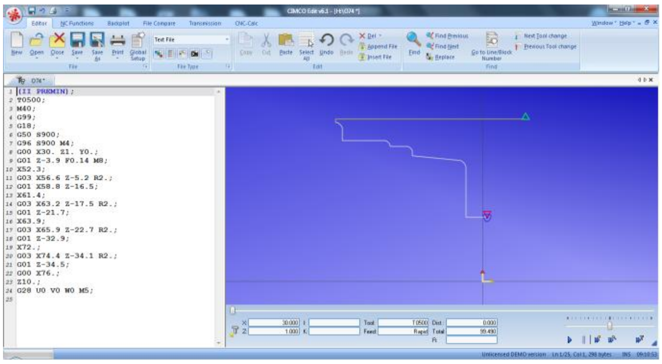

```
(II PREMIN);
T0500;
M40;
G99;
G18;
G50 S900;
G96 S900 M4;
G00 X30. Z1. Y0.;
G01 Z-3.9 F0.14 M8;
X52.3;
G03 X56.6 Z-5.2 R2.;
G01 X58.8 Z-16.5;
X61.4;
G03 X63.2 Z-17.5 R2.;
G01 Z-21.7;
X63.9;
G03 X65.9 Z-22.7 R2.;
G01 Z-32.9;
X72.;
G03 X74.4 Z-34.1 R2.;
G01 Z-34.5;
G00 X76.;
Z10.;
G28 U0 V0 W0 M5;
```

__Fig. 13__ Simulation of the second pass

The cutting tool is moved in a linear interpolative motion along the X and Z axes to finish the third pass in the second phase (Fig. 14).

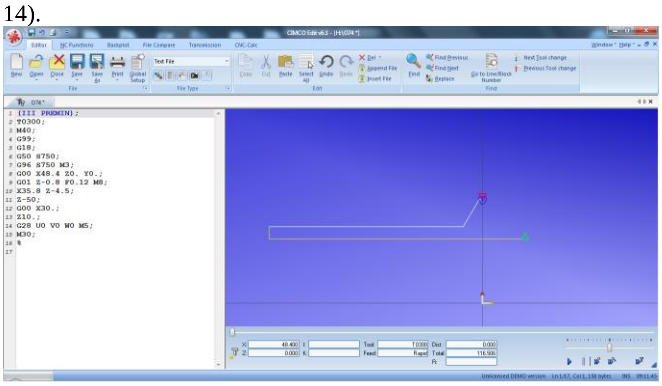

```
(III PREMIN);
T0300;
M40;
G99;
G18;
G50 S750;
G96 S750 M3;
G00 X48.4 Z0. Y0.;
G01 Z-0.8 F0.12 M8;
X35.8 Z-4.5;
Z-50;
G00 X30.;
Z10.;
G28 U0 V0 W0 M5;
M30;
%
```

__Fig. 14__ Simulation of the third pass

The realization of the second phase follows the completion of the three passes (Fig. 15).

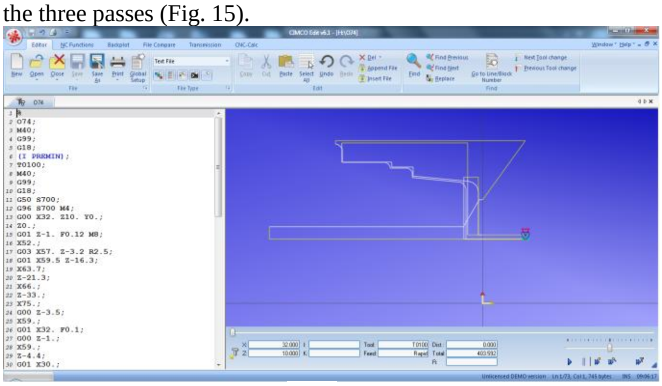

```
%
O74;
M40;
G99;
G18;
(I PREMIN);
T0100;
M40;
G99;
G18;
G50 S700;
G96 S700 M4;
G00 X32. Z10. Y0.;
Z0.;
G01 Z-1. F0.12 M8;
X52.;
G03 X57. Z-3.2 R2.5;
G01 X59.5 Z-16.3;
X63.7;
Z-21.3;
X66.;
Z-33.;
X75.;
G00 Z-3.5;
X59.;
G01 X32. F0.1;
G00 Z-1.;
X59.;
Z-4.4;
G01 X30.;
```

__Fig. 15__ Simulation of the second phase

4. Conclusion

In order to develop parts from design to end product with acceptable accuracy, compatibility, machinability, and processability on a CNC machine tool, certain steps must be followed. According to the reliable manufacturing method, the target workpiece is first constructed using particular design software. Then, a specific program of instructions based on G-code is created.

After receiving the program of instructions in the CIMCO Edit v6.1 software program, simulations of the toolpath are generated. Actually, the program of instructions is tested and visualized in the interest of its verification before being applied to the CNC lathe machine tool. Through simulation and verification of the program of instructions, every possible collision is predicted, detected, and eliminated.

The benefit of current and future usage and development of this type of software is that they can rapidly examine various manufacturing strategies without causing any disturbance, damage, or waste. In addition, they are convenient for continuous analysis of the manufacturing processes in order to optimize machining operations, reducing cost and time while raising quality and conserving materials.

5. References

[1] S. Suh, S. Kang, D. Chung, I. Stroud, *Theory and Design of CNC Systems* (Springer - Verlag, London, 2008), pp.278

[2] P. Radhakrishnan, S. Subramanyan, V. Raju, *CAD/CAM/CIM*, 3th ed., (New Age International Publishers, New Delhi, 2008), pp. 403

[3] D. E. Kandray, *Programmable Automation Technologies: An Introduction to CNC, Robotics ans PLCs* (Industrial Press, United States of America, 2010), pp.120

[4] K. Evans, *Programming of CNC Machines*, 4th ed., (Industrial Press, United States of America, 2016), pp. 311

[5] P.R.Nair, H. Khokhawat, R.G. Chittawadigi, Int. Con. Ro. S. Ma. 133, 823-830 (2018)

[6] S. Zivanovic, N. Slavkovic, Z. Dimic, G. Vasilic, R. Puzovic, D. Milutinovic, 6th ICMEN, 41-51 (2017)

[7] L. N. B. Misman, (2017). Application Of Cnc Simulator For CNC Machining Via CAD/CAM [dissertation], 35.

[8] M. P. Groover, *Fundamentals of Modern Manufacturing: Materials, Processes, and Systems*, 4th ed., (John Wiley & Sons, United States of America, 2010), pp.483-485

[9] G. Globocki Lakić, D. Kramar, J. Kopać, *Metal Cutting: Theory and Applications* (University of Ljubljana, Ljubljana, 2014), pp. 6

[10] U. Sellgren, *Simulation-driven design: motives, means, and opportunities*, [Doctoral thesis], 1999

[11] E. Trent, P. Wright, *Metal Cutting*, 4th ed., (Butterworth–Heinemann, United States of America, 2000), pp. 32

[12] S. Kalpakjian, S. R. Schmid, *Manufacturing Engineering and Technology*, 6th ed., (Prentice Hall, United States of America, 2009), pp.575

[13] D. M. Yip-Hoi, 120th ASSE Ann. Co. Expo. 6201, 23.1336-1 – 15 (2013)

[14] H. Yau, J. Chen, B. Yu, T. Yang, Int. Con. Sim. Mod. Methodol., 717-724 (2014)

[15] S. Zivanovic, N. Slavkovic, B. Kokotovic, D. Milutinovic, Int. J. Eng, 1854, 189 – 194 (2017).

Analyze of welding arc parameters in shielded metal arc welding

Yordan Denev[1]
Technical University of Varna[1]
e-mail: y.denev@tu-varna.bg

Abstract: *Shielded metal arc welding is widely used in heavy industries in partly shipbuilding and ship repair. This method didn't required special personal skills and equipment. Different scientists are analyzed welding parameters, mechanical characteristics and chemical composition in welding seam but interesting is to be investigated welding arc characteristics in different electrodes. The paper deal with analyze of welding arc parameters in shielded metal arc welding. For this purpose on mild steel plates are welded seams with different diameters of electrodes and different welding current. In welding process are measured welding arc burning time, length of electrodes melted part, welding machine voltage and weight of melted electrodes part. For analyze welding arc parameters are used response surface methodology method (RSM). Used RSM in the paper is 2^k factorial design where k=2 factors. The influence of each to other factors of welding arc is presented by meta models.*

KEYWORDS: *SHIELDED WELDING, ARC LENGHT, MODELS, EXPERIMENT PLANING*

1. Introduction.

Welding arc is main component of welding seams. Its role is to transfer melted metal in weld seam. Transfer of melted metal from electrodes to weld pool depends from electrodynamics forces, gravity, welding arc pressure and gases in welding arc. The type of melted metal transfer is large dropped, middle dropped or like a stream.

Welding arc analyzation is widely area of scientists. Characterization of welding arc and weld pool formation in vacuum gas hollow tungsten arc welding is analyzed in [1]. In this paper authors obtain the effective arc radii for various welding conditions in vacuum gas hollow tungsten arc welding. They used Abel inversion algorithm to CCD arc image and determine the distribution of arc heat flux, arc pressure and current density from the physical relations of arc irradiance, temperature and current density in gas tungsten arc welding.

Physical characteristics of arc ignition process are analyzed in[4]. In their publication they focused attention on stable combustion state and the research on the mechanism of welding arc ignition process is quite lack. They used tungsten arc welding process for their analysis and physically characteristic of welding arc are investigated by camera with height resolution. The welding arc electron density during the period of the arc ignition is calculated by the Stark-broadened lines of Hα.

In[3] is studied effect of arc length on oxygen content and mechanical properties of weld metal in pulsed gas metal arc welding. For the analyze the authors used Q 690 high strength steel and ER69-G wire with diameter 1,2mm. Shielded gas used for experimental procedure is 82%Ar and 18% CO_2. Conclusion is that arc length raised, oxidation in drop transfer and oxygen content in weld metal increased significantly.

Determination of welding parameters is important stage from welding process. Proper parameters selection resulting to minimization of deformation. This process is widely described in[5]. They describe step by step stages in parameters determine. This information is useful for production of welded construction in heavy industry, shipbuilding and ship repair sector.

There aren't enough information, data and analyses about welding arc in shielded metal arc welding process and mainly about its parameters. The main parameters of welding arc are burning time, burning stability and weight melted metal. Burning stability of welding arc method is developed by akad. Hrenov. It is consist of burned of arc of rigid electrode. The arc burn while length of electrode is enough to touch the steel plates.

2. Description of shielded metal arc welding process.

Shielded metal arc welding is most applicable method in industry. It is characterized with simplicity in equipment and not so special skills of operator. The main method equipment is shown on fig.1.

Welding arc is the distance form electrodes to surface where arc is formed. Based on this welding arc can be divided into three types:

- Medium or normal;
- Long;
- Short;

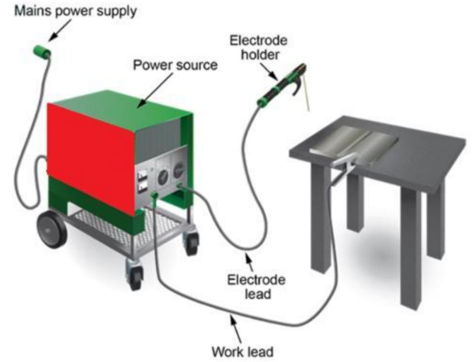

Fig.1. *Shielded metal arc welding scheme[8]*

Power source is direct or alternative current. This power sources has static dropping V-A characteristic. Welding arc temperature in this power sources is about 6000-9000°C.

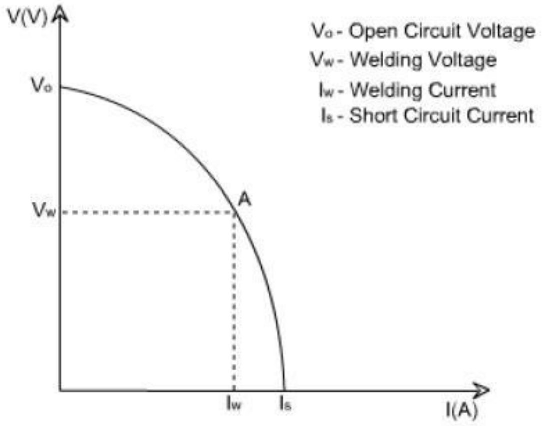

Fig.2.*V-A characteristic of power source[9]*

Welding arc can be divided into three regions: anode, cathode and arc column. On fig.3. is shown welding arc structure and voltage distribution.

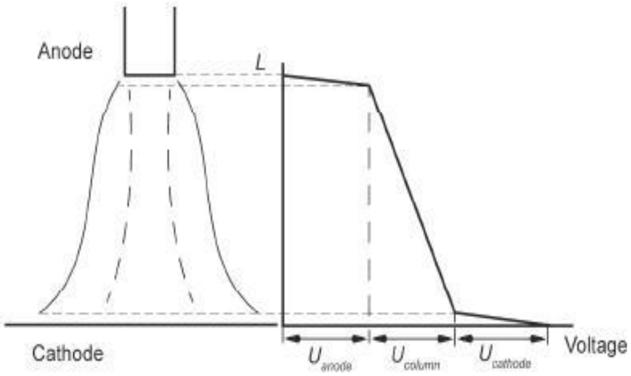

Fig.3. *Voltage arc distribution[6]*

At the anode region, as the temperature falls higher voltage is required to maintain ionization in the arc. The heat loss is compensated by electrons in the plasma. In cathode area is the same situation with the difference that more heat is generated in anode area than in cathode. In the arc column, high temperature concentrations are accumulated. This process together with ionized metals kept welding arc burning at temperatures of about 6000K.

Electrodes for shielded metal arc welding are covered electrodes. The role of a cover is to protect welding seams from atmospheric . The cover contains stabilizing, shielding, fluxing, deoxidizing and other elements supporting the welding process. Depending on the type of electrode being used, the electrode covering provides the welding seam in air[7].In proper selection of cored electrodes is important to be considered followed rules:

- R_m electrodes≈R_m base metal
- Chemical composition electrodes≈ Chemical composition base metal

If these rules are considered working characteristic of welding construction is absolutely reliable.

According[2] shielded metal arc welding cored electrodes are with diameter range 2.00, 2.5, 3.0,3.25,4.0,5.0,6.0mm and length from 350mm and 450mm.

The value of welding current depends form electrodes diameter. It is calculated by following formulae:

$$Iweld = de * k \qquad (1)$$

where: de- diameter of electrode, k- coefficient depended from steel grade, k=40 for low carbon, low alloyed steels, k=30 for other carbon steels.

Shielded metal arc welding method is used in different welding positions. This gave it widely application in industry, shipbuilding and ship repairing.

3. Experimental procedure.

The experimental procedure is consisting of welding seams on the mild steels plate St 235. Welding is done by rutile electrodes with different diameter and different values of welding current.

Table 1. *Welding current for different electrodes diameters*

№	De, mm	I weld, A
1	3.25	80
2	2.5	100
3	3.25	120
4	4.00	150

For purpose achieving in the paper is used welding machine for shielded metal arc welding shown of fig.4.

In selection of electrodes rules for equal or approximate chemical composition and mechanical characteristic of electrodes and base metal are kept. Chemical composition of steel plates are shown on table 2 and chemical composition of electrodes are shown on table 3.

Table 2*. Chemical composition of steel plates base metal*

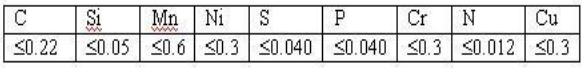

C	Si	Mn	Ni	S	P	Cr	N	Cu
≤0.22	≤0.05	≤0.6	≤0.3	≤0.040	≤0.040	≤0.3	≤0.012	≤0.3

Table 3. Chemical composition of electrodes

C, %	Si, %	Mn, %
0.08	0.3	0.4

Fig.4. *Overview of welding machine*

Mechanical characteristic of steel plates and electrodes are shown on table 4 and table 5.

Table 4. *Mechanical characteristic of base metal*

Rm, MPa	Rpl, MPa	A, %
470	340	26

Table 5. *Mechanical characteristic of electrodes*

Rm, MPa	Rpl, MPa	A,%
510	400	28

In welding process are measured parameters of welding arc: welding arc burning time, length of electrodes, melted part, welding machine voltage.

To analyze influence of parameters on each other are used response surface methodology. The commonly used response surface methodology is the simplest 2k factor design. In this 2k factor design, every factor has two levels(+1, -1) and each run at two levels. The levels of the factors can be called,, low" and,, high". The two levels can be quantitative and qualitative. In engineering analysis, for example, quantitative factors are forces, pressure, speed and etc. and qualitative factors can be number of machines, ships and other. To convert factorial design into regression models, we used some of the following models:

- First model

$$y = \beta_0 + \beta_1 x_1 + \beta_2 x_2 + ...\beta_k x_k \qquad (2)$$

- Iteraction model

$$y = \beta_0 + \sum_{i=1}^{k} \beta_i x_i + \sum \sum_{i<j}^{k} \beta_{ij} x_i x_j \qquad (3)$$

- Second model

$$y = \beta_0 + \sum_{i=1}^{k} \beta_i x_i + \sum \sum_{i<j}^{k} \beta_{ij} x_i x_j + \sum_{i=1}^{k} \beta_{ij} x_i^2 \qquad (4)$$

where: x_1 is the coded variable that represent the reactant concentration, x_2 is the coded variable that represent the feed rate, β-s are correlation coefficients.

Design matrix of 2^2 factor planning is shown on table 6.

***Table 6.** Design matrix*

№	X1	X2
1	-1	-1
2	+1	-1
3	-1	+1
4	+1	+1

4. Results

Experimental results are processed by software STATISTICA and Excel worksheet. To analyzed impact of welding arc parameters is used first regression model of RSM. Widely matrix of experimental plan matrix is shown in table and the actual matrix of plan matrix is shown in table 7.

***Table 7.** Full design matrix*

№	X1	X2	X3	X4
1	1	-1	-1	1
2	1	1	-1	-1
3	1	-1	1	-1
4	1	1	1	1

Time for welding arc burning time and length of welding arc are objects of analysis. These two parameters describe and characterize the welding arc. Based on the model are done graph dependence of:

Length of welding arc against diameter of electrode and welding current fig. 5.

Welding arc burning time against voltage of welding machine and welding current, fig.6.

***Table 8.** Experimental data*

№	Voltage, V	L weld arc, mm	de, mm	I weld, A	T weld arc, sec
1	14	24	2.0	80	30.3
2	17	27	2.5	100	44.45
3	21	30	3.25	120	67.7
4	26	34	4.0	150	79.5

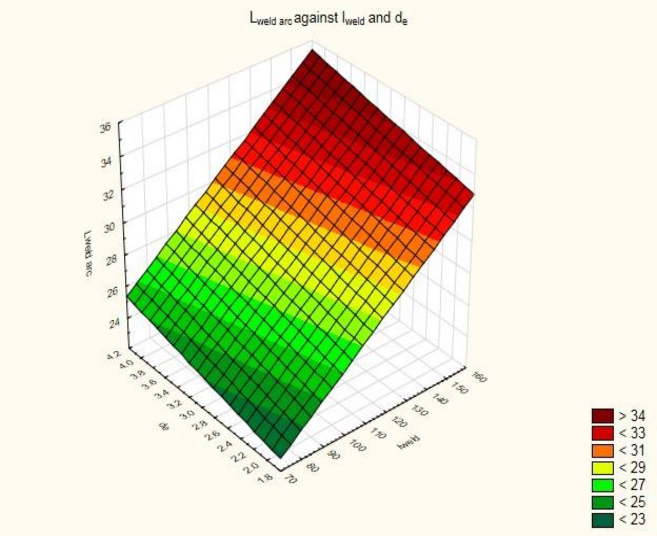

***Fig.5.** Length of welding arc against diameter of electrodes and welding current*

1. Conclusion

In the paper are analyzed welding arc parameters in manual shielded metal arc welding. For experimental procedure are used retile electrodes with diameters of 2.00; 2.5; 3.25 and 4.00mm and steel plates grade ST235.

To analyze the results are used response surface methodology. Two-level factorial design of experiments is used. Based on methodology regression models, regression equations for analyzed welding arc parameters were developed.

Length of welding arc closely depends form welding current. With higher welding current values, the length of the welding arc is higher. Type and diameter of electrodes haven't a so important impact on length of welding arc. This is confirmed by the developed regression equation.

Time for welding arc burning closely depends on voltage of welding machine. Impact degree of welding current in burning time is not so clearly expressed. In higher values of welding machine voltages burning time is bigger. This is in close relation to welding current.

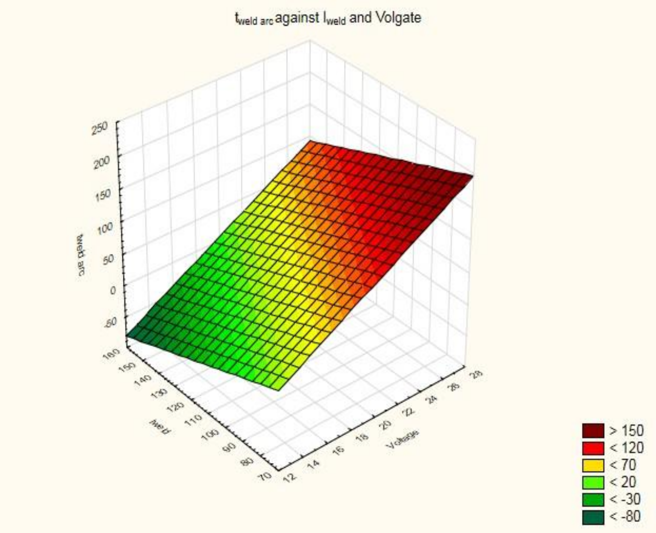

***Fig.6.** Welding arc burning time against voltage and welding current*

$$t_{weldarc} = -25.5333 + 10.8306V - 1.1567 I_{weld} \qquad (5)$$

$$L_{weldarc} = 13.0385 + 0.1115V + 1.0769 I_{weld} \qquad (6)$$

2. Declarations

Conflict of interests: The author has no conflicts of interest to declare that are relevant to the content of this article.

3. Bibliography

[1] Cho, D.W., Lee, S.H., Na, S.J., 2013, Characterization of welding arc and weld pool formation in vacuum gas hollow tungsten arc welding, Journal of Materials Processing Technology, ELSIVIER, pp. 143-152;

[2] ESAB, catalogue;

[3] Jiache, Xu, Xiaoxiao Zhou, Dawei Zhu, 2022, Effect of Arc Length on Oxygen Content and Mechanical Properties of Weld Metal during Pulsed GMAW, 12,176, Basel, Switzerland;

[4] Shi, L., Song, Y., Xiao, T., Ran, G., 2012, Physical Characteristics of Welding Arc Ignition Process, CHINESE JOURNAL OF MECHANICAL ENGINEERING Vol. 25, No. 4, pp. 786-791;

[5] Ugur Soy, Osman Lyibilgin, Fehim Findak, Cemiz Oz, Yasar Kiyan, 2011, Determination of welding parameters for shielded metal arc welding, Scientific Research and Essays Vol. 6(15), pp. 3153-3160, DOI: 10.5897/SRE10.1073;

[6] Weman, K., 2012, Welding process handbook, second edition, Woodhead Publishing Limited, Cambridge, UK

[7] https://www.fabtechexpo.com/blog/2018/01/04/shielded-metal-arc-welding-basics;

[8] https://www.materialwelding.com/what-is-shielded-metal-arc-welding-smaw/;

[9] https://weldknowledge.com/2016/02/06/characteristics-of-arc-welding-power-sources/;

Physico-chemical characterization of the corn silk by DTA-TGA, SEM-EDS and FTIR analysis

Milan Gorgievski [1*], Dragana Božić [2], Miljan Marković [1], Nada Štrbac [1], Vesna Grekulović [1], Kristina Božinović [1], Milica Zdravković [1]
University of Belgrade Technical Faculty in Bor, Vojske Jugoslavije 12, 19210 Bor, Serbia[1]
Mining and Metallurgy Institute Bor, Zeleni bulevar 35, 19210 Bor, Serbia[2]
mgorgievski@tfbor.bg.ac.rs

Abstract: *In this paper, the results of the DTA-TGA, SEM-EDS, and FTIR analysis of the corn silk are presented. The DTA-TGA analysis shows that the decomposition of corn silk has several stages which are manifested with corresponding peaks on obtained DTA-TGA curves. SEM-EDS analysis was performed before and after the adsorption of copper ions. It has shown that untreated corn silk has a non-uniform structure, consisting of channels and cavities of irregular orientation, which facilitates the penetration of the water phase into the adsorbent structure, and incorporation of copper ions in the internal active sites. After the adsorption of Cu^{2+} ions, the structure becomes more compact, and uniform, as a result of the incorporation of copper ions into the molecular structure of the corn silk. FTIR analysis shows that ion exchange is not the dominant mechanism of binding copper ions to the active sites in the molecular structure of the corn silk, but also chemisorption and physical adsorption is present.*

***Keywords**: CORN SILK, CHARACTERIZATION, DTA-TGA, SEM-EDS, FTIR, COPPER IONS*

1. Introduction

Water pollution with heavy metals is a significant environmental problem all over the world. Most of these pollutants are not biodegradable and tend to accumulate in living organisms. Their toxicity, along with their non-biodegradability makes the polluted wastewater purification an initial concern [1].

Conventional methods for wastewater purification include ion exchange, chemical precipitation, membrane processes, electrolysis, etc [1, 2]. Among these wastewater treatment methods, sorption has shown good prospects, thanks to its economic feasibility, and environmental-friendly nature [2].

The use of waste biomass, including agricultural by-products, as adsorbents for wastewater purification, has been very popular in the scientific world in the past decade. This process is often referred to as biosorption. The main advantages of the biosorption process are the low-cost, biodegradability, efficiency, ease of operation and simplicity of design, and abundance of potential biosorbents. Further, this process can remove/minimize the different types of pollutants, and thus it has wider applicability in water pollution control [2, 3].

Corn silk (*Stigma maydis*) has been used for thousands of years as a folk medicine in many parts of the world for the treatment of edema as well as for cystitis, gout, kidney stones, nephritis, diabetes mellitus, and prostatitis [4].

Corn silk is a by-product of corn after deep processing, and is one kind of crop waste, widely available in large quantities. Corn silk, whose components are significantly different from maize stalk, maize corncob, and maize leaf, mainly contains cellulose. However, corn silk is constituted of lignin and cellulose and there are a large number of oxygen-containing functional groups, such as hydroxyl groups, carboxyl, and carbonyl on its surface classifying it as a potential adsorbent for metal ions [1, 5]. However, there are only a few papers dealing with metal removal by raw or modified corn silk [1, 6].

In this study, SEM-EDS, DTA-TGA, and FTIR analysis of corn silk, as a potential adsorbent for copper ions biosorption is given. The SEM-EDS and FTIR analysis was performed on samples before and after the biosorption process.

2. Materials and methods

Corn silk was collected from the local cornfields near the city of Bor (Serbia). Collected samples were firstly washed, ground, then sieved through a set of laboratory sieves, and the sieve fraction (−1 + 0.4) mm was analyzed for potential use as an adsorbent for copper ions biosorption.

A synthetic Cu^{2+} solution of an initial concentration of 0.2 g dm^{-3} was used for the adsorption experiments, to obtain a corn silk sample after the biosorption process for the SEM-EDS and FTIR analysis.

The SEM-EDS analysis was performed on a VEGA 3 LMU TESCAN scanning electron microscope, coupled with an integrated energy-dispersive X-ray detector X-act SDD 10 mm^2 (Oxford Instruments).

The DTA-TGA analysis was performed on a simultaneous DSC-DTA-TGA device (SDT-Q600), under an inert atmosphere (nitrogen).

The FTIR analysis of the corn silk samples before and after the biosorption process was performed on a BOMEM MB-100 (Hartman & Braun Michelson) FTIR spectrometer.

3. Results and discussion

3.1 SEM-EDS analysis of corn silk

Based on a large number of results from scientific research in which the SEM analysis of different biosorbents was performed, the corn silk was analysed before and after the biosorption process. On the basis of the SEM analysis, in which the surface of the samples was observed, certain differences in the structure of the surface before and after the biosorption process were noted. The surface morphology of the corn silk samples before and after the biosorption process is shown in Figure 1.

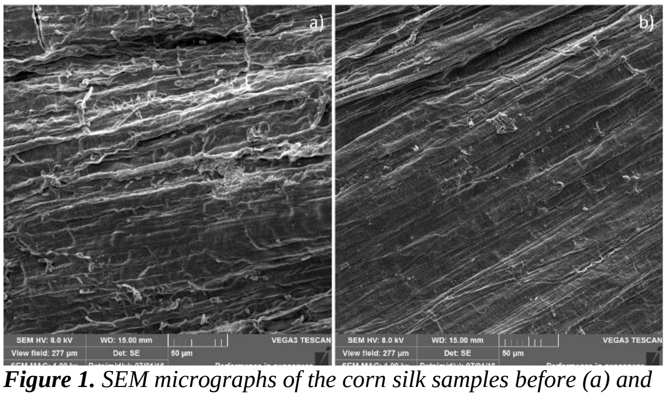

***Figure 1.** SEM micrographs of the corn silk samples before (a) and after the biosorption of copper ions (b)*

Figure 1a shows a micrograph of the surface of untreated corn silk. Macro-pores and cavities can be seen in the image. The presence of macro pores and larger cavities facilitate the movement of the aqueous phase through the corn silk structure and promotes internal diffusion. The cavities and macro-pores of untreated corn silk have a chaotic and irregular orientation, and their openings are also irregularly shaped, as can be seen in Figure 1a. It is assumed that metal ions through these pores easily penetrate into the structure of the adsorbent where they are adsorbed on numerous internal active sites [6]. Similar morphological changes in biosorbents were observed by other authors using SEM analysis in their works [7, 8].

After the biosorption process, a change in the morphology of the surface is noted (Figure 1b), compared to the untreated sample. Figure 1b shows a relatively uniform structure of the corn silk sample. The change in morphology is manifested as a compact cellulosic structure, where no pores are observed, and the surface has become rough [9]. The given changes in the morphology of the sample lead to the conclusion that the adsorption of copper ions is related to chemical changes on the surface of corn silk.

The EDS spectra of corn silk samples before and after the biosorption process are shown in Figure 2. As can be seen from Figure 2a, pointed on the alkali and alkali earth metal ions, the EDS spectrum before the biosorption of copper ions shows a high content of Ca, K, and Mg. After the biosorption process, the K peaks decreased with the disappearance of Ca and Mg peaks, and peaks for Cu were observed (Figure 2b). Hence, it could be assumed that the ion-exchange mechanism occurs between Ca^{2+}, Mg^{2+}, K^+, and Cu^{2+} ions [10].

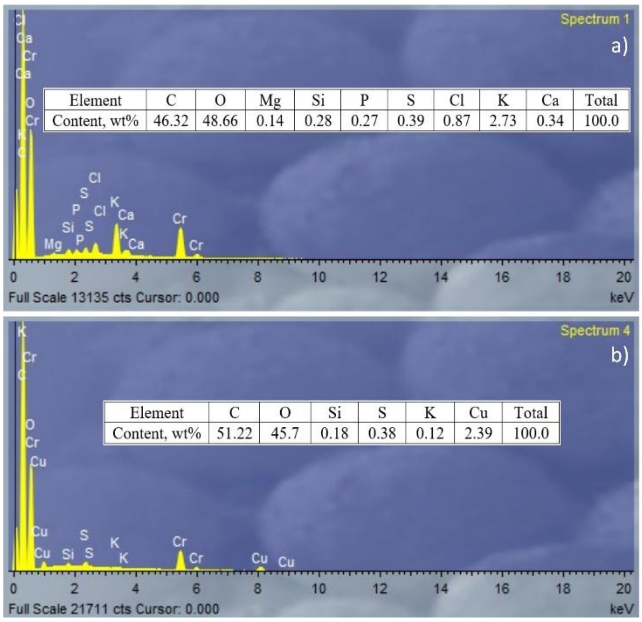

Element	C	O	Mg	Si	P	S	Cl	K	Ca	Total
Content, wt%	46.32	48.66	0.14	0.28	0.27	0.39	0.87	2.73	0.34	100.0

Element	C	O	Si	S	K	Cu	Total
Content, wt%	51.22	45.7	0.18	0.38	0.12	2.39	100.0

Figure 2. *The EDS analysis of the corn silk samples before (a) and after the biosorption of copper ions (b)*

3.2 DTA-TGA analysis of corn silk

The DTA-TGA analysis of corn silk was performed in order to determine the thermal stability of the biosorbent. 4 mg of corn silk was heated at a constant rate of 10 °C/min in the range from 20 °C to 900 °C, and the obtained results are shown in Figure 3.

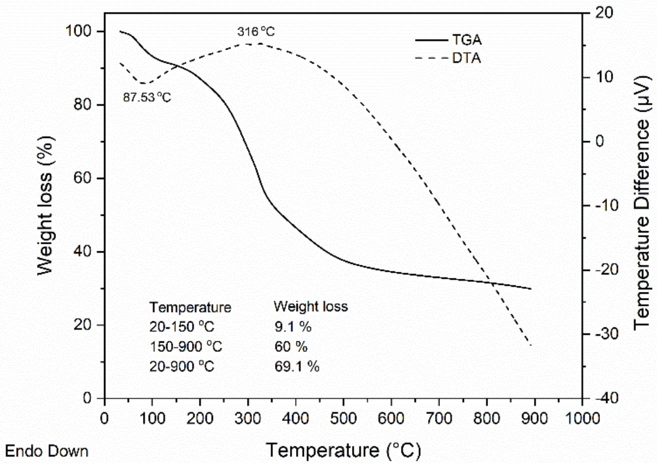

Figure 3. *The DTA-TGA analysis of the corn silk sample*

Figure 3 shows the DTA and TGA profiles of corn silk. The TGA curve shows a weight loss of 9.1 % in the temperature range from 20 to 150 °C, as a result of the loss of physically bound water within the sample. This process is followed by an exothermic peak on the DTA curve with a minimum of 87.53 °C. Further, in the range from 150 to 900 °C, the TGA curve shows a weight loss of about 60 %, which can be contributed to the degradation of the lignocellulose components present in the corn silk sample, and the formation of volatile products like CO, CO_2 and others [10, 11]. This change is followed by an exothermic peak on the DTA curve, with a maximum of 316 °C. The total weight loss, in the temperature range from 20 to 900 °C, was 69.1 %.

3.3 FTIR analysis of corn silk

FTIR spectroscopy is an instrumental method used to determine the functional groups in the adsorbent responsible for ion exchange with metal ions from the solution. The FTIR analysis of the corn silk samples was performed in the spectral range from 4000-400 cm^{-1}, with a resolution of 2 cm^{-1}. The obtained results are shown in Figure 4.

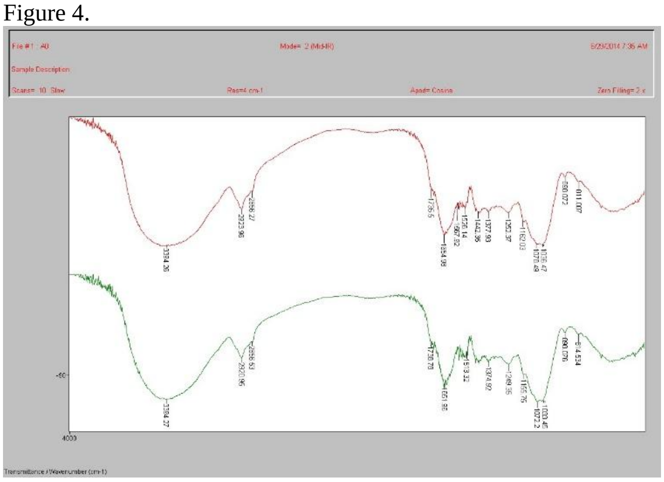

Figure 4. *FTIR spectra of the corn silk samples before (green band) and after the biosorption of copper ions (red band)*

The obtained FTIR spectra before and after the biosorption process do not show significant shifts in the terms of wavelengths, which suggests that ion exchange is not the dominant mechanism of binding copper ions to the active sites in the molecular structure of the corn silk, but also chemisorption and physical adsorption is present.

4. Conclusions

The characterization of corn silk, as a potential adsorbent for copper ions biosorption is presented in this work. The SEM-EDS analysis was performed on corn silk samples before and after the biosorption of copper ions. The SEM analysis showed a change in the surface morphology of the corn silk samples after the biosorption process. The macro-pores and cavities, present on the SEM image before the biosorption process, disappeared, and the structure of the corn silk sample became more uniform and compact. The change in the morphology of the sample occurred as a result of the incorporation of the copper ions inside the structure of the corn silk.

DTA-TGA analysis was performed on a corn silk sample to determine its thermal stability. The sample was heated at a constant rate of 10 °C/min, from 20 °C to 900 °C. The obtained results showed a total weight loss of 69.1 % in the analysed temperature range indicating the degradation of the lignocellulose components in the sample.

The FTIR analysis was performed on samples before and after the Cu^{2+} ions biosorption. The obtained FTIR spectra showed no significant shifts in the terms of wavelengths. This led to the conclusion that ion exchange is not the dominant mechanism of binding copper ions to the active sites in the molecular structure of the corn silk, but also chemisorption and physical adsorption is present.

5. Acknowledgment

The research presented in this paper was done with the financial support of the Ministry of Education, Science and Technological Development of the Republic of Serbia, within the funding of the scientific research work at the University of Belgrade, Technical Faculty in Bor, according to the contract with registration number 451-03-68/2022-14/200131.

6. References

1. H. Yu, J. Pang, T. Ai, L. Liu, *J. Taiwan. Inst. Chem. Eng.* **62** (2016), 21-30.
2. G. Tan, H. Yuan, Y. Liu, D. Xiao, *J. Hazard. Mater.* **174** (2010), 740-745.
3. A. Bhatnagar, M. Sillanpää, *Chem. Eng. J.* **157** (2010), 277-296.
4. Q.-L. Hu, L.-J. Zhang, Y.-N. Li, Y.-J. Ding, F.-L. Li, *Int. J. Phys. Sci.* **5(4)** (2010), 321-326.
5. H. Yu, J. Pang, M. Wu, Q. Wu, C. Huo, *Anal. Sci.* **30** (2014), 1081-1087.
6. M. Petrović, T. Šoštarić, M. Stojanović, J. Petrović, Č. Lačnjevac, K. Trivunac, S. Stanković, *Zaštita Materijala* **57** (2016), 480-487.
7. J. O. Ighalo, A. G. Adeniyi, *SN Appl. Sci.* **2** (2020), Ar, No 509.
8. D. Božić, M. Gorgievski, V. Stanković, M. Cakić, S. Dimitrijević, V. Conić, *CICEQ* **27** (2021), 21-34.
9. M. Petrović, T. Šoštarić, M. Stojanović, J. Milojković, M. Mihajlović, M. Stanojević, S. Stanković, *J. Taiwan. Inst. Chem. Eng.* **58** (2016), 407-416.
10. P. M. K. Reddy, P. Verma, C. Subrahmanyam, *J. Taiwan. Inst. Chem. Eng.* **58** (2016), 500-508.
11. H. Yang, R. Yan, H. Chen, D. H. Lee, C. Zheng, *Fuel* **86** (2007), 1781-1788.

Application of characterisation methods in the development of biomedical titanium alloys

Magdalena Jajčinović[1,*], Ljerka Slokar Benić[1], Robert Pezer[1], Tamara Holjevac Grgurić[2]
University of Zagreb, Faculty of Metallurgy, Croatia[1]
Catholic University School of Medicine, Croatia[2]
magdalenaj@simet.unizg.hr

Abstract:
Biomaterials are becoming an increasingly important research topic over time as they are used to replace parts and functions of the human body, helping to improve the quality of human life. Titanium alloys are particularly important for the development of new biomaterials. Commercial pure titanium and its alloys are used as essential structural biomaterials in the manufacture of implants due to their excellent biocompatibility, good corrosion resistance and mechanical strength. However, studies have shown that aluminum and vanadium ions are released in alloys such as Ti-6Al-4V, which can cause health problems over time. Because of the problems that occur, researchers are working to improve the properties of titanium alloys by adding new elements. In most cases, different metals are added to titanium and it is known that with the presence of different metals, the properties of titanium also change. All biomedical titanium alloys must undergo various testing procedures before they can be used. The article describes the characterisation methods used in the development of titanium alloys, such as: light and scanning electron microscopy, energy-dispersive spectrometry, X-ray diffraction analysis, differential scanning calorimetry, differential thermal analysis. The reliability of the results depends on the methods used and the avoidance of errors in the characterisation of biomedical alloys in order to reach better conclusions and produce alloys of the highest quality desirable for use in the human body.

***Keywords**: BIOMEDICAL ALLOYS, Ti-ALLOYS, CHARACTERISATION, PROPERTIES*

1. Introduction

After the first meeting on biomaterials, held in South Carolina in 1969, the field of biomaterials received a lot of attention. [1] Nowadays, biomaterials play an important role. [2] Biomaterials are artificial or natural materials. They are used to make structures or implants to restore form or function or to replace a diseased or lost biological structure. [3,4] In this way, biomaterials help to improve the quality of life. [1] With the advances in medicine and materials processing in recent decades, a large number of biomaterials have been developed with properties suitable for various applications. [2] Metals have been used for decades for various applications in medicine. They are used in different parts of the body, such as artificial heart valves, as replacement implants in the knee, hip, elbow and shoulder, as stents in blood vessels and as dental implants. A large number of biomaterials are used for hip, spine and knee replacements. [1,5] Biomaterials must meet various criteria such as sufficient strength, bioadhesion, osseointegration ability, biofunctionality, high corrosion resistance, biocompatibility, high wear resistance and low friction. [6, 7] Biomaterials are also characterised by their biocompatibility. Biocompatibility is an important property of the material. [8] From studies conducted, elements such as Ti, Mo, Nb, Zr, W, Ta, Au and Sn are highly biocompatible, while Al, V, Cr and Ni are elements considered hazardous to the human body. Figure 1 shows detailed information about pure metals and their biocompatibility. [9]

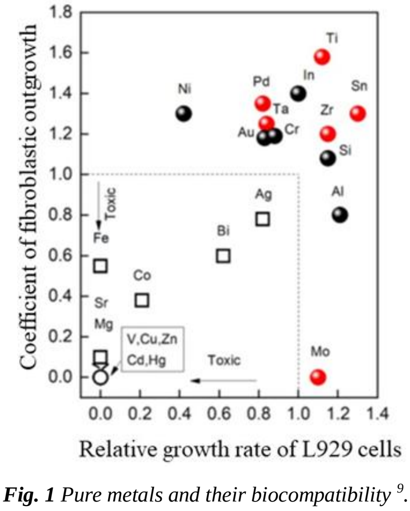

***Fig. 1** Pure metals and their biocompatibility [9].*

Metals and alloys used in biomedicine include stainless steels, titanium and cobalt based alloys. [6, 10] Only commercially pure titanium (CP-Ti) has the best biocompatibility among metallic materials, but its mechanical properties are not satisfactory. [11] Titanium and titanium alloys are currently the most commonly used metals in the manufacture of medical components, especially implants. Their natural properties such as low density and thus low weight, good corrosion resistance, low modulus of elasticity, wear resistance, high mechanical strength, relatively low modulus of elasticity, excellent biocompatibility and non-magnetic behavior give them an advantage over other metals such as chromium and cobalt alloys and stainless steels. [6, 9, 12] Titanium has long been considered a safe and inert element for human use. It also produces minimal side effects in the human body. This can also be considered one of the main reasons for using titanium as an implant. These alloys have better biocompatibility than stainless steel and cobalt-based alloys due to their good corrosion resistance. [2] However, in addition to the good properties mentioned, titanium alloys also have some poor tribological properties due to low resistance to plastic shear, low protection by surface oxides and low hardening. [6] Most of the published literature refers to the alloy Ti-6Al-4V because of its properties. However, there are some issues that limit the long-term use of these commonly used alloys as implants. Some of the disadvantages of these Ti-based alloys are that they lead to loosening of the implant and fracture of the bone due to the stresses being shielded due to the difference in elastic strength between the implant and the surrounding tissue, causing discomfort over a long period of time. [13] Concerns have been raised with the use of aluminium and vanadium as alloying elements regarding their harmful effects following the release of ions into the body, which can cause dermatitis, while in some cases implant rejection occurs. Although Ti-6Al-4V is considered highly resistant to corrosion, no material is completely bioinert. The release of ions can cause allergic reactions in some cases. Vanadium can have both positive and negative effects on the body. Therefore, great efforts have been made to develop titanium alloys with relatively harmless elements. Elements considered safer than aluminium and vanadium include niobium, tantalum and zirconium. Similarly, the release of aluminium and vanadium ions can cause neurodegenerative diseases such as Alzheimer's disease and peripheral neuropathy. It can be deduced that there is a need to explore metals that are better substitutes for alloying elements in Ti-alloys, as well as their properties. [13] With the increasing demand for durable implants, it has become necessary to accelerate research into the development of biomaterials, which should lead to a significant production of implants. [14]

2. Methods of characterizations

The article describes some of the test methods used in the development of titanium alloys. The methods described and explained in the article are characterisation methods using a light microscope (LM), a scanning electron microscope (SEM), an energy- dispersive spectrometer (EDS), X-ray diffraction (XRD), differential scanning calorimetry (DSC) and differential thermal analysis (DTA) methods. The aim of these methods is to characterise materials in order to determine suitable process parameters that will result in an alloy with a satisfactory microstructure or properties desirable for use in the human body.

Two types of microscopy are generally known. These are light microscopy (LM) and scanning electron microscopy (SEM). In light microscopy, the specimen is illuminated with visible light and the image is produced with a system of objectives and eyepieces. Scanning electron microscopy (SEM) is one of the most commonly used instrumental methods to examine and analyse the characterisation of solids containing micro- and nanoparticles. SEM can provide information on surface topography, crystal structure and chemical composition. It is used to obtain a realistic three-dimensional image of the surface of the sample under investigation. One of the reasons why SEM is preferred for particle size analysis is its resolution of 10 nm or 100 Å. The basics of SEM 's work involve scanning the surface of the sample under investigation with a very precisely focused electron beam. The smaller the electron beam, the smaller the surface of the sample and the more accurate the image. Energy dispersion X-ray spectroscopy (EDS) works in conjunction with SEM to provide qualitative and qualitative results. [15]

X-ray diffraction (XRD) is an increasingly important method for the qualitative and quantitative characterisation of crystalline materials. It is a particularly valuable analytical method because it is possible to obtain a large amount of necessary information based on a very small sample. A key feature of qualitative analysis is that the constituents are identified as specific compounds. [16] It provides information on phases, structures and parameters such as crystallinity, average grain size, defects and crystal deformations. It can be said that the sample obtained by this method actually corresponds to a fingerprint, i.e. the periodic arrangement of the atoms of the material under investigation. [17] X-ray diffraction is one of the most important methods for studying and diagnosing atomic structure, particle morphology, phase composition and a number of other structural features. After the discovery of the effects of X-ray diffraction, it has been successfully used to determine the structure of crystalline, conventionally crystalline and amorphous materials, as well as the size and shape of microscopic and submicroscopic particles in liquid and solid states. [18]

The most common methods of thermal analysis are differential scanning calorimetry (DSC) and differential thermal analysis (DTA). Thermal analysis is a method that has continued to develop in terms of new applications in the study of phase equilibria and phase transformation behaviour. [19] These methods have a major impact on materials science as they allow the measurement of a wide range of physical and chemical properties. They are also two closely related methods that analyse the change in temperature difference between a sample and a reference sample while subjected to temperature change and thermal effects in the material. Differential scanning calorimetry is a method in which the change in heat flow difference between a sample and a reference sample is analysed while they are subjected to a temperature change. Differential thermal analysis is a method in which the change in temperature difference between a sample and a reference sample is analysed while they are subjected to a temperature change. The notation of the DTA method is the differential thermocurve or DTA curve. [20] The above methods explain endothermic and exothermic processes at very low (-120°C) to high temperatures (DSC 600°C and DTA 1800°C). Physical properties measured by these methods include crystallisation temperatures, melting transitions, specific heat capacity, enthalpy of melting and crystallisation, liquid crystal transitions, solid-solid transitions, evaporation, sublimation, thermal conductivity and glass transition temperature. Chemical properties monitored by the above methods include oxidative reactions, solid-state reactions, dehydration, decomposition, chemisorption, combustion, hardening and polymerisation. [21] Depending on the measurement method used, a distinction is made between two measurement methods. These are differential scanning heat flow calorimetry (heat flow DSC) and differential scanning calorimetry with power compensation (power compensation DSC). [20, 21]

Ti- alloys

S. Y. Alshamari et al. analysed binary Ti-Cu alloys, i.e. Ti-0.5Cu, Ti-2.5Cu and Ti-5Cu, prepared by vacuum sintering of compacted powders. Using a light microscope, the sintered samples were found to have mostly closed spherical pores in the centre of the samples in the range of 15 to 50 μm. The alloys were sintered at a temperature of 1250˚C, resulting in the formation of spherical isolated pores. This is an indication that the sintered Ti-Cu alloys have reached the final stage of sintering. Since Cu is a stabilizer of the titanium β-phase, its addition leads to the formation of an α+β lamellar structure. Using SEM analysis, they found that there is a microstructural difference in the thickness and amount of β-phase between the different alloys, even when the amount of β-phase present increases. Only the increase in β-phase was determined by the XRD analysis. The XRD patterns of the sintered alloys Ti-2.5Cu and Ti-5Cu show the peaks of β-Ti and Ti_2Cu phases, especially in the Ti-5Cu sample. [22]

P. Pripanapong and colleagues conducted the tests on a Ti-Cu alloy with compositions Ti-2Cu, Ti-4Cu, Ti-7Cu and Ti-10Cu. The samples were sintered at 1000 °C for 1 hour in an argon atmosphere. The microstructure of the investigated alloys shows a 4% Cu alloy, which has a hypoeutectoid structure. The mentioned structure includes primary α-Ti (white phase) and eutectoid phase (lamellae α-Ti/Ti2Cu), which transforms from β-Ti at high temperature. The alloy with 10% Cu has a predominantly eutectoid structure. XRD analysis showed Ti-2Cu peaks corresponding to α-Ti only, while the Ti-10Cu alloy had α-Ti and Ti_2Cu peaks. In the differential thermal analysis (DTA), Ti-15Cu was investigated because the amount of copper added is the largest and it is also easier to detect a possible reaction between titanium and copper powder. The DTA curve showed an exothermic reaction at 1078°C, which is consistent with the melting temperature of pure copper. This compares to the XRD result of the sintered samples. The exothermic peak of the DTA analysis results indicates the formation of Ti2Cu in the alloy after the copper powder was melted. [23]

Algattaan and co-workers added another alloying element, in this case manganese, to the Ti-Cu alloy. Ti-0.5Mn-0.25Cu, Ti-1Mn-0.5Cu, Ti-2Mn-1C, Ti-3.5Mn-1.75Cu and Ti-5Mn-2.5Cu alloys were tested. The XRD diffractograms of the mentioned Ti-Mn-Cu alloys show that the α-phase of titanium is the primary phase forming the alloys. The relative intensity of the β-phase of titanium increases with the addition of a larger amount of alloying elements, as both manganese and copper are elements that stabilize the β-phase of titanium. Accordingly, it is expected that the β-phase of titanium in the microstructure of Ti-Mn-Cu alloys will be more pronounced in heavier alloy compositions. The microstructural analysis results show that the sintered Ti-Mn-Cu alloys have a fully lamellar microstructure composed of almost equal α-Ti grains and parallel α-Ti and β-Ti lamellae, regardless of the alloy composition. With increasing manganese and copper content, the relative amount of β-Ti phases present in the microstructure increases linearly. The higher manganese and copper content increases the fineness of the lamellae and thus decreases the spacing between them. [24]

Xu et al. investigated a biocompatible Ti-28Nb-35.4Zr alloy used as a bone implant. The results showed that the sintering temperatures have a significant influence on the mechanical properties of the alloys. SEM microphotography showed that the atomised powders have a typical spherical shape. XRD analysis showed that the atomised powders consist of a β-Ti, while the spherically milled powders consist of β-Ti and TiO_2. TiO_2 mostly appears because some oxygen is introduced during the ball milling process. The hardness of Ti-28Nb-35.4Zr alloy generally increases with increasing sintering temperature, which significantly improves the mechanical properties of the produced alloy. [25]

Examining Ti-Nb alloys, Haq et al. determined that before the start of heat treatment, the microstructure of the investigated alloy consisted mainly of separated α-Ti grains and Nb grains with a lamellar α- and β-structure at the interface between them. As the heat treatment was performed at 1200°C, the lamellar microstructure started to grow. After 4 hours of heat treatment, the microstructure consisted only of lamellar morphology. The microhardness of the sample increased with increasing heating time. The microstructure had no influence on the change in hardness. The phase change actually played a role in increasing the hardness. [26]

Kalita et al. prepared a Ti-Nb alloy with different chemical composition (Ti-14Nb, Ti-20Nb and Ti-26Nb) using the mechanical alloying method. In XRD analysis of the sintered alloy after sintering, they observed the β-phase. Only a small amount of hexagonal α-phase was present in the samples. Traces of the orthorhombic martensitic α" phase were observed in the Ti-14Nb and Ti-20Nb alloys. In the microstructure of the obtained alloys, β-phase grains with a size of 10-50 µm were observed in the case of the Ti-14Nb alloy. Darker areas of the Nb-depleted α-phase were present at the grain boundaries. It was found that the amount of α-phase decreases with the Nb content. Very bright areas of Nb were also observed. The presence of these particles leads to a decrease in the niobium content in the matrix. XRD analysis was also performed after heat treatment and confirms that the applied heat treatment resulted in a reduced amount of hexagonal α-phase. A regular β-phase was observed in all alloys. A martensite phase was observed within the β-phase grains in the microstructure of these alloys. The temperatures determined by DCS analysis for A_s and A_f were -12.4 and 2.2˚C, respectively. There were no visible effects associated with martensitic transformation in the Ti-20Nb and Ti-26Nb alloys. [27]

Zhou et al. prepared three types of Ti-Ta binary alloys (Ti-10Ta, Ti-30Ta, Ti-70Ta). Microscopic analysis showed that the tested alloys have lamellar and acicular microstructure. The SEM analysis showed the formation of passive oxide films on the surface of the samples. Oxide films formed on the surface of the Ti-30Ta alloy. The results of XRD analysis showed that TiO_2 formed on the surface of the Ti-10Ta alloy, while orthorhombic Ta_2O_5 films were present on the surfaces of the other alloys studied. [28]

Elshalakany and colleagues produced five alloys with different compositions (Ti-15Mo-6Zr, Ti-15Mo-6Zr-1Cr, Ti-15Mo-6Zr-2Cr, Ti-15Mo-6Zr-3Cr and Ti-15Mo-6Zr-4Cr). Optical micrographs showed that the Ti-15Mo-6Zr alloy mainly consists of the (α' + β)-phase. After addition of 1 wt%Cr, a small amount of the β-phase was detected. In all Ti-15Mo-6Zr-xCr alloys investigated, the microstructure of the whole alloy was transformed into a granular equiaxed β-phase. As the chromium content increased, the average grain size of the β-phase decreased. Unlike the Ti-15Mo-6Zr-xCr alloy, the microstructure of the Ti-15Mo-6Zr-2Cr alloy appears to consist of β-phase grains. In other words, in the Ti-Cr alloy system, the β-phase can be completely preserved after rapid cooling when the chromium content increases. The average grain sizes of the β-phase decreased with increasing chromium content. The Ti-15Mo-6Zr-2Cr alloy has the highest amount of β-phase and also showed the highest microhardness values (412 HV). [29]

Ho et al. investigated the structure and properties of a series of binary Ti-Mo alloys with molybdenum content ranging from 6 to 20 wt%. The experimental results of XRD analysis showed that the crystal structure and morphology of the cast alloys were sensitive to the molybdenum content. At a Mo content of 6 wt.%, a fine, acicular martensite structure of the orthorhombic α" phase was observed. At a molybdenum content of 7.5 wt%, the entire alloy was dominated by the martensitic α" structure, and when the molybdenum content was increased to 10 wt% or more, the retained β-phase became the only dominant phase. Of all the Ti-Mo alloys, the Ti-7.5-Mo alloy with α"-phase exhibited the lowest hardness. [30]

Luz et al. observed the Ti-40Zr alloy during sintering at a temperature between 800-1300°C. From the microstructure analysis, they determined that the formation of a two-phase (α+β) region started at a temperature of 800°C. The microstructure showed dark areas with titanium particles. Grey areas with dissolved zirconium particles were also visible. The two-phase (α+β) region becomes visible at 1000 °C and consists of a pure zirconium core surrounded by a two-phase microstructure. In the samples sintered at 1300 °C, a fine-plate α- and intergranular β-structure prevailed. Analysis of the results showed that slight additional densification occurs at temperatures above 1300°C. The hardness analysis values showed that as the temperature increases, the hardness value also increases. X-ray diffraction analysis revealed peaks related to the α- and β-phases of titanium, while the peaks of zirconium were not determined, confirming its complete resolution at a temperature of 1300°C. Zirconium-rich regions are present up to 1200°C. [31]

In their study, Slokar et al. produced a $Ti_{90}Zr_{10}$ alloy mixture that was analysed. The SEM analysis of the powders showed different morphologies of the starting powders, for example, the titanium powder consisted of spherical particles with a rough surface and the zirconium powder consisted of angular particles. In addition, a relatively high degree of agglomeration of the titanium particles was observed, as the smallest particles were not separated from the powder. In addition, after grinding $Ti_{90}Zr_{10}$ according to the SEM analysis and the corresponding EDS analysis, it was observed that many smaller particles retained their original shape as the particles were subjected to low energy collisions. In addition, only a small portion of the powder was agglomerated and deformed into flakes. After milling the powders, the EDS line scan confirmed that elemental zirconium remained, indicating that the milling parameters were not satisfactory for complete dissolution of zirconium into titanium. After sintering, a large number of pores were visible that were not spherical, indicating that the final stage of sintering had not been completed. Subsequently, the samples were subjected to SEM and EDS analysis and it was found that the zirconium content in the samples varied, indicating that the mixing of the starting powders was not done correctly. Peaks were only found for Ti and Zr in all the samples, and titanium was seen to be evenly distributed across the analysed range. [32]

Liu et al. investigated the microstructure of the powder metallurgy produced Nb-25Ti-xTa alloy (x = 10, 15, 20, 25, 35 at.%). In the SEM analysis of the alloy, the β-phase was very easy to detect. After sintering at 1700 °C, grain boundaries were clearly observed in the Nb-25Ti-xTa alloy. The average grain sizes were 50 µm, 46 µm and 33 µm. As the Ta content increased, the grain size decreased, while the dissolution rate of Nb and Ta into the Ti matrix increased with increasing sintering temperature. As the sintering temperature increased from 1600 °C to 1800 °C, a gradual transition to the β-phase occurred. It was also found that the acicular α-phase transitioned to the α + β-phase, and when the temperature increased to 1800 °C, a transition to the β-phase occurred. EDS line scanning was then performed to determine the distribution of the elements Nb, Ti and Ta in the Nb-25Ti-25Ta alloy sintered at 1600 °C. Titanium was the main element in the dark areas. As shown by the analysis of SEM, the pore size and shape gradually changed as a function of the sintering temperature. At higher sintering temperatures (1800 °C), there were more pores with regular shape, while at low sintering temperatures (1600 °C), the pores were mostly irregular in shape. XRD analysis of the sintered Nb-Ti-Ta alloys was also performed and it was found that the predominant diffraction peaks of the sample were from the spatially centred cubic (bcc) β-phase. Due to the small difference between the lattice parameters of Nb and Ta, the diffraction peaks of these elements overlapped. [33]

Popescu and colleagues investigated a new TiZrNbTaFe alloy. Based on the morphology of the starting powders, they found different spherical shapes for each type of elemental powder. They also found that the titanium powder consists of flattened angular particles, for zirconium they are needle-like particles, for niobium they are flaky, while for tantalum irregular particles with a slight tendency to spheroidise and for iron spheroidal particles can be seen. XRD analysis of the homogenised sample revealed that in addition to Ti, Zr, Nb and Fe powder, a combination of these elements with hydrogen or oxygen also occurs, which is due to the high degree of oxidation or hydration of the metal powder. After alloying the mixture for 20 hours, the analysis of SEM showed that the formation of NbTiZr phases was predominant, with some unalloyed powders also visible. Based on the results of the X-ray analysis, it could be assumed that the alloying process had started, but that the milling time was not sufficient to achieve complete mixing of the powders into a homogeneous mixture. Thus, Ti made up 45 % of the powder mixture, Fe 17 %, Ta 12 %, Zr 4 % and the Nb content was 3 %.[34]

3. Conclusion

The excellent properties of titanium alloys have made these alloys a very important material for various applications, especially in biomedicine. Although titanium and titanium alloys are widely used biomedical materials, research continues in order to obtain the highest quality and most reliable material possible. The above overview shows the importance of the presented conventional methods for the development of biomaterials. However, they should be applied together with other characterisation methods in order to be able to adjust the parameters of the biomaterials manufacturing process based on the characterisation results obtained, with the aim of obtaining titanium alloys with satisfactory properties for biomedical applications.

4. References

1. M. Geetha, A.K. Singh, R. Asokamani, A.K. Gogia, Materials Science, **54**, 97-425 (2009).
2. A.J. Festas, A. Ramos, J.P. Davim, Proceedings of the Institution of Mechanical Engineers, Part L, **234**, 1-11 (2019).
3. M. Kaur, K. Singh, Materials Science and Engineering: C,**102**, 844-862 (2019).
4. L.-C. Zhang, L.-Y. Chen, Adv. Eng. Mater., 21, 1-29, 2019.
5. C. S. Pitchi, A. Priyadarshini, G. Sana, S.K. R. Narala, Materials Today: Proceedings, **26**, 3297-3304 (2022).
6. FA Anene, CN A. Jaafar, I Zainol, MA Azmah Hanim, MT Suraya, Proc IMechE Part C: J Mechanical Engineering Science 235, 1-14 (2020).
7. W. Xu, Z. Liu, X. Lu, J. Tian, G. Chen, B. Liu, Z. Li, X. Qu, C. Wen, Science China Materials, **62**, 1-12 (2019).
8. K. Pałka, R. Pokrowiecki, Adv. Eng. Mater., **20**, 1-18 (2018).
9. M. A. Hussein, A. S. Mohammed, N. Al-Aqeeli, Materials, **8**, 2749-2768 (2015).
10. V. S.de Viteri, E. Fuentes, TribologyFundamentals and Advancements, **5**, 1-28 (2013).
11. S. Lascano, C. Arévalo, I. Montealegre-Melendez, S. Muñoz, J. A. Rodriguez-Ortiz, P. Trueba, Y. Torres, Appl. Sci, **9**, 982 (2019).
12. F. Mahyudin, H. Hermawan, Biomaterials and Medical Devices. Vol. 58, Springer International Publishing, **58**, 1-249 (2016).
13. S. Agarwal, J. Curtin, B. Duffy, S. Jaiswal, Mater. Sci. Eng. C, **68**, 948-963 (2016).
14. D. Annur, I. Kartika, S. Supriadi, B. Suharno, Mater. Res. Express, **8** ,1-24 (2021).
15. A. Mohammed, A. Abdullah, Proceedings of 2018 International Conference on Hydraulics and Pneumatics-HERVEX, 1-9 (2018).
16. A. L. Ryland, Journal of Chemical Education, **35**, 1-4 (1958).
17. A. A. Bunaciu, E. G. Udriştioiu, H. Y. Aboul-Enein, Critical Reviews in Analytical Chemistry, **45**, 289-299 (2015).
18. G.V. Fetisov, Physics-Uspekhi, **63**, 2-32 (2020).
19. K. Hildal, Handbook of Thermal Analysis and Calorimetry, **6**, 781-828 (2018).
20. C. Schick, D. Lexa, L. Leibowitz, Characterization of Materials, 1-13 (2013).
21. R. A. Meyers A. Riga, R. Collins, Encyclopedia of Analytical Chemistry, 1-33 (2020).
22. A. Mohammed, A. Abdullah, J. Mech. Behav. Biomed. Mater., (2019).
23. P. Pripanapong, T. Luangvaranunt, Advanced Materials Research, **93**, 99-104 (2010).
24. M. Alqattan, L. Peters, Y. Alshammari, F. Yang, L. Bolzoni, Regenerative Biomaterials, 1-8 (2020).
25. W. Xu, M. Li 1, C. Wen, S. Lv, C. Liu, X. Lu, X. Qu, Materials, **11**, 1-12 (2018).
26. M.A. Haq, S.F. Abbas, N.S.A. EOM, T.S. Kim, B.Lee, K.-T. Park, B.S.Kim, Arch. Metall. Mater., **63**, 1429-1432 (2018).
27. D. Kalita, Ł. Rogal, T. Czeppe, A. Wojcik, A. Kolano-Burian, P. Zackiewicz, B. Kania, J. Dutkiewicz, Journal of Materials Engineering and Performance, **29**, 1445-1452 (2022).
28. Y. L. Zhoua, M. Niinomi, T. Akahori, H. Fukui, H. Toda, Materials Science and Engineering A, **398**, 28-36 (2005).
29. A. B. Elshalakany, S. Ali, A. A. Mata, A. K. Eessaa, P. Mohan, T.A. Osman, V. A. Borras, Journal of Materials Engineering and Performance, **26**, 1262-1271 (2017).
30. W.F. Ho, C.P. Ju, J.H. Lin, Biomaterials, **20**, 2115-2122 (1999).
31. T. dos Rei Luz, V. A. Rodrigues Henriques, J. L. de Oliveira, E. F. Diniz, SAE Technical Paper Series [SAE International 22nd SAE Brasil International Congress and Display - (OCT. 07, 2013)] SAE Technical Paper Series, **1**, 1-6 (2013).
32. Lj. Slokar, A. Štrkalj, Z. Glavaš, Engineering Review, **39**, 115-123 (2019).
33. J. Liu, L. Chang, H. Liub, Y. Li, H. Yanga, J. Ruan, Mater. Sci. Eng. C, **71**, 512–519 (2017).
34. G. Popescu, B. Ghiban, C. A. Popescu, L. Rosu, R. Truscă, I. Carcea, V. Soare, D. Dumitrescu, I. Constantin, M. T. Olaru, B. A. Carlan, Mater. Sci. Eng., **400**, 1-9 (2018).

The influence of electrochemical corrosion on the structure and phase composition of a sintered multicomponent titanium-based composite in a 3% NaCl solution

Oksana Baranovska[1], Gennadii Bagliuk[1], Oleksandr Bykov[1], Oleksandr Hrypachevsky[2], Viktor Talash[1],
Yulia Rudenko[1], Dmytro Baranovskyi[1]

Frantsevich Institute for Problems in Materials Science[1], Kurdyumov G.V. Institute for Metal Physics[2] of the NASU, Kyiv, Ukraine, 03142
E-mail: ksenya.suprun@gmail.com, gbag@ukr.net

Abstract: *The electrochemical corrosion properties in a 3% NaCl solution of the titanium-based multicomponent composite of the $65TiH_2$–$30FeSiMn$–B_4C system were investigated. The kinetics and the mechanism of anode dissolution of metals and oxidation of specimens have been studied by using polarization curves, chemical and x-ray phase analyses. It was found a decrease in the titanium carbide peaks on the X-Ray defractions also the titanium silicon carbide almost disappears after immersing the sample in a 3% NaCl solution. Formation of silicon and boride phases of titanium in the synthesis process leads to an increase in corrosion resistance due to the inhibition of the velocities of both the anode and cathode processes.*

KEYWORDS*: POWDER MATERIALS, ELECTROCHEMICAL CORROSION, POLARIZATION CURVES, TITANIUM SILICON CARBIDE, TITANIUM CARBIDE*

1. Introduction

For the successful development of modern technology, it is necessary to create new materials that can work in extreme conditions and possess of physical and technical properties: refractory, heat resistance, wear resistance, resistance to aggressive environments.

Titanium and titanium-based materials are among the stable materials in many aggressive environments, especially in the electrochemical corrosion, for example, in the marine environment or in the wastewater environment. Which is caused by the rapid formation of a titanium thin inert film of dioxide on its surface, which interacts with the lower layer of titanium with the formation of lower oxides soluble in the metal.

In recent years, powder metallurgy methods have been increasingly used for the production of titanium materials [1-3]. One of the effective options for obtaining sintered titanium-containing materials is the use of titanium hydride powders instead of serial titanium powder as raw materials [4,5].

In [6], the results of the electrochemical corrosion test of three-layer ceramics based on Ti_3SiC_2 are presented. Titanium silicon carbide is highly stable in concentrated hydrochloric acid solution and exhibits high crystalline hydrogen evolution activity. In [7] Ti_3SiC_2 exhibits excellent tribocorrosion resistance *in situ* due to the formation of an oxide film on the surface was found, unlike pure titanium. Thus, it can be concluded that Ti_3SiC_2 can have very wide prospects for the use in seawater as a substitute for non-corrosive components. However, obtaining titanium silicon carbide requires the use of many technological operations [8], as well as the use of pure powders of titanium, silicon and graphite as raw materials, which significantly increase the price of the finished product.

The appropriateness of choosing an alloying element to obtain our multicomponent material is determined by technical and economic factors. Thus, the introduction of up to 3÷5% of iron, silicon or manganese into the composition of the powder charge significantly increases the strength of the sintered alloy. In addition, during the synthesis of titanium hydride with ferro-silicon-manganese, there is an active interaction with the formation of hard and wear-resistant silicide phases of titanium, which favorably affect corrosion resistance in sea water and sulfuric acid. Additional introduction of boron, carbon, or nitrogen transition metals to IV-VI groups makes it possible to obtain a composite material with a combination of unique electrophysical and mechanical properties, while having chemical and thermal stability [9,10].

A number of interesting temperature and mechanical properties of borides, for example, a high melting point and high hardness, have already been studied and successfully exploited in such areas as wear-resistant products. Composite materials that include borides make it possible to use them in high-tech areas, along with well-known oxide ceramic materials, as well as silicon carbide and hard alloys [11].

Considering the above, ***the aim*** of this paper is to study the influence of a 3% NaCl solution on the stability of a multicomponent titanium based composite doped with ferrosilicomanganese and boron.

2. Objects and research methods

As the base of charge, we used powders of PTKh-80 titanium hydride with a particle size of ≤ 63μm. The main alloying elements were added to the charge in the form of MnS-17 ferro-silicon-manganese (FSM) powder with a particle size of ≤ 80 μm the chemical composition of which is given in the table 1 and boron carbide with a particle size ≤ 50 μm. The morphology of the powders of the initial charge is shown in Fig. 1.

Table 1: Chemical composition of Ferro-Silicon-Manganese MnS-17 (%, wt.)

Mn	Si	Fe	C
62,5	14,1	21	2,1

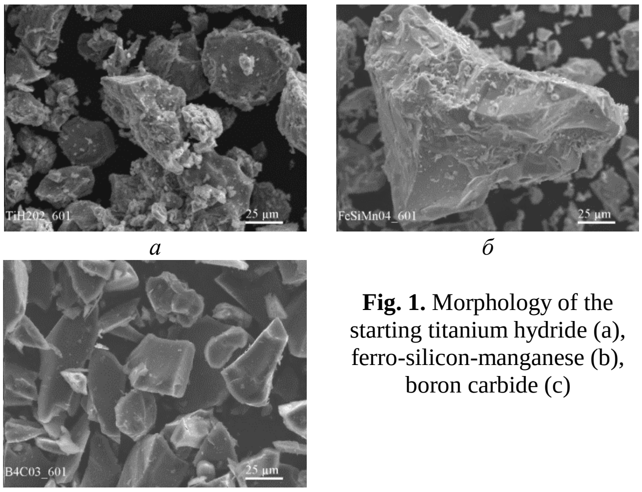

а   *б*

в

Fig. 1. Morphology of the starting titanium hydride (a), ferro-silicon-manganese (b), boron carbide (c)

The initial powder mixture was mixed in a ball mill in an alcohol for 6 hours with grinding carbide balls (diameter of 4–12 mm) and a ratio of the mass of the mixture to the mass of the balls of 1:5.

Samples of size 43×6×6 mm were pressed from the obtained mixture under a pressure of 500 MPa. The test samples were sintered in a vacuum furnace type СШВЛ - 1.2,5/25-M04 with a heating rate of 5-7 degrees/min in two successive stages: heating to 600 ^oC with isothermal holding for 30 min (to remove the main amount of hydrogen), further heating to 1250 ^oC with exposure for 60 min.

The microstructures of the starting powders after mechanoactivation was examined employing REM-106Y scanning electron microscope.

The change in the local chemical composition of the samples was studied by X-ray spectral analysis using the MS-46 "Cameca" microprobe. The phase composition was determined by X-ray defraction in filtered Co-K_α (λ = 0.15418) radiation using a DRON-3M diffractometer. The diffractograms were processed using the ORIGIN 2016 program to determine the reflection angles and lattice parameters. The phase composition of the samples was determined by the intensity distribution along the diffraction vector.

The process of electrochemical oxidation of the material was carried out by the method of obtaining anodic polarization curves with a potential sweep speed of 0.5 mV/s on a PI-50-1 potentiostat in a 3% NaCl solution. A platinum electrode was used as a cathode; anode potentials were measured using a silver chloride reference electrode. The studied sample was not subjected to grinding before the test due to high fragility.

3. Results and discussion

Figure 2 shows the schematic of a cathodic and anodic polarization curve after electrochemical oxidation of the synthesized TiH2-FeSiMn-B4C in 3% NaCl solution.

It is known [12] that during anodic oxidation of binary compounds of transition metals, the formation of a wide range of oxides should be expected. This is especially characteristic of titanium, which forms compounds with different degrees of oxidation.

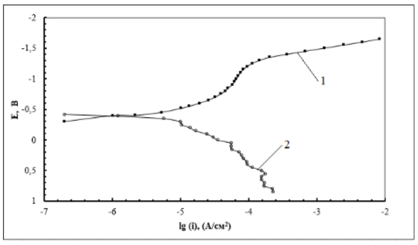

Fig. 2. *Cathodic (1) and anodic (2) polarization curves of the 65TiH2-30FeSiMn-5B4C composite in a 3% NaCl solution*

As can be seen from curve 2 (Fig. 2), in the initial range of potentials from stationary (Est = -0.42 V) to -0.3 V, active anodic oxidation is observed, which is accompanied by its dissolution in the electrolyte with transition to a solution of Ti^{3+} ions. On the basis of curve 2 (see Fig. 2), the following anodic process on the TiB surface can be proposed: in the range of potentials Est = - 0.3 V, Ti^{3+} ions and boric acid ions pass into the solution:

$$TiB + 3H_2O = Ti^{3+} + BO_3^{3+} + 6H+ + 6e^- \quad (1)$$

With the development of the anodic process, passivation of the sample with the formation of a TiO2 (rutile) film is observed at potentials more positive than -0.3 V, which is evidenced by the changed slope of the polarization curve:

$$TiB + 5H_2O = TiO_2 + BO_3^{3+} + 10H^+ + 7e^- \quad (2)$$

The cathodic recovery process (curve 1), which occurs on the surface of the sample, proceeds as actively as the anodic process. According to the course of the curves, the rate of corrosion is controlled by the course of reactions (1) and (2), i.e., the value of the limit oxygen current.

Taking into account that electrochemical reactions occur on the surface of the material, the nature of the distribution of phases and their composition, which are in direct contact with the aggressive environment, is important. For this purpose, the microstructure and surface composition of the material before and after oxidation were investigated. The material 65TiH2/30FeSiMn/B_4C has a heterophase microstructure based on grains of titanium carbide, titanium silicide, titanium boride, a matrix in the form of a Ti-Mn compound and some amount of ternary carbide Ti_3SiC_2. X-ray phase analysis is presented in Fig. 3.

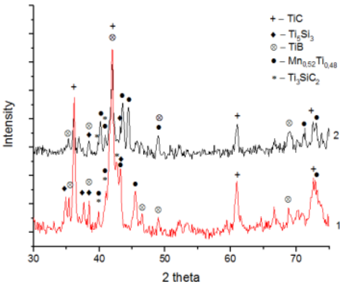

Fig. 3. *Fragment of the X-ray diffraction pattern of an alloy synthtesized at 1250°C from the TiH_2-FeSiMn-B_4C: 1 – sample after synthesis, 2 – sample after synthesis immersed in a 3% NaCl solution*

Based on the X-ray diffraction pattern (Fig. 3(1) before the sample is immersed in a 3% NaCl solution), the matrix phase is presented in the form of the Ti–Mn system, there is a significant number of clear lines of silicide phases (Ti_5Si_3). The main phase is titanium carbide, which is located at angles of 36°; 42°; 61° and 73°, whose diffraction maxima are (111), (200), (220), (311), respectively. Reflexes of titano-silicon carbide Ti_3SiC_2 and some amount of TiB were also observed.

After immersing the sample in 3% NaCl (Fig. 3(2)), the diffraction pattern changes slightly: a decrease in the intensity of the carbide peaks is observed. The most intense reflection (200) is almost halved from 100.0 to 58.3, probably due to the formation of a passivation film. Titanium silicon carbide almost disappears and the amount of silicide phase decreases. As noted in [6], the decrease in the number of these phases indicates that most of the Ti and Si atoms in the lattice are selectively dissolved in the solution, and carbon remained in free form. The chemical bond between the Si and Ti–C layer was very weak, and the electrical conductivity could be mostly attributed to the 3d electrons of titanium atoms adjacent to silicon. Therefore, most electrons in the loop were provided by titanium and silicon easily diffused into the solution during corrosion.

The corrosion/passivation mechanism could be sketched in Fig. 4 that layered crystal structure and weaker chemical bond between Si and Ti–C layer made silicon atoms are more likely diffused outward which promoted the reaction [6].

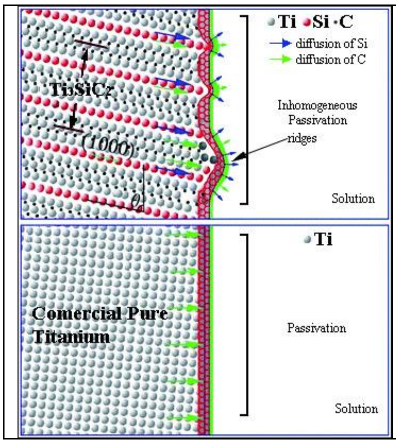

Fig. 4 The Schematic of passivation in 3.5% NaCl solution and the difference, (a) schematic of Ti_3SiC_2, (b) schematic diagram of CP titanium. [6].

Silicon and titanium inhomogeneous diffusion reduced efficiency of passivation films generation and a great deal of silicon and titanium atoms loss into solution and which could be due to the increasing of polarization potential.

On the contrary, titanium atoms in CP Ti diffused uniformly into the barrier layer enhanced the protection of the passivation film as shown in Fig. 4b.

The microstructure of the surface of the material before and after oxidation differs significantly (Fig. 5). Before the tests (Fig. 5(a)), the Mn-Ti matrix phase (Table 2) and the carbide phase separation (Table 2 phase 1) were observed on the surface of the sample. After testing the sample for electrochemical corrosion, a passivating film appears on the sample surface (Fig. 5b). Such structural changes occurred as a result of partial dissolution of less stable surface layers based on Ti and Si.

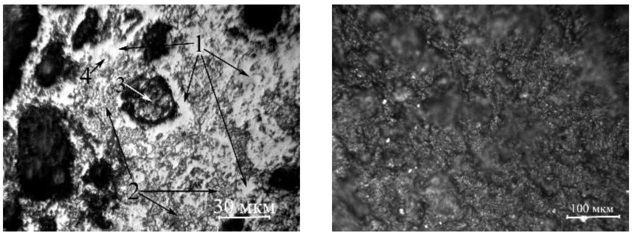

a b

Fig. 5. X-ray microspectral analysis of sintered samples obtained from the 65TiH$_2$/30FeSiMn/B$_4$C powder mixture:
a – sample after synthesis at 1250^{o}C, b – sample after synthesis immersed in a 3% NaCl solution

Table 2: Chemical composition of elements in different phase components of the 65TiH$_2$/30FeSiMn/B$_4$C composite (%, wt.)

	Fe	Mn	Si	Ti	C/B	Фаза
1	0,36	0,73	0,17	78,96	19,94	TiC
2	7,83	14,74	1,66	69,32	6,44	Mn_xTi_x
3	7,86	24,52	0,39	65,11	2,12	Mn_xTi_x
4	10,68	44,56	2,81	39,01	2,95	Mn_xTi_x

4. Conclusion

The electrochemical corrosion properties in a 3% NaCl solution of a multicomponent composite based on titanium, system 65TiH2–30FeSiMn–B4C, were studied. It was found that after immersing the sample in a 3% NaCl solution, the radiograph shows a decrease in the titanium carbide peaks by half, the titanium silicon carbide almost disappears. Amount of the silicide phase also decreases, which is associated with the dissolution of the Ti and Si phases in the solution.

The corrosion/passivation mechanism of Ti/Si/C compared to commercially pure titanium was elucidated. A high resistance to anodic oxidation was established, which is due to the formation of a protective TiO$_2$ (rutile) film on the surface of the sample. The conducted research makes it possible to predict the corrosion behavior of new titanium-based composites during their operation in natural environments.

5. References

1. Froes F. H., Eylon D. Powder-Metallurgy of Titanium Alloys // Int. Mater. Rev. – 1990. – Vol., 35, (3). – P. 162–182.

2. Liu Y., Chen L. F., Tang H. P., Liu C. T., Liu B., Huang B. Y. Design of Powder Metallurgy Titanium Alloys and Composites // Materials Science and Engineering. A. – 2006. – Vol. A418, (1–2). P. 25–35.

3. Whittaker D. Powder Processing, Consolidation and Metallurgy of Ttanium // Powder Metallurgy. – 2012. – Vol. 55; No. 1. – P. 6-10.

4. Ivasyshyn O.M., Bagliuk G.A., Stasyuk O.O., Savvakin D.G. The Peculiarities of Structure Formation Upon Sintering of TiH2+TiB2 Powder Blends // Physics and Chemistry of Solid State. - 2017. - Vol. 18, No. 1. - P. 15-20.

5. Bagliuk G.A., Stasyuk A.A., Savvakin D.G. Structure and Phase Composition of Sintered Alloys Obtained From Powder Mixtures of the TiH$_2$+TiB$_2$ System // Powder Metallurgy: Surface Engineering, New Powder Materials. Quarrel. - Minsk: "Belarusian Science", 2017. - P. 347-359.

6. Ming Zhu, Rui Wang, Chen Chen, Haibin Zhang and Guojun Zhangc Electrochemical Study on the Corrosion Behavior of Ti$_3$SiC$_2$ in 3.5% NaCl Solution // RSC Advances. – 2017. – Vol.7; Iss. 21 – P. 12534-12540.

7. Jovic V. D. Corrosion Behavior and Passive Film Characteristics Formed on Ti, Ti$_3$SiC$_2$, and Ti$_4$AlN$_3$ in H$_2$SO$_4$ and HCl / V. D. Jovic, M. W. Barsoum. // Journal of The Electrochemical Society. – 2004. – Vol.151; No.2. – P. B71–B76.

8. Zhou Y., Sun Z., Chen S. & Zhang Y. (1998). In-situ Hot Pressing/Solid-Liquid Reaction Synthesis of Dense Titanium Silicon Carbide Bulk Ceramics // Materials Research Innovations. – 1998. – Vol. 2; No.3. – P.142–146.

9. Shein A.V., Pavroznyk V.S., Rokytyanskaya I.L. Silicides of Transition Metals - Promising Corrosion-Resistant Electrode Materials // 18th Mendeleev Congress on General and Applied Chemistry. Moscow. – September 23-28, 2007. Abstracts of reports. T. 2. Chemistry of metals, nanostructures and nanotechnology. - M.: Granitsa. - 2007. - P. 616.

10. Boltovets N.S., Ivanov V.N., Konakova R.V. SiC Schottky- Barrier Diodes Formed with TiB(x) and ZrB(x) Amorphous Layers / N.S. Boltovets, V.N Ivanov, R.V. Konakova and all. // Semicond. Phis., Quantum Electron and Optoelectron. – 2004. – 7. 1. – P. 60–62.

11. Danylovich D.P., Kayumov R.A., Mukhamedova I.Z. High-Temperature Properties of Ceramics Based on Titanium Diboride and Silicon and Boron Carbides / D. P. Danylovich, R. A. Kayumov, I. Z. Mukhamedova. // Bulletin of the Kazan Technological University. – 2014. – Vol. 17 No. 9. – P. 28–30.

12. Chirkin A.D., Lavrenko V.A., Talash V.N., Panasyuk A.D. Formation of Oxide Nanofilms on The Surface of Titanium, Molybdenum, and Tungsten Disilicides During Anodic Polarization // Dop. NAS of Ukraine. – 2006. – No. 12. – P. 96–101.

Composite graphene/nanocarbons prepared by one-step reduction reaction

Nadia Todorova[1,2*], Vera Marinova[1] , Dimitre Dimitrov[1,3], Christos Trapalis[2]
Institute of Optical Materials and Technologies, Bulgarian Academy of Science, bl. 109 “Acad. G. Bonchev” Str., 1113 Sofia, Bulgaria[1]
Institute of Nanoscience and Nanotechnology, National Centre for Scientific Research “Demokritos”, 15341 Athens, Greece[2]
Institute of Solid State Physics, Bulgarian Academy of Science, 72 Tzarigradsko Chaussee Blvd, 1784 Sofia, Bulgaria[3]
n.todorova@inn.demokritos.gr

Abstract: *Nowadays, the decrease of CO_2 concentration in the atmosphere and/or its utilization need urgent resolution. At the same time, preparation of advanced graphene-based composites through effective environmentally benign procedures remains in the focus of intensive research. In the present work, composites consisted of reduced graphene oxide and nanocarbons (rGO/nC) were prepared by simultaneous reduction reaction of solid graphite oxide and CO_2 gas over alkaline earth reductant. The structure and the morphology of the prepared composite material were examined employing X-ray diffraction analysis and scanning electron microscopy. It was revealed that the characteristic narrow peak of the graphite oxide (GtO) at low 2θ ($\sim 11^o$) was not present in the pattern of the composite suggesting its successful reduction. Instead, a broad one positioned at 26^o was recorded which was attributed to the formed nanocarbons. The observed accordion-like morphologies typical for reduced-graphene-oxide type of graphene evidenced the detachment of the graphene layers during the thermal treatment, while the formed nanocarbons were with irregular shape. The rGO/nC composite exhibited specific surface area (485 m^2/g) higher than the pure nanocarbons (417 m^2/g) obtained without addition of GtO. The outcome was attributed to the influence of the layered rGO which hinders the aggregation of the nanocarbons and facilitates their homogeneous distribution. The prepared composite can be considered as candidates for gas and energy storage applications, while the suggested environmentally benign preparation method can be scaled up to industrial extent due to simplicity.*

Keywords*: 2D COMPOSITES, REDUCED GRAPHENE OXIDE, NANOCARBONS, CO_2*

1. Introduction

The development of graphene-containing composite materials remains in the focus of the research community due to the constantly increasing variety of application of this type of materials, but also due to the search for effective, scalable methods for their preparation [1, 2]. Graphene in the form of reduced graphene oxide (rGO) is often coupled with other carbonaceous materials such as carbon nanotubes, activated carbon, etc. in order functional properties like conductivity, specific surface area, stability etc. to be further improved. The main approaches for composite preparation are *in situ* synthesis of the second component in presence of rGO, as well as simultaneous decoration and reduction of the parent graphite oxide (GtO). Methods such as chemical reduction with suitable substances and thermal reduction in various gas or vacuum atmosphere, as well as combination of them are among the most used [3, 4].

On the other hand, the high concentration of greenhouse gases in the atmosphere, especially the CO_2 pollutant, needs to be urgently tackled. Metallothermic reduction of CO_2 to carbon nanostructures is one of the used methods which employs alkaline earth elements usually Mg as reductant [5]. Various modifications of the Mg and CO_2 precursors have been reported such as using additions of other metals like Zn and Ca to facilitate the CO_2 reduction [6], [7], but also using other substances for example silica, instead of the CO_2 in order to be reduced by the Mg under inert atmosphere [8].

In the present work, solid graphite oxide was added to Mg in order to be reduced by the metal along with the flowing CO_2 gas, aiming at preparation of composite rGO/nanocarbons in one-step GtO and CO_2 reduction reaction. The structural and morphological properties of the composite material were investigated in comparison with pure nanocarbons prepared in absence of GtO.

2. Experimental

2.1. Synthesis of the materials

The initial free-standing paper-like graphite oxide was prepared by oxidation of natural graphite applying a modified Hummers method as described in [9]. Then, the GtO was subjected to metallothermic treatment in CO_2 flow at conditions similar to those in [10]. In this experiment, a mixture of GtO and Mg powder in ratio 1:5 was placed in tube furnace onto an alumina scaffold and cured at 675 °C for 1 h under CO_2 flow. The heating up to the target temperature and the natural cooling after the reaction were performed under Ar flow. Subsequently, the obtained powder was treated in boiling 3M HCl for 1 h under reflux and washed /centrifuged with deionized water until pH 7 in order the co-product MgO and the unreacted Mg to be removed. Finally, the solid material was dried at 80 °C overnight, collected and nominated as rGO/nC. For reference purpose, pure nanocarbons were prepared at the same conditions without addition of GtO which were named nC.

2.2. Characterization

The crystalline structure of the prepared pure and composite materials were investigated through XRD analysis employing Siemens D500 instrument with CuKa radiation source. The patterns were recorded in the 2θ range 2 - 70° with velocity 0.03°/2 s. SEM analysis was performed using FEI Inspect electron microscope with tungsten filament operating at 25 kV. The porosity of the materials was investigated using Quantachrome Autosorb-iQ instrument. Prior measurement, the samples were degased at 120 °C for 12 h. The Brunauer-Emmett-Teller (BET) specific surface area and the total pore volume were determined from the liquid N_2 adsorption isotherms, while the pore size distribution was received from the desorption branch of the isotherms applying BJH analysis.

3. Results and discussion

The XRD patterns of the initial GtO, the intermediate rGO/nc before the acid treatment and washing, as well as the final pure nC and rGO/nC are presented in Fig. 1 and 2.

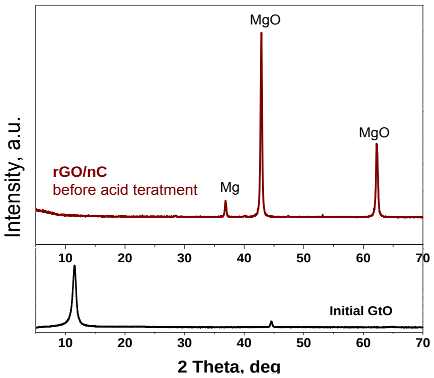

Fig. 1 *XRD patterns of the initial graphite oxide (GtO) and the composite rGO/nC.before the acid treatment.*

It is evident that the narrow peak of the GtO at low 2θ ~11^{o} is not present in the pattern of the intermediate (Fig. 1) and the final composite (Fig. 2). This outcome indicates that the initial GtO was either delaminated/reduced to rGO or its content in the composite is below the detection limit of the technique. Also, the well-defined peaks of MgO and Mg recorded for the intermediate composite were not present in the patterns of the final rGO/nC and pure nC, evidencing their successful removal by the acid treatment. Instead, a broad peak positioned at ~26^{o} was recorded which was attributed to the (002) diffraction line of the formed nanocarbons [5].

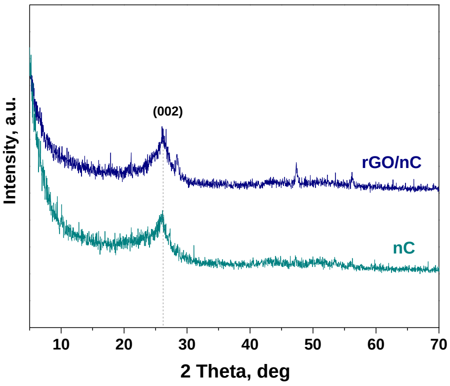

Fig. 2 *XRD patterns of the final pure nanocarbons (nC) and composite material (rGO/nC).*

The results from the SEM analysis presented in Fig. 3 and 4 are in good accordance with the XRD results. Specifically, from Fig. 3 it is evident that the stacked layers of the GtO (a and b) were detached after the metallothermic treatment resulting in accordion-like network (c and d) that is typical for thermally reduced graphene oxide [11]. The irregular aggregates in these images are attributed to carbon nanostructures together with the co-product MgO and non-reacted Mg.

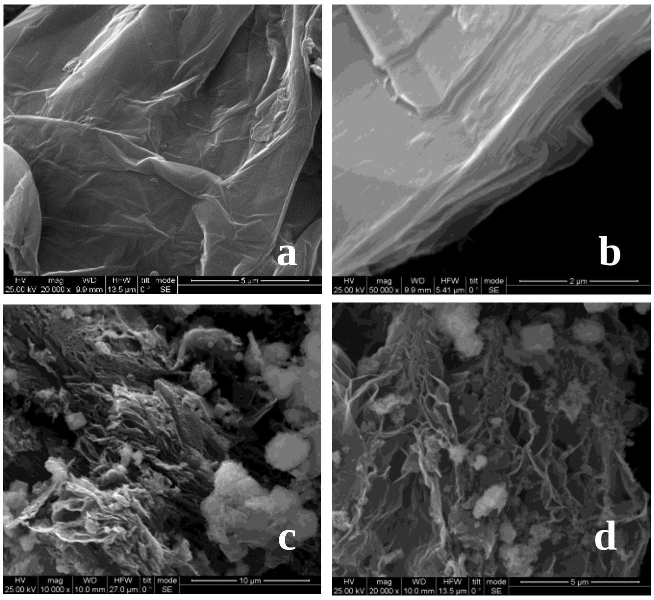

Fig. 3 *SEM images of the initial graphite oxide (a, b) and the composite rGO/nC before acid treatment and washing (c, d).*

In Fig. 4, SEM images of the composite rGO/nC and pure nC after the acid treatment and washing are given. For the composite, two types of morphologies, i.e. thin packs of layers and particles' aggregates can be observed, while for the pure nC only the second type is present. It can be expected that the rGO sheets will influence the porosity acting as a support for the *in-situ* formed nanocarbons. The fact that the rGO layers in the sample after the acid treatment (Fig. 4 a and b) appear more detached in comparison to those before the treatment (Fig. 3 c and d) can be related to the influence of the hot HCl which reacts with the MgO and Mg and contribute to the rGO delamination and nanocarbons dispersion.

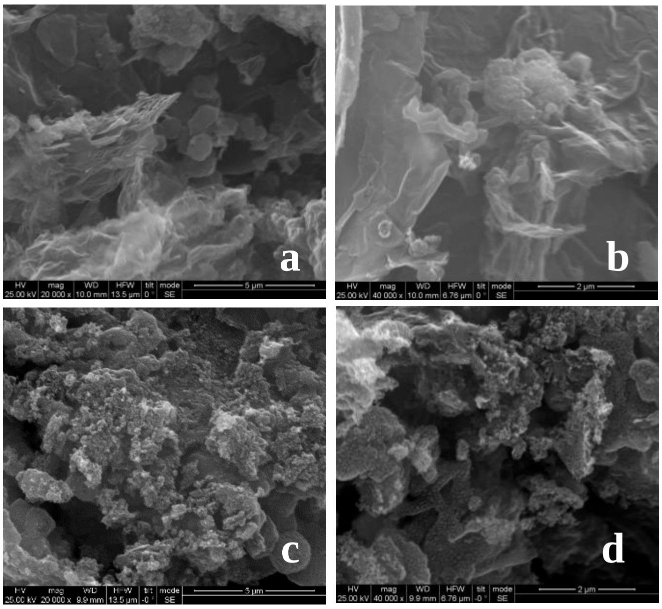

Fig. 4 *SEM images of the final composite rGO/nC (a, b) the pure nanocarbons (c, d).*

The performed liquid N_2 adsorption-desorption measurements verified the increase in the porosity of the composite rGO/nC in comparison to the initial GtO and pure nC sample. The isotherms and pore size distribution for the samples are presented in Fig. 4.

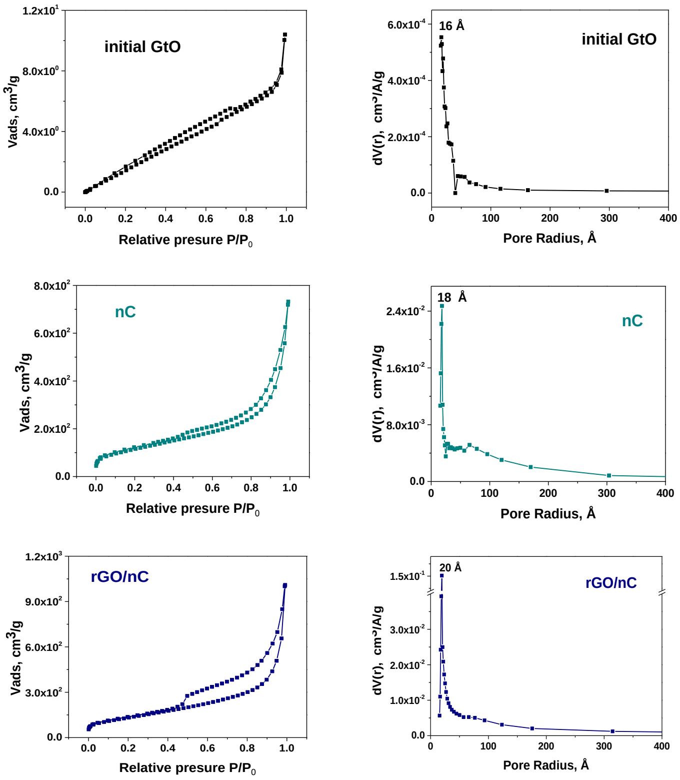

Fig. 5 *Liquid N_2 absorption-desorption isotherms and the pore size distribution plots of the initial graphite oxide (GtO), the pure nanocarbons (nC) and the composite rGO/nC.*

The absorption branches can be categorized as type II and IV typical for makro- and mesoporous solids. The hysteresis loop formed due to different behavior in adsorption and desorption at the same pressure P/P_0 matches H3 type, which is characteristic for materials consisted of aggregates from non-uniform particles forming slit shaped pores [12]. The hysteresis is more prominent in the case of the composite rGO/nC that can be attributed to the presence of the rGO component with 2D layered structure. The initial GtO material appeared non-porous with very low specific surface area (Table 1).

Table 1: *The BET specific surface area (SSA_{BET}), total pore volume (TPV) and main pores' diameter (MPD) of the prepared materials*

	Initial GtO	Pure nanocarbons	Composite rGO/nC
SSA_{BET} [m^2/g]	12	417	486
TPV [cm^3/g]	0.016	1.132	1.562
MPD. [nm]	3.2	3.8	4

The SSA of the composite rGO/nC increased significantly in comparison to the initial GtO reaching the value 486 m^2/g that is also higher than the SSA of the pure nC, with the TPT to follow the same trend. From the pore size distribution plots it is evident that the majority of the pores for all the samples have diameter between 3.2 and 4 nm. Also, a second population of pores with broad size distribution between 8 and 12 nm can be observed, which is less distinctive for the rGO/nC composite. This outcome may be related to the influence of the rGO component which hinders the aggregation of the nanocarbons and facilitates their homogeneous distribution. The high porosity of the rGO/nC composites makes them promising candidates for gas and/or energy storage applications.

4. Conclusions

Composite rGO/nanocarbons were successfully synthesized through a simultaneous reduction of solid graphite oxide and CO_2 gas at magnesiothermic conditions.

The XRD analysis evidenced the formation of nanocarbons for the pure nC and the composite rGO/nC. The initial GtO was not detected in the composite that was connected to its low content or to possible delamination/reduction during the treatment.

The SEM images demonstrated the delamination of the GtO and the presence of two types of morphologies for the composite, i.e. thin packs of layers and particles' aggregates attributed to the rGO and the nanocarbons, respectively.

The composite rGO/nC exhibited higher specific surface area (486 m^2/g) than the pure nC (417 m^2/g) that was related to influence of the rGO component hindering the aggregation of the formed nanocarbons.

5. Acknowledgments

The National Scientific Program "Petar Beron i NIE" contract number КП-06-ДБ/3 and "T1EDK-01729 CARBONGREEN" (MIS 5048538) co-financed by the European Union and Greek National Funds through the Operational Program Competitiveness, Entrepreneurship and Innovation, under the call RESEARCH-CREATE-INNOVATE are highly acknowledged.

6. References

1. A. Mondal, N.R. Jana, Rev. Nanoscience Nanotech. **3**, 177-193 (2014) https://doi.org/10.1166/rnn.2014.1051
2. N. Devi, R. Kumar, S. Singh, R.K. Singh, Crit. Rev. Solid State Mater. Sci. (2022) https://doi.org/10.1080/10408436.2022.2132910
3. V. Agarwal, P. Zetterlund, Chem. Eng. J. **405**, 127018 (2021) https://doi.org/10.1016/j.cej.2020.127018
4. A. Ahmed, A. Singh, S.-J. Young, V. Gupta, M. Singh, S. Arya, Compos. Part A **165**, 107373 (2023) https://doi.org/10.1016/j.compositesa.2022.107373
5. H. Zhang, X. Zhang, X. Sun, Y. Ma, Sci. Rep. **3**, article 3534 (2013) https://doi.org/10.1038/srep03534
6. C. Luchetta, E.C.O. Munsignatti, H.O. Pastore, Front. Chem. Eng. **3**, 707855 https://doi: 10.3389/fceng.2021.707855
7. T. Giannakopoulou, N. Todorova, N. Plakantonaki, M. Vagenas, I. Papailias, E. Sakellis, C. Trapalis, J. CO_2 Util. **65,** 102200 (2022) https://doi.org/10.1016/j.jcou.2022.102200
8. J. Entwistle, A. Rennie, S. Patwardhan, J. Mat. Chem. A **6**, 18344-18356 (2018) https://doi: 10.1039/c8ta06370b
9. N. Todorova, T. Giannakopoulou, N. Boukos, E. Vermisoglou, C. Lekakou, C. Trapalis, Appl. Surf. Sci. **391**, 601-608 (2016) https://dx.doi.org/10.1016/j.apsusc.2016.04.088
10. T. Giannakopoulou, N. Plakantonaki, M. Vagenas, I. Papailias, N. Boukos, N. Todorova, C. Trapalis, **17th**CEST, 00765 (2021) https://cms.gnest.org/sites/default/files/Proceedings/cest2021_00765/cest2021_00765.pdf
11. E.C. Vermisoglou, T. Giannakopoulou, G.E. Romanos, N. Boukos, M. Giannouri, C. Lei, C. Lekakou, C. Trapalis, Appl. Surf. Sci. **358**, 110-121 (2015) https://doi.org/10.1016/j.apsusc.2015.08.123
12. G. Leofanti, M. Padovan, G. Tozzola, B. Venturelli, Catal. Today **41**, 207-219 (1998) https://doi.org/10.1016/S0920-5861(98)00050-9

Synthesis and characterization of 2D $NbSe_2$

Dimitre Dimitrov[1,2*], Vera Marinova[2], Irnik Dionisiev[2]
Institute of Solid State Physics, Bulgarian Academy of Sciences, 72 “Tzarigradsko Chaussee” Blvd, 1784 Sofia, Bulgaria[1]
Institute of Optical Materials and Technologies, Bulgarian Academy of Sciences, Bl.109 “Acad. G. Bonchev Str., 1113 Sofia, Bulgaria[2]
dzdimitrov@issp.bas.bg

Abstract: *Two-dimensional van der Waals (vdW) materials possess novel physical properties and promising applications. A wide range of 2D vdW materials having been obtained via the chemical vapor transport (CVT) method. In this work, we develop the controllable growth meyhod of 2H-$NbSe_2$ single crystals via the CVT method. The quality of fabricated crystals was characterized by X-ray diffraction, and electron dispersive spectrometry (EDS) measurements. Crystals of the best quality were successfully grown under selected temperature/time schedule.*

Keywords: *TDMC, CVT (CHEMICAL VAPOR TRANSPORT), NBSE2, SINGLE CRYSTAL, STRUCTURE*

1. Introduction

In recent years, interest in the synthesis and applications of transition metal dichalcogenides MX_2 (M: Mo, W, X = S, Se, Te) nanomaterials has steadily grown because of their unique structure and superior properties [1]. Transition metal dichalcogenides have a sandwich interlayer structure formed by the stacking of the X–M–X layers, which are loosely bound to each other only by van der Waals forces and are easily cleaved. Moreover, MX_2 exhibits unique physical, optical and electrical properties correlated with their layered structure. In addition, their electronic structure is such that band-edge excitation corresponds largely to a metal centered d-d transition. Owing to these features, TMDCs materials have numerous applications such as sensors, detectors, solid lubricants, catalysis, electrocatalysis, high-density batteries and optoelectronic devices [2].

Niobium diselenide ($NbSe_2$) is transition metal dichalcogenide layered compound, and it is exceptionally attractive because of its super conductivity and the formation of a charge-density-wave (CDW) state [3]. 2H-phase niobium diselenide (2H-$NbSe_2$) is a superconducting vdW (Van der Waals) crystal with charge density wave (CDW) and Weyl semimetal properties. It has a superconducting critical temperature of ~7.8K and charge density wave behavior at ~34K. It has layered structure (lamellar) with weak interlayer coupling. $NbSe_2$ displays metallic and superconducting behavior.

2. Experimental details

Chemical vapour transport (CVT), a technique / process where a condensed phase, typically a solid is volatilized in the presence of a gaseous reactant (transport agent) and deposited elsewhere in the form of crystals. Typical transport agents include halogens and halogen compounds. The setup consists of a 2-zone furnace, the reactant and transport agent sealed in an ampoule. The various parameters that must be optimized for a successful CVT are growth temperature, transport direction, rate of the mass transport, choice of the transport agent and the free energy of the reaction.

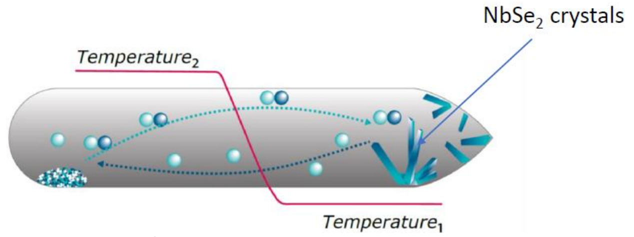

Fig. 1 *Schematic of the experimental setup.*

Single crystals of $NbSe_2$ were grown by a chemical vapour transport technique using iodine as transporting agent. A 5 gm mixture of Nb (purity: 99.95 %, Alfa Aeser, Germany) and Se (purity: 99.99 %, Alfa Aeser, Germany) was filled in a dried ampoule. Iodine of the quantity 5-6 mg/cc of the ampoule volume was sealed in the thin capillary and placed in the ampoule as transporting agent. Then the ampoule was sealed at the pressure of 10^{-5} torr. The sealed ampoule was introduced into a two-zone furnace at constant reaction temperatures to obtain the charge of $NbSe_2$. The charge so prepared was rigorously shaken to ensure proper mixing of the constituents and kept in the furnace again, under appropriate condition to obtain single crystals of $NbSe_2$. The experimental conditions for crystals growth are shown in Table 1.

Table 1: *Growth parameters for $NbSe_2$ single crystals using chemical vapor transport technique.*

	Length (mm)	ID (mm)
Ampoule dimensions	300	25
	Hot zone (K)	Cold zone (K)
Temperatures	1123	1053
	Time (hours)	
Growth time	240	

Powder X-ray diffraction (XRD) patterns were gathered within the 2Θ range from 20 to 80° with a constant step 0.02° on a Bruker D8 Advance diffractometer with a Cu Kα radiation and LynxEye detector. Phase identification was performed with the Diffracplus EVA using the ICDD-PDF2 Database.

3. Results and discussions

$NbSe_2$ is Molybdenite-like structured and crystallizes in the hexagonal $P6_3$ /mmc space group. The structure is two-dimensional and consists of two $NbSe_2$ sheets oriented in the (0, 0, 1) direction. Nb^{4+} is bonded to six equivalent Se^{2-} atoms to form distorted edge-sharing $NbSe_6$ pentagonal pyramids. All Nb–Se bond lengths are 2.62 Å. Se^{2-} is bonded in a 3-coordinate geometry to three equivalent Nb^{4+} atoms.

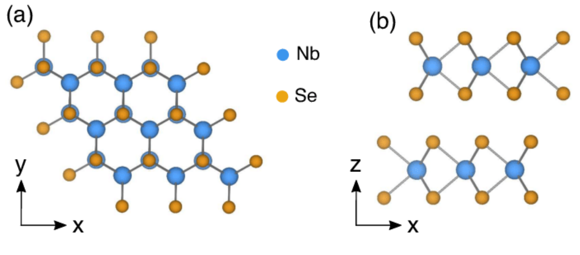

Fig.2 *(a) Crystal structure of bulk $NbSe_2$ illustrating the (a) top view and (b) side view of the structure. The x, y and z axes denote the cartesian axes*

Many methods have been developed to improve the crystalline quality of superconducting $NbSe_2$, for example: (a) exfoliation from bulk single-crystal $NbSe_2$ by the electrochemical exfoliation method [4]; (b) growth by salt-assisted CVD [5]; (c) growth by molecular beam epitaxy (MBE) under ultra-high vacuum [6]; and (d) growth of a wafer-scale $NbSe_2$ film in oxygen-free conditions by a two-step vapor deposition method [7]. However, most of the above preparations of $NbSe_2$ have either a lot of point defects or a small grain size, which reduces its environmental stability or Tc. Therefore, it is still challenging to develop a reliable strategy to grow 2D $NbSe_2$ with a large area, high crystalline quality, and high repeatability.

The CVT single crystals growth was chosen due to the advantages of bulk single crystals as large crystals to measure basic properties: structural, optical, electrical; nearly-perfect state of material: purity, no grain boundaries, less structural defects, stress, etc. The tunability of bulk properties: control of phase stoichiometry, doping level, alloy composition is readily obtained. The layered crystals as $NbSe_2$ are easily of exfoliation and stacking of heterostructures.

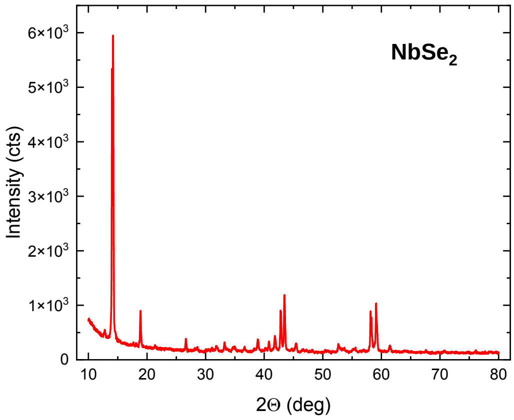

Fig.3 *XRD patterns of $NbSe_2$ single crystal*

The crystallinity, structure, and phase purity of the prepared samples were confirmed by XRD and EDS. As shown in Fig. 1a, all observed diffraction peaks can be exactly indexed to the hexagonal phase of $NbSe_2$ with lattice constants a = 3.445 Å and c = 12.55 Å (PDF No. 65-7464). No characteristic peaks were observed, and the sharp diffraction peaks imply a good crystallinity of the obtained $NbSe_2$ products under current synthesis conditions. The Energy-dispersive X-ray Spectrometry (EDS) result demonstrates that the samples are consisted of elements Nb and Se, while no other elements were observed.

4. Acknowledgements

We are grateful for the financial support from Bulgarian Science Fund project number КП-06-КОСТ/13 and COST Action CA17123 - Ultrafast opto-magneto-electronics for non-dissipative information technology (MAGNETOFON)

5. References

1. S. Manzeli, D. Ovchinnikov, D. Pasquier, O. V. Yazyev & A. Kis, Nature Reviews Materials, volume 2, article number: 17033 (2017)
2. A. A. Tedstone, D. J. Lewis, and P. O'Brien, Chem. Mater., 28, 7, 1965–1974 (2016)
3. Z. Li, X. Xi, B. Ding, H. Li, E. Liu, Yuan Yao, and W. Wang, Cryst. Growth Des., 20, 2, 706–712 (2020)
4. Z. Zeng, T. Sun, J. Zhu, X. Huang, Z. Yin, G. Lu, Z. Fan, Q. Yan, H.H. Hung, H. Zhang, Angew. Chem. Int. Ed., 51, 9052–9056 (2012)
5. H. Wang, X. Huang, Lin, J.; Cui, J.; Chen, Y.; Zhu, C.; Liu, F.; Zeng, Q.; Zhou, J.; Yu, P., Nat. Commun., 8, 394 (2017)
6. T. Hotta, T. Tokuda, S. Zhao, K. Watanabe, T. Taniguchi, H. Shinohara, R. Kitaura, Appl. Phys. Lett., 109, 133101 (2016)
7. H. Lin, Q. Zhu, D. Shu, D. Lin, Xu, J.; Huang, X.; Shi, W.; Xi, X.; J. Wang, L. Gao, Nat. Mater., 18, 602–607 (2019)